Departamento de
Universidade de Aveiro Eletrónica, Telecomunicações e Informática

2014

Francisco Manuel Ruivo Rodrigues

Transreceptor Óptico Integrado para PONs Híbridas
Photonic Integrated Transceiver for Hybrid PONs

Universidade de Aveiro Departamento de
Eletrónica, Telecomunicações e Informática
2014

Francisco Manuel Ruivo Rodrigues

Transreceptor Óptico Integrado para PONs Híbridas
Photonic Integrated Transceiver for Hybrid PONs

Dissertação apresentada à Universidade de Aveiro para cumprimento dos requisitos necessários à obtenção do grau de Mestre em Engenharia Electrónica e Telecomunicações, realizada sob a orientação científica de Dr. António Teixeira e Dr. Mário Lima, Professores do Departamento de Electrónica Telecomunicações e Informática da Universidade de Aveiro.

Apoio financeiro da FCT (Fundação para a Ciência e Tecnologia), ao abrigo dos projectos NG-PON2 and NG-PIC, e do QREN (Quadro Referência de Estratégica Nacional)

Dedico este trabalho aos meus pais José e Maria, à minha irmã e cunhado Joana e Hugo e à minha fonte de tranquilidade Maria Eduarda.

o júri

presidente

Professor Doutor José Carlos da Silva Neves
Professor Catedrático da Universidade de Aveiro

Professor Doutor António Luís Jesus Teixeira
Professor associado com agregação da Universidade de Aveiro

Professor Doutor Paulo Sérgio de Brito André
Professor associado com agregação da Universidade de Lisboa

agradecimentos

Os meus agradecimentos começam por se dirigir ao Instituto de Telecomunicações pelos recursos disponibilizados para a realização dessa tese.

Aos Professores António Teixeira e Mário Lima, que me orientaram ao longo deste último ano, um especial obrigado em primeiro lugar por todos os conhecimentos científicos transmitidos e em segundo pelo verdadeiro espírito de autonomia e confiança em mim que me ensinaram.

Aos meus colegas ao longo deste trabalho: Ana Lopes, Ana Tavares, Ricardo Ferreira e Simão Brandão as minha desculpas por todas as vezes que vos interrompi o raciocínio para vos por as minhas dúvidas, sem o vosso *know-how* isto não tinha a mesma piada.

À Associação Juvenil de Ciência o espaço a que dediquei mais tempo da minha juventude, tempo esse muito bem empregue. A todas as pessoas que lá conheci, que me orientaram e que eu orientei. Em especial ao Gonçalo Pimentel, o meu melhor amigo que eu ainda hoje não consegui perceber completamente e que por isso mantém a mesma piada desde o momento que o conheci. Podia-te agradecer por muita coisa, mas principalmente pelas decisões que tomaste para me proteger e eu não percebi.

Para chegar a esta tese, cinco anos de curso ficaram para trás e é sem dúvida que de pessoas se fazem as recordações. Começo por agradecer primeiro a quem me deixou no final da licenciatura Maria Beatriz Ferreira. Escusado será dizer que te agradeço pela ajuda ao longo deste percurso. Quero sim deixar público aqui que muito do que sou hoje academica, pessoal e profissionalmente o devo a ti. Foi um orgulho poder partilhar três anos de estudo e diversão contigo, muitas estórias e muitos sorriso ainda estarão para se desenlaçar. António Carvalho, Filipe Serra, Hélder Machado, Joana Garrido, João Azevedo, João Mendes,Luís Guedes, Maria da Graça e Rui Miguel Fernandes amigos para a Praça, para a bilbioteca e para todas as horas a vocês todos obrigado por terem partilhado estes cinco anos comigo.

Aos meus avós, pelo amor, ternura e ensinamentos que me transmitiram Aos meus pais a quem não posso estar mais grato pelo amor e educação que me deram, pelas portas que me abriram e por todas as oportunidades que me proporcionaram. Joana,minha irmã, obrigado por todas as brincadeiras que tivemos e por todas as vezes que me ajudaste a abrir os olhos.

Maria Eduarda, a nossa viagem mal começou. Até agora só tens feito uma coisa: ajudar ajudar ajudar. Obrigado.

palavras-chave Chip, Comunicações ópticas, Fotónica, QPSK , transreceptor, WDM,

resumo

Na era da tecnologia que estamos a viver, todos os cidadãos do mundo estão ligados em rede. Hoje em dia, ir às compras ou conhecer os lugares mais remotos do mundo sem sair de casa é possível graças à Internet. Dada a proliferação dos serviços que esta oferece, a largura de banda e a capacidade das redes tal como são hoje conhecidas estão a atingir o limite. Para fazer face a esse problema, a única solução que permite aos operadores fornecer o serviço desejado ao seus clientes são as comunicações ópticas. Estas conseguem proporcionar ritmos de transmissão na ordem dos Terabits/s e alcance na ordem dos milhares de kilometros . Redes ópticas passivas (PON) já estão standardizadas e implementadas por alguns operadores, contudo elas não tiram total partido das capacidades da fibra. Para que isso aconteça, redes que usem multiplexagem do comprimento de onda (WDM) e formatos de modulação avançados como Quadrature Phase Shift Keying (QPSK) têm que ser usadas.

O crescimento e evolução na implementação das redes ópticas irá torná-las mais complexas. Essa complexidade irá ser traduzida no hardware que, hoje em dia, ainda é feito maioritariamente com componentes discretos. Se o seu uso se continuar a verificar, o espaço necessário para as unidades como terminação de rede de transporte óptica (OLT) irá ser elevado. Então, o desenvolvimento das redes ópticas terá que ser feito usando dispositivos ópticos integrados.

Como contribuição para o desenvolvimento das redes ópticas passivas de futuras gerações, este trabalho apresenta o desenho e a implementação de um transreceptor óptico integrado para uso em redes PON com topologia WDM que suportem formatos de modulação avançados. Este tipo de redes são denominadas neste trabalho PONs híbridas. No início, um estudo dos transreceptores disponíveis no mercado é feito para posterior comparação e posicionamento do produto desenvolvido. De seguida, diferentes componentes ópticos são apresentados de um ponto de vista teórico e para os necessários para o chip, modelos são criados. A arquitectura do circuito é depois apresentada e dividida em três blocos. Para cada um, o seu princípio de funcionamento e implementação no chip são demonstrados. No fim, testes laboratoriais são feitos. Estes testes, visam a validação da arquitectura e funcionalidade do chip.

keywords Chip, Optical communications, photonics , QPSK, transreceptor , WDM

abstract

On the technology era that we are living, all the citizens of the world are connected in a network. Nowadays, either shopping or meet the most remote place on Earth without leaving home is possible due to the Internet. Because of the proliferation of the services that the Internet provides, the bandwidth and capacity of the networks as they are known are facing their limit. In order to solve this problem, the only solution that the service providers have to properly supply their clients are the optical communications. They allow bitrates in the order of Terabits/s and a reach that can go up to thousands of kilometers. Passive Optical Networks (PONs) are already standardized and deployed by some of service providers. However, they do not use all the fibre capabilities. In order to take full advantage of the fibre capacities, networks that use Wavelength Division Multiplexing (WDM) and advanced modulation formats such as Quadrature Phase Shift Keying (QPSK) must be used.

Owing to the growth and evolution of the optical networks, they will become more complex. This complexity will also be at a hardware level that nowadays is still composed by discrete components. The room needed for units such as Optical Line Terminals (OLTs) will be high if integrated optical circuits are not used. Thus, the development of optical networks must be done using Photonic Integrated Circuits (PICs).

As a contribution for the development of optical networks of future generations, this work presents the design and implementation of an integrated optical transceiver for PONs with WDM topology that supports advanced modulation formats. These type of networks are called, in the scope of this work, hybrid PONs. At the beginning, a market analysis of the transceivers available is done so that it can be used for comparison and positioning of the developed product. Afterwards, one can read about the theory background of different optical components. For the ones needed on the chip, models are created. The architecture of the transceiver is then presented and divided in three blocks. For each one, its working principle and on chip implementation are presented. At the end, laboratory tests are performed. Their goal is to validate the chip functionalities and architecture.

CONTENTS

LIST OF FIGURES

LIST OF TABLES

LIST OF ACRONYMS

Advanced Simulator for Photonic Integrated Circuits	ASPIC
Allowable Path Loss	APL
Arrayed Waveguide Grating	AWG
Avalanche Photodiode	APD
Beam Propagation Method	BPM
Bit Error Rate	BER
C Form Factor Pluggable	CFP
Conduction Band	CB
Cosimulation	cosim
Digital Signal Processing	DSP
Erbium Doped Fiber Amplifiers	EDFA
Error Vector Magnitude	EVM
Ethernet Passive Optical Network	EPON
External Cavity Laser	ECL
Fiber to the Home	FTTH
Free Propagation Region	FPR
Free Spectral Range	FSR
Full Service Access Network	FSAN
Full Width at Half Maximum	FWHM
Germanium	Ge
Gigabit Interface Converter	GBIC
Guided Mode Propagation Analysis	MPA
Indium Phosphide	InP
Inidium Gallium Arsenide	InGaAs
In-Phase	I
Input and Output	I/O
Integrated Circuit	IC
Intermediate Frequency	IF
International Telecommunications Union - Telecommunication	ITU-T
LiNbO3	Lithium Niobate
Local Oscillator	LO
Mach-Zehnder Modulator	MZM
Multimode Interference device	MMI
Multiquantum Well	MQW
Multi-Sourge-Agreement	MSA
New Generation - Passive Optical Network	NG-PON
Non Return to Zero	NRZ
On-Off Keying	OOK
Optical Coherent Receiver	OCR
Optical Line Terminal	OLT
Optical Network Unit	ONU

Optical Spectrum Analyzer	OSA
Optical-to-Electrical-to-Optical	OEO
Passive Optical Network	PON
Phased Array	PHASAR
Photonic Integrated Circuit	PIC
p-i-n Photodiode	PIN
Point-to-Multipoint	P2MP
Polarization Beam Splitter	PBS
Polarization Controller	PC
Quad Samall Form Factor Pluggable	QSFP
Quadrature	Q
Quadrature Amplitude Modulation	QAM
Quadrature Phase Shift Keying	QPSK
Quantum Well	QW
Receptor	Rx
Rejection AWG	R-AWG
Semiconductor Optical Amplifier	SOA
Silicon	Si
Smal Form Factor pluggable	SFP
Small Form Factor	SFF
Standard Single Mode Fiber	SSMF
Time and Wavelength Division Multiplexing	TWDM
Transmitter	Tx
Transverse Electric	TE
Tunning AWG	T-AWG
Valence Band	VB
Variable Optical Attenuator	VOA
Wavelength Division Multiplexing	WDM

1 INTRODUCTION

1.1 Context and Motivation

Technology growth brought human kind to a new stage of development where simple things like shopping or complex situations in human relations are at the distance of one click, because we are now all connected. Our connection is the Internet. If one sees the Internet as a resource it is easy to understand that the mankind demanded more and more information and thus bandwidth and speed bringing the network capacity to its limits like we did with our other resources.

In concrete numbers, the growth of the Internet between 2000 and 2012 was 566% which corresponds to a 34.3% of internet penetration. The region with the biggest increase in that period of time was Africa with a growth of 3607%, followed by the Middle East that had a growth of 2640%. However, the distribution of the service around the world is unequal. While in North America the internet penetration is 78.6%, in Africa is only 15.6%. [1]

The only communication technology able to go along with the demands of bandwidth imposed by the growth of the internet is the optical communications technology. As one can conclude from Figure 1 it is the only technology that allows bitrates in the order of Terabits and long distances. Apart from satellites communications optical communications are the only that allow links with thousands of kilometers without the need of regeneration of data.

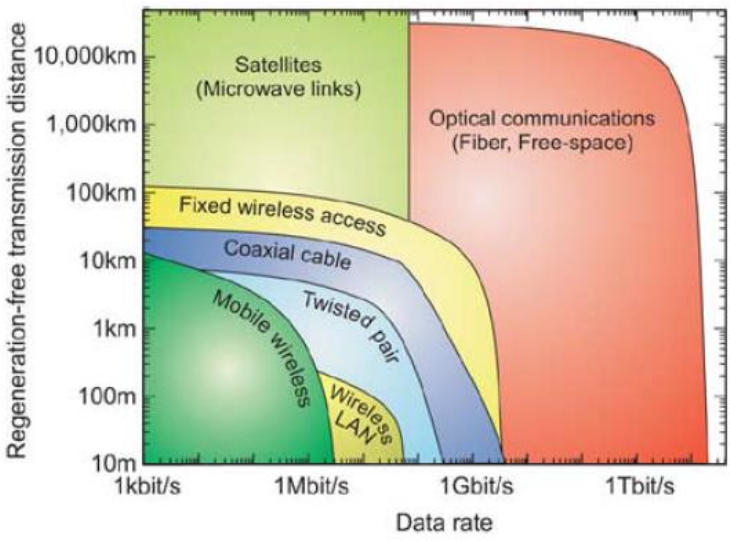

Figure 1 Renegeration-free transmission distance versus data rate for various wireless and wireline communication technologies [2]

Passive optical networks (PONs) have a topology of point-to-multipoint (P2MP) where all the elements should be passive (no power supplies to operate). This topology was the one chosen to provide the service of Fibre to The Home (FTTH) as it offers higher bitrates, reduces power consumption and requires less space in centrals. To properly implement this type of networks in mass, standardization needed to be done. Full Service Access Network (FSAN) and International Telecommunications Union-Telecommunication (ITU-T) are the entities that were more involved in the standardization of PONs. In the standardization, details like the spectrum management, up and downstream bitrates are defined. Since 2010 the New Generation-PON 1 (NG-PON1) is standardized. Its long term evolution is the NG-PON2 that is predicted to be fully standardized in 2015. It defines 40Gb/s of downstream and 10Gb/s for upstream divided over 4 channels using Time and Wavelength Division Multiplexing (TWDM). [3] In a TWDM-PON, a unique channel (wavelength) for downstream and upstream is fully assigned to a user at a time.

The bitrates provided by PONs and NG-PON1 and 2 are high and can, for a short period of time, solve the problem of bandwidth demand. However, the capacity of optical fibre communications is greater than the one that is in use with these topologies. A solution to take advantage of all the properties of fibre optics communication is the combination of Wavelength Division Multiplexing (WDM) with higher order modulation formats such as Quadrature Phase Shift Keying (QPSK). This solution is onwards called hybrid PON and it has been defended by several authors, e.g. [4] [5].

With the growth of the deployment of optical networks, their complexity will also increase. The optical hardware used nowadays is based on discrete components. This should be revised because in less than a decade the room at the central offices and the power consumption are going to be a huge problem. Photonic integrated circuits (PICs) are the solution to this problem. PICs are the equivalent of electronic Integrated Circuits (ICs) in the optical domain. Instead of containing transistors or other electronic components, they contain optical elements such as optical amplifiers or optical multiplexers. PICs emerge at the end of the 60s although, it took four decades to the first one enter in the marketplace. This was due mainly for two reasons. In one hand in the 90s a shift on technology focus from 'technology push' to 'market pull' delayed the funding for photonic integration, on the other hand there was a fail on the coordination of technology development which led to high costs and several different technologies developed [6]. Nowadays one can find more benefits in PICs than negative points. Among other reasons, PICs reduce space and power consumption while improve reliability. Moreover they reduce the cost of optical-to-electrical-to-optical (OEO) conversions.

With this contextualization, the reader is able to conclude that PICs for PONs that take advantage of all the fibre capacities will be needed. In order to contribute to the development of this technologies, in this document it is presented a photonic integrated transceiver for hybrid PONs. Commercially available versions of transceivers are presented in the beginning. The transceiver's components and architecture are discussed along the third chapter of the thesis and at the end one can find laboratory results for a proof of concept of the transceiver architecture.

1.2 Objectives

The context and motivation of this work were already presented. To enable high capacity networks, WDM PONs with advanced modulation formats have to be used. Moreover, to make the referred networks as much efficient as possible PICs have to be used. Hence, the main scope of this thesis is to present a photonic integrated transceiver for hybrid PONs. To do so, the thesis has the following objectives:

- Present a market analysis of the transceivers available in order to place and differentiate the final designed transceiver.
- Study different PIC components.
- Model PIC components of a specific foundry to allow its future simulation.
- Design PIC components for a specific application and for a specific foundry.
- Study the architecture of a WDM coherent optical transceiver.
- Demonstrate the steps of the design implementation of a PIC for a specific foundry
- Present the on-chip design of an optical transceiver for hybrid PONs.
- Do a laboratory proof of concept of the designed architecture.

1.3 Structure

In order to provide the best readability to the reader the chapters were organized in flow and content as it is presented:

- **Chapter 2: Market Analysis** It starts to present an overview of the different standard optical transceiver packages by highlighting functionalities, applications and dimensions. The available transceivers on the market of two of the biggest vendors (Finisar and Fujitsu) are compared in their different parameters such as power dissipation, wavelength of operation and bitrate.
- **Chapter 3: Photonic Integrated Circuit Components** The following components are studied: Semiconductor Optical Amplifier (SOA), Mach-Zehnder Modulator (MZM), Arrayed Waveguide Grating (AWG), Multimode Interference devices (MMI), optical directional coupler and photodetectors. The modulation for the specific application and foundry is performed for the SOA, MZM and AWG. The design of photonic components to use in the transceiver is performed namely for SOA, AWG, MMI and coupler. Different applications of the components can also be found along the chapter.
- **Chapter 4: Photonic Integrated Transceiver Design** This section of the thesis is devoted to present the design steps of the optical transceiver. First are

presented the different design steps that an optical chip face during the process then the architecture of the transceiver is presented block by block: laser cavity, transmission block and reception block. For each part, the operating principle is discussed and the components are placed on the chip.

- **Chapter 5: Laboratory Experiments and Results** Presents the laboratory tests and results that were done to prove the concept of the presented architecture. Two setups, each one with two versions are presented, studied and compared.
- **Chapter 6: Conclusions and Future Work** The main conclusions and achievements of this work are presented in Chapter 6. At the end, future work is proposed.
- **Appendix**

1.4 Contributions

The main contributions of this work are:

- A market analysis of the transceivers available on the market.
- Explanation of several different PIC components.
- Discussion of optical transceiver architectures.
- Discussion of different architectures of the coherent receiver.
- Design of a photonic integrated transceiver for hybrid PONs
- Submission of the paper "Photonic Integrated Transceiver for Hybrid PON" in the *16th International Telecommunications Network Strategy and Planning Symposium*
- Ana Tavares, Ana Lopes et al, "Photonic integrated transmitter and receiver for NGPON2" in the *II International Conference on Application of Optics and Photonics.*

2 MARKET ANALYSIS

A transceiver is a unit that includes both a transmitter and a receiver, which are combined and share the same package and common circuitry. The definition was presented in the early 1920s, since then the concept has been adopted through different types of communications both wired and wireless.

In simple terms, an optical transceiver modulates light according to an electrical signal on the transmitter side and converts an optical signal into an electrical one on the receiver side.

Transceivers can be divided according to their package. In the context of this thesis the analyzed packages were: SFP,SFP+,SFF,QSFP,QSFP+,CXP,GBIC,XFP,X2,XENPAK and 300-PIN.

2.1 Optical Transceiver Packages

SFP and SFP+(Small form-factor pluggable): it was designed to be hot-swappable and to offer high- speed performance. SFP was the first standardized form factor and was used for data rates up to 4 Gb/s. Examples of applications are the networks that use Dense Wavelength Division Multiplexing (DWDM). The rising need for higher data rates resulted on the development of SFP+. It is an enhanced version of SFP settled for applications up to 10 Gb/s and beyond. Specially used in data and telecom optical links, its main applications are 8G fibre Channel, 10 Gb Ethernet and Optical Transport Network standard OTU2.

Both SFP and SFP+ can be used in the same cages, which are presented in Figure 2.

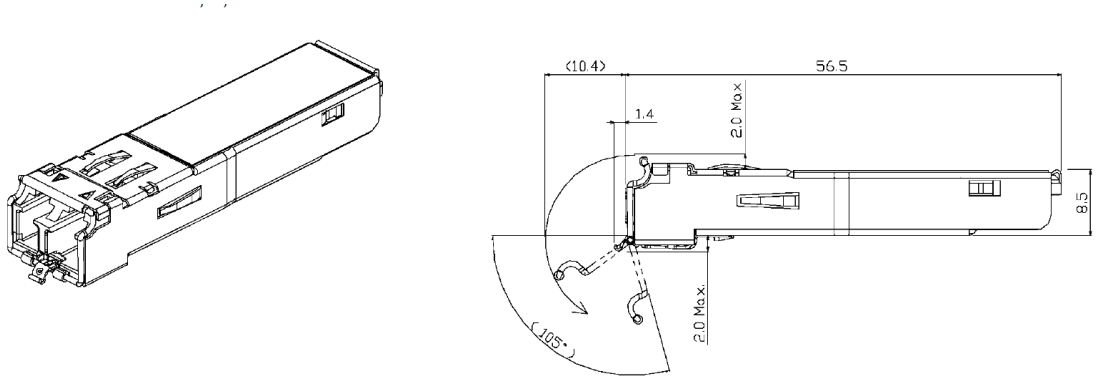

Figure 2 SFP cage and its mechanical dimensions mm] [7]

CFP(C Form-factor Pluggable): Hot-pluggable transceiver module form fact was developed for 100 Gigabit Ethernet Systems. With the use of different versions of CFP modules, one can realize applications for several link distances either multimode or single mode. CFP modules nowadays have innovative features such as thermal management or enhanced signal integrity systems. The electrical interface to the host board is based on a Nx10 Gb/s, with N depending on the application supported.

In Figure 3, mechanical dimensions of different CFP modules can be compared. Both CFP2 and CFP4 are the evolved form of CFP and each of them has its own Multi-Source-Agreement (MSA).

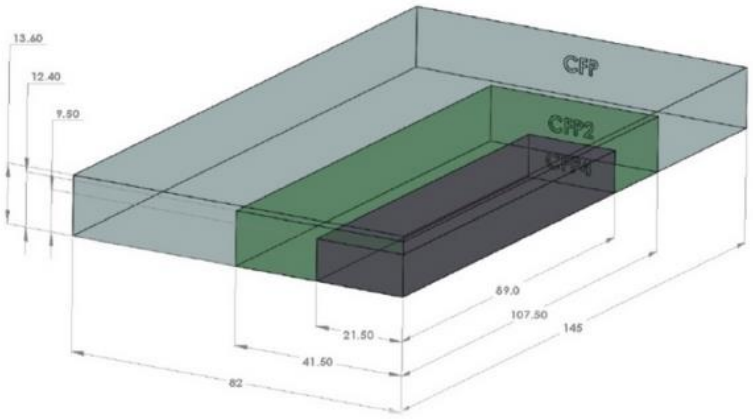

Figure 3 CFP, CFP2, CFP4 blocks and their mechanical dimensions [mm] [8]

SFF(Small Form Factor): similar to SFP it was designed for data ranges up to 4Gb/s . It offers pin-thru hole soldering onto a host board offering physical compactness.

Several configurations are available, an example is the 2x5 industry standard MSA compliant which is presented in Figure 4.

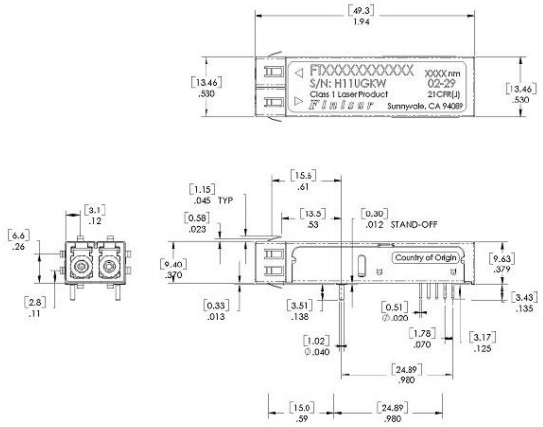

Figure 4 SFF Finisar FTLF1319F1xTL and its mechanical dimensions [mm] [9]

QSFP or QSFP+ (Quad Small Form-factor Pluggable): high-density, hot-pluggable form factor transceiver that provides 4 channels of traffic in each direction. QSFP was the initial version module and supported 2.5 Gb/s and 5 Gb/s per channel. The evolution of QSFP format is QSFP+ that supports up to 10.5 Gb/s per channel for applications such as 40G Ethernet. QSFP+ mechanical dimensions are presented in Figure 5.

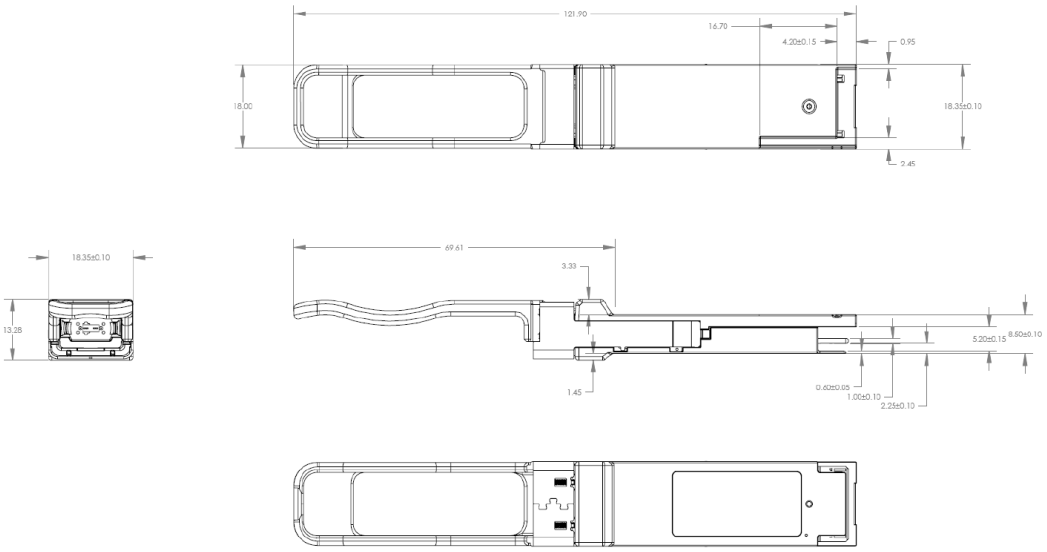

Figure 5 QSFP+ MSA package and its mechanical dimensions [mm] [10]

CXP: hot pluggable transceiver that provides 12 channels of traffic in each direction. With up to 12.5 Gb/s per channel, it can support applications such as 100G Ethernet. In comparison with the entire standardized pluggable form factor, it has the highest density and the lowest power dissipation. However, it is limited to short single mode links. According to the CXP specifications the physical dimensions are presented in Figure 6.

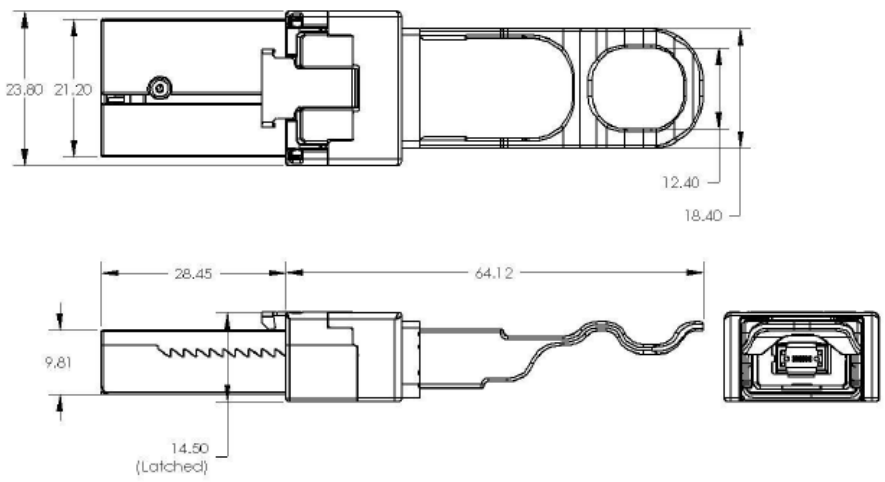

Figure 6 CXP Finisar FTLD10C and its mechanical dimensions [mm] [11]

GBIC(Gigabit Interface Converter): It offers a hot-swappable electrical interface, that allows one gigabit port to support a wide range of physical media. SFP is considered to be a variation of GBIC and is often known as mini-GBIC.

XFP(10 Gigabit Small Form Factor Pluggable): designed for serial 10Gb/s, it is used in data and telecom optical links. It is protocol independent and fully compliant with several standards such as 10G Ethernet. A major advantage is its smaller footprint when compared to other 10 Gb/s transceivers. XFP electrical interface to the host board is called XFI

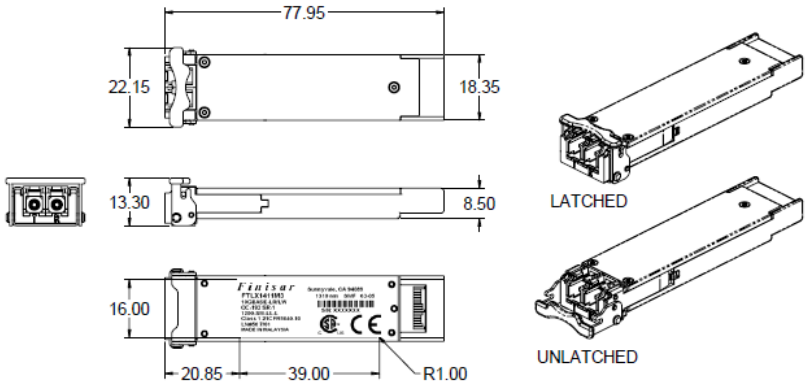

Figure 7 XFP transceiver and its mechanical dimensions [mm] [12]

X2/XENPAK: standardized form factors for 10Gb/s fibre optic transceivers which are used in data communication optical links. Their electrical interface to the host boards is called XAUI.

X2 and XENPAK mechanical dimensions are presented in Figure 8.

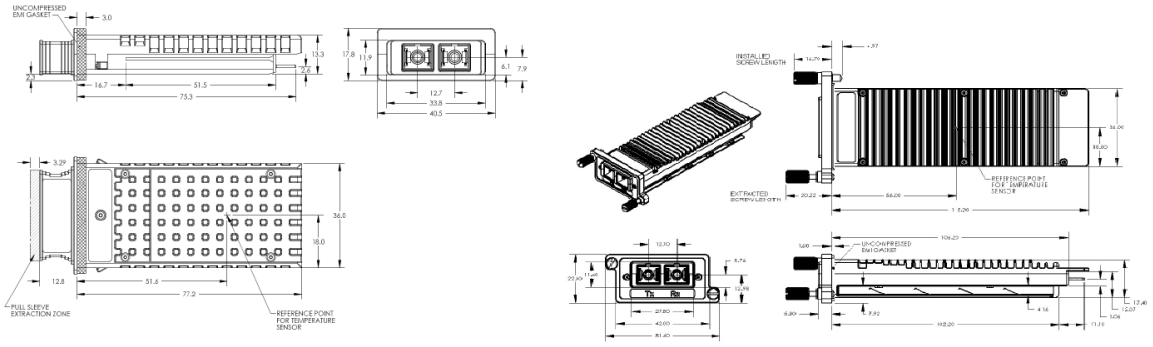

Figure 8 Left: X2 mechanical dimensions [mm] [13] **Right: XENPAK mechanical dimensions [mm] [14]**

300-PIN: standardized pigtailed form factor for 10 and 40Gb/s communications primarily used in telecom and DWDM applications. The electrical interface to the host board is a 16-lane bus. Standard dimensions are: L x W x H:127 x 102 x 17 [mm].

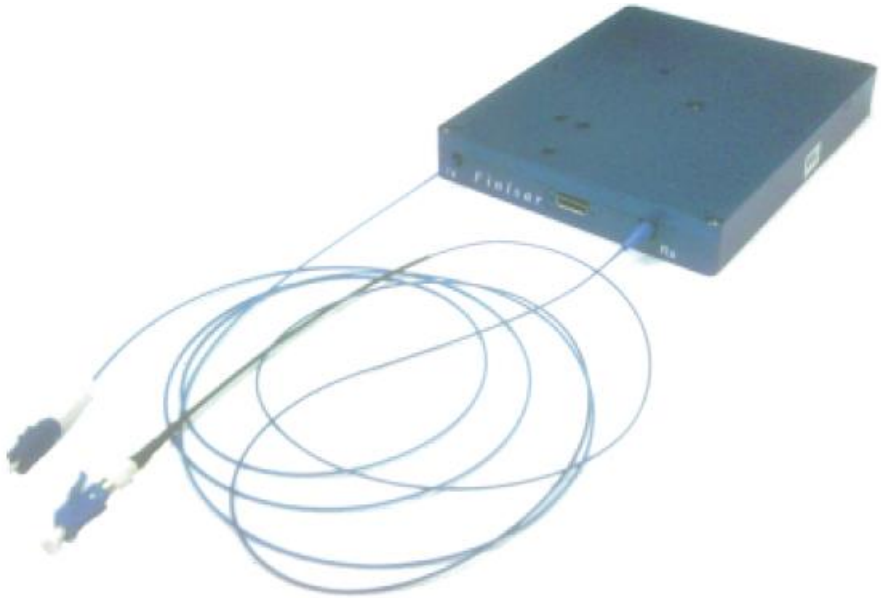

Figure 9 300 PIN Finisar cage [15]

2.2 Comparison Study and Data Analysis

The following section presents the market analysis that was done to systematize the different options of available transceivers according to their packages and characteristics (e.g. power dissipation). The study was carried out with the information present on the catalog of the vendors *Finisar* and *Fujistu* because they can be considered to be on the top of the leader vendors and they offer a large, diversified set of transceivers.

In order to have a fair comparison among the different transceivers they were divided according to the packages presented in the previous sub section. In the figures of the current subsection one can find a package called PON which was not presented previously. This is due to the fact that PON are transceivers sold by *Finisar* that are compliant with SFP characteristics but are designed for specific Ethernet PON (EPON) and PON applications. After the division, their most relevant characteristics were studied: bitrate and distance versus minimum/ maximum power of the transmitter, sensitivity of the receiver, allowable path loss (APL), power dissipation and minimum and maximum wavelength of both transmitter and receiver. In order to perform the data analysis, the collected information was processed on *Matlab*®.

2.2.1 Minimum Power of the Transmitter

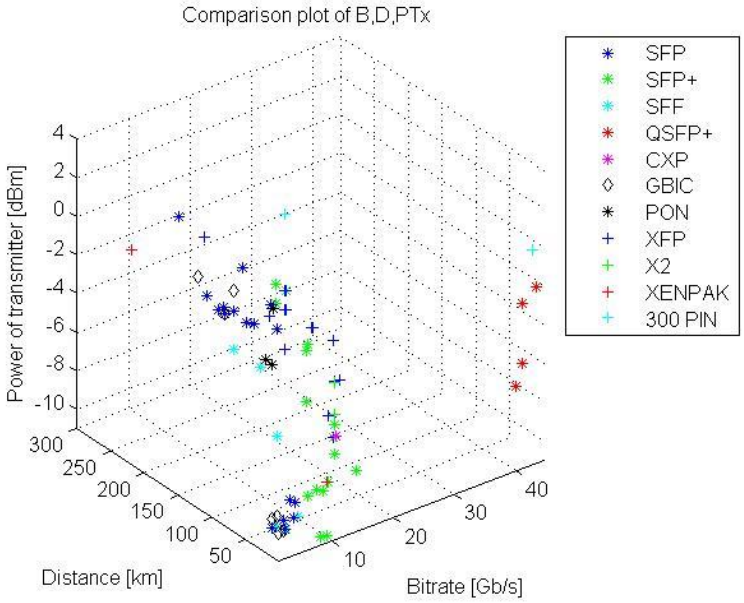

Figure 10 Comparison plot of bitrate, distance and minimum power of the transmitter

The tridimensional plot of Figure 10 allows the reader to verify the scattering of the points along the axes as well as the concentration of the different packages along the bitrate,

distance product. In order to have a better analysis of these features, one can analyze Figure 11. Along this subsection for all the studied parameters, first it is presented the tridimensional plot and then its decomposition in two dimensional.

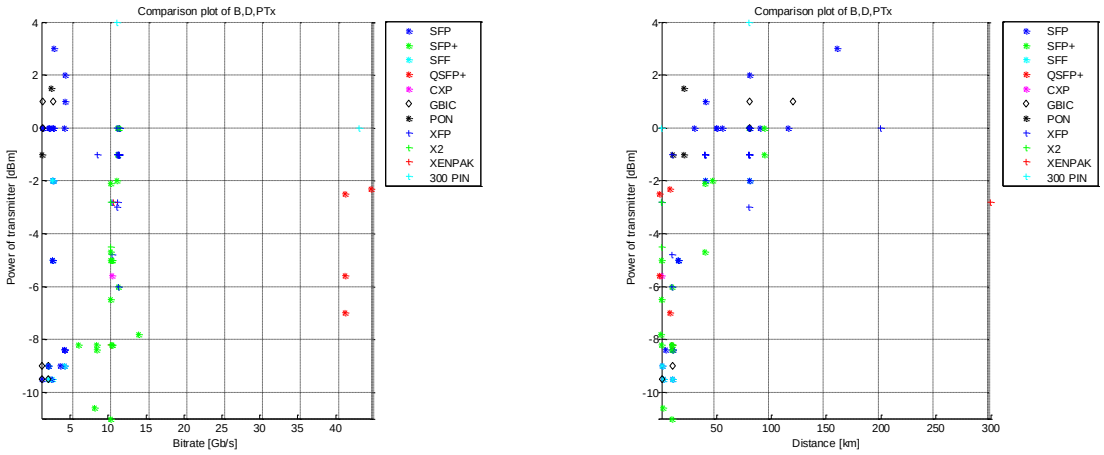

Figure 11 Minimum power of the transmitter versus bitrate (left) and transmission distance (right), for different packages

As Figure 11(right) shows, with the increasing of the distance, more power in the transmitter is needed in order to overcome the losses that are going to occur in the fibre. The package that, in average, needs more power is SFP. This can be explained with the fact that it is the oldest package, thus when it was developed the technology was not as evolved as today. On the other hand the package that, in average, needs less power is the SFP+. Regarding this package, the scattering of the points relative to this package grows from less than -10dBm to 0dBm. However, one should keep in mind the fact that the maximum distance for this package is around 100km.

From the observation of Figure 11 (left) one can conclude that as the demand for a higher bitrate increases, more power in the transmitter is needed. The highest bitrates are provided by QSFP+. In comparison with other packages, QSFP+ has a good performance in terms of bitrate versus power of transmitter. The cloud of points is mostly concentrated in the region of the 10Gb/s or less, since most of the packages and applications were designed for rates in the referred region.

2.2.2 Maximum Power of the Transmitter

With the observation of Figure 13 one can conclude that its plots are approximated shifted versions of the ones in Figure 11. This shift refers to the power axis which is the one that is under analysis. The maximum power of transmitter is around 7dBm, for an SFP transceiver and the minimum maximum power is for GBIC. Both of them for small bitrates. One can also notice that although the QSFP+ is the one with the highest bitrate it is not the one with the highest maximum power.

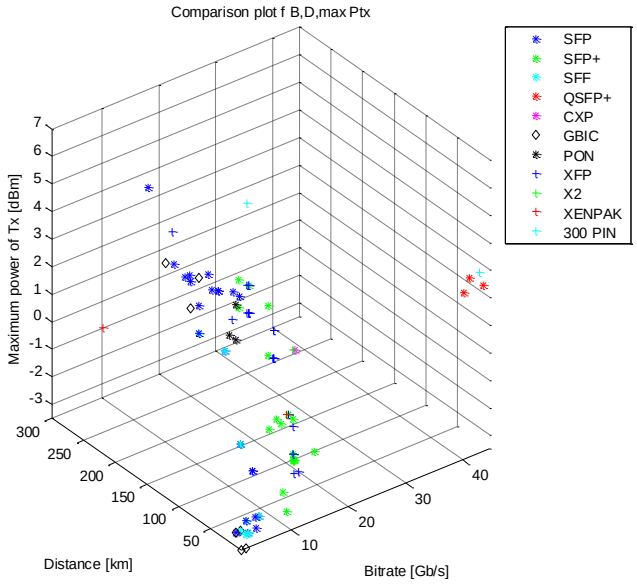

Figure 12 Comparison plot of bitrate, distance and maximum power of the transmitter

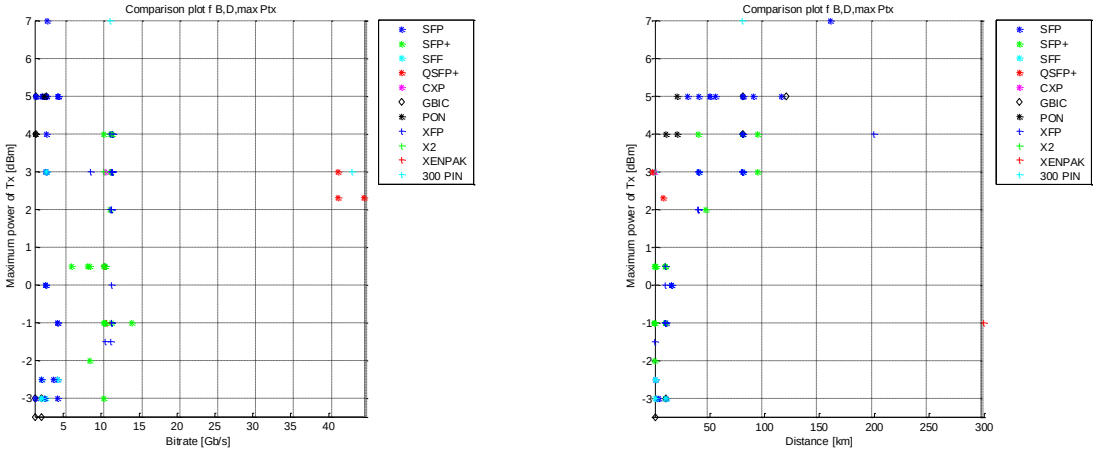

Figure 13 Maximum power of the transmitter versus bitrate (left) and transmission distance (right), for different packages

2.2.3 Sensitivity of the Transceiver

Sensitivity can be defined as the minimum acceptable received power to achieve a defined Bit Error Rate (BER) thus it represents an important criteria on the transceiver performance.

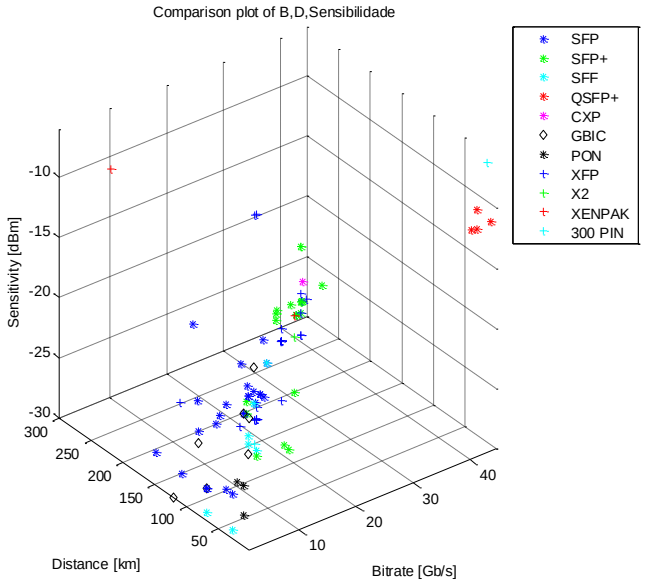

Figure 14 Comparison plot of bitrate, distance and sensitivity

From the data analysis presented in Figure 14 and Figure 15, the mean value of the sensitivity for these transceivers is around-19.5dBm. The lowest values of sensitivity are for GBIC and SFF, which represent a good performance. Instead, the package that presents the highest values of sensitivity is SFP+ even for small distances. Hence, if one only takes in consideration the trade-off between distance and sensitivity for choosing a transceiver, SFP+ would in general be in disadvantage against the other packages.

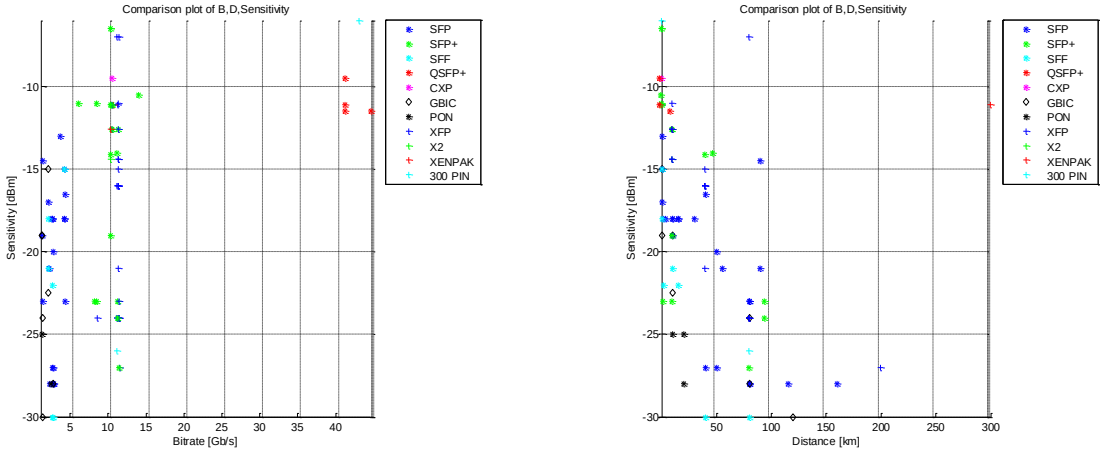

Figure 15 Sensitivity versus bitrate (left) and transmission distance (right), for different packages

In Figure 15 (left) the vertical lines represent constant values of bitrate, and in those lines even for the same packages, one can observe different values of sensitivity. This yields to the conclusion that these two criteria, bitrate and distance, all along are not enough to make the best choice for a transceiver.

2.2.4 Allowable Path Loss

APL is defined for point to point communications and represents the maximum loss that one can have on the fibre, in case of not having any amplifier on the path. These results represent the APL that is obtained when is used the same transceiver on the receiver and transmitter side. Although this is not a realistic implementation, it can give a good indicator of possible APLs.

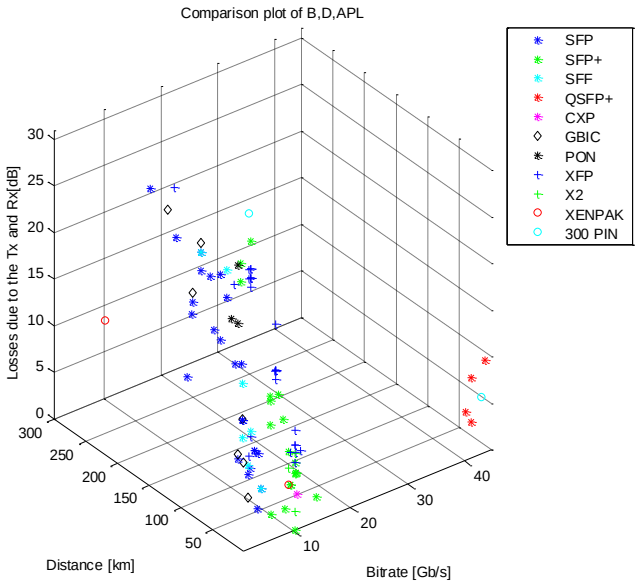

Figure 16 Comparison plot of bitrate, distance and APL

With the analysis of the Figure 17, one can conclude that APL is normally in the range of 0-30dB, which is an acceptable interval for regular applications. Taking in consideration that in a regular fibre transmission at 1550nm the attenuation is about 0.2dB/km, the values presented here are enough to overcome that loss. For example after 100km, the losses would be 20dB and in most of the presented transceivers around 100km the value is higher than 20dB thus using the same transceiver in both sides (Transmitter - Tx and Receptor-Rx) can suit most of the desired applications.

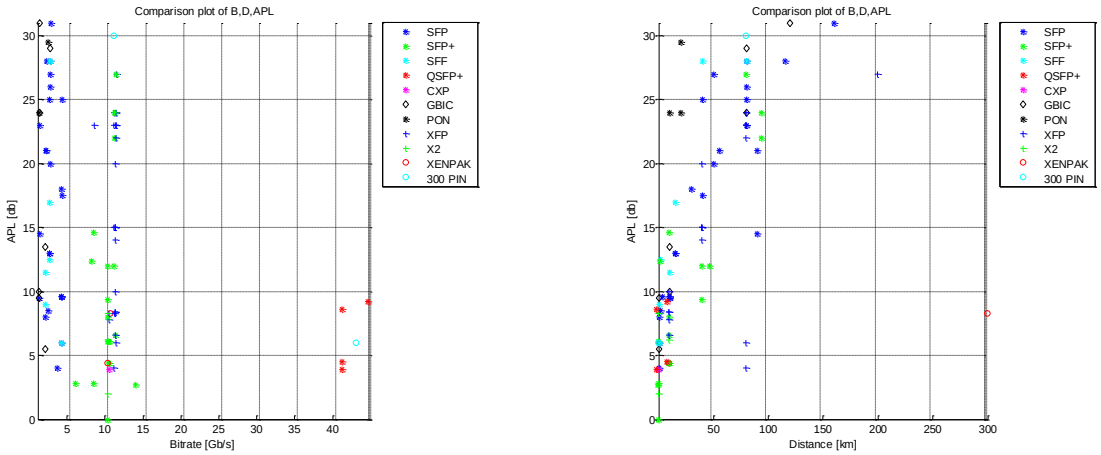

Figure 17 APL versus bitrate (left) and transmission distance (right), for different packages

2.2.5 Power Dissipation

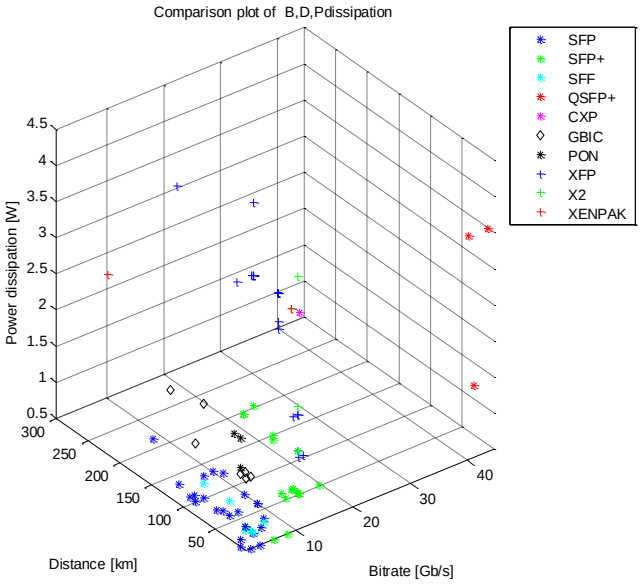

Figure 18 Comparison plot of bitrate, distance and power dissipation

The parameter power dissipation is important in the way that it sets the needs for power supply in the receiver and transmitter side as well as defines the costs of energy during the time that the transceiver is going to be used. In Figure 18 it is possible to confirm that for different transceivers of the same package the power dissipation does not show a large variation.

By inspection of Figure 19 (right), one can conclude that the package SFP is the one with less power dissipation: in average less than 1W. On the other hand, the package with more power dissipation is XFP. One can also observe that these two packages work almost in the same range of distances but the power dissipation is completely different, which can be due to the different applications of each one.

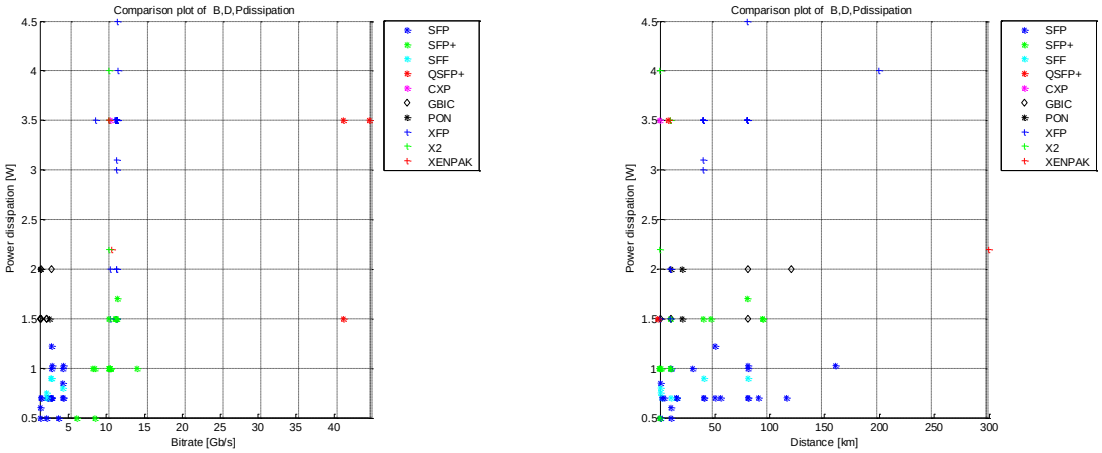

Figure 19 Power dissipation versus bitrate (left) and transmission distance (right), for different packages

In terms of bitrate the conclusions are similar with the respect to the distance, i.e. the scattering of the points on the vertical axis is done according to the different packages. Here, one can focus on the QSFP+ and notice that, although its transceivers are the ones with the highest bitrate, they are not the ones with more power dissipation which is a good feature.

2.2.6 Maximum and Minimum Wavelength of the Transmitter

The wavelength at which the information is sent is the parameter that defines for example which kind of fibre is going to be used or which kind of amplifiers should be chosen on the communication link.

On the figures related to these parameters, the reader can conclude that most part of the transceivers work around 1500-1600 nm which correspond to the region where the so called C and L band are defined. The C-band is defined from 1530-1560nm

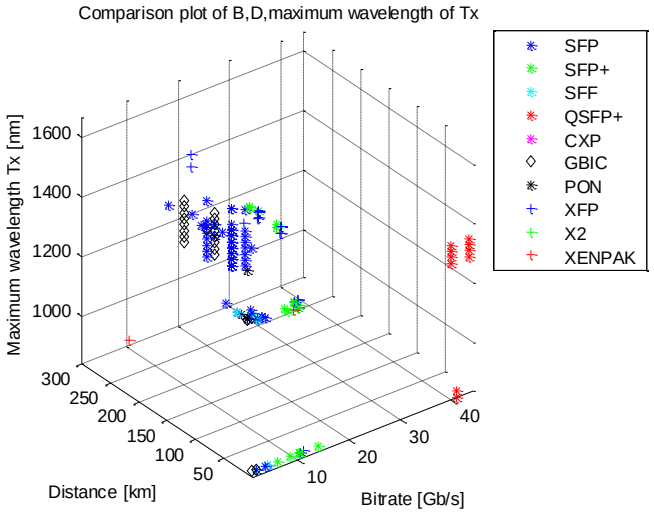

Figure 20 Comparison plot of bitrate, distance and maximum wavelength of transmitter

and Erbium Doped Fibre Amplifiers (EDFAs) are the amplifiers which are normally used. The L-band is defined from 1570-1610nm and normally the amplifiers used are the gain-shifted EDFAs and the Raman amplifiers. The two parameters (maximum and minimum wavelength) were studied for the different transceivers in order to understand its dynamic range.

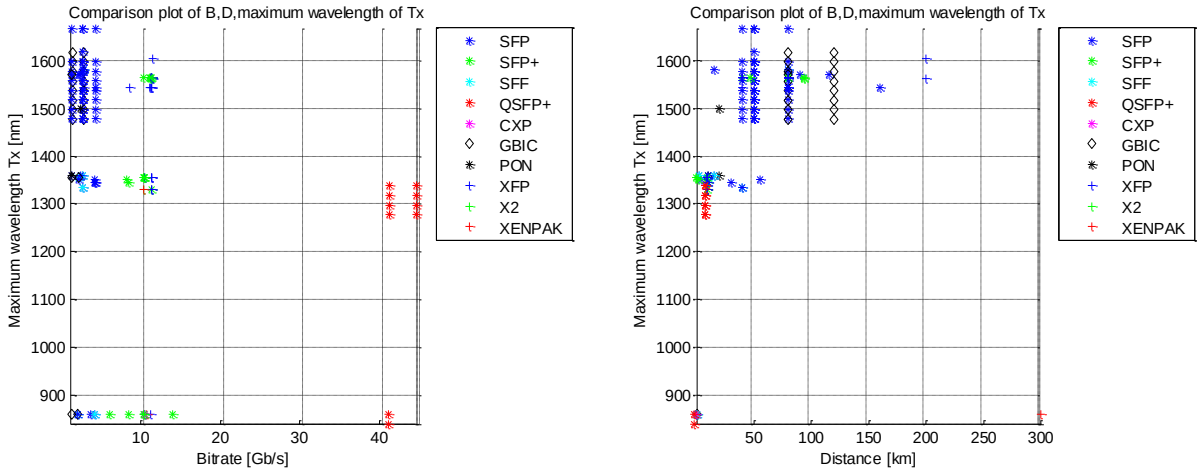

Figure 21 Maximum wavelength of transmitter versus bitrate (left) and transmission distance (right), for different packages

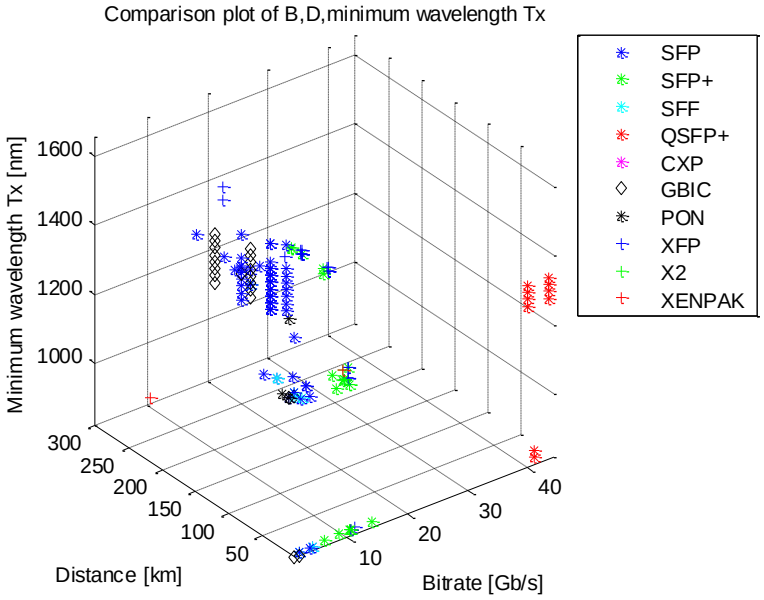

Figure 22 Comparison plot of bitrate, distance and minimum wavelength of the transmitter

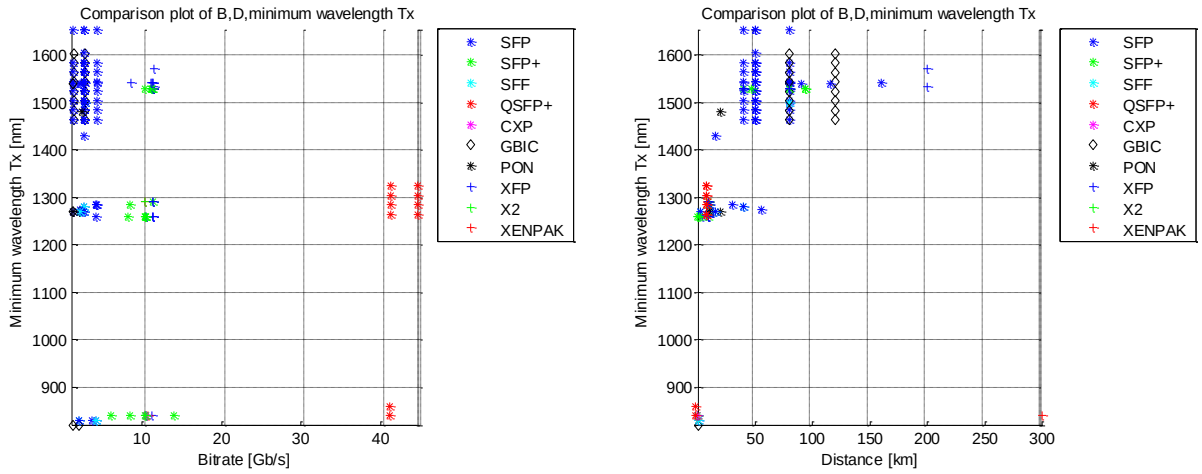

Figure 23 Minimum wavelength of transmitter versus bitrate (left) and transmission distance (right), for different packages

2.2.7 Maximum and Minimum Wavelength of the Receiver

Regarding the receiver, it is important that it is tunable over a wide range of wavelengths so that it can be used in different network scenarios. This feature combined with the sensitivity can be used to perform an evaluation of the quality of the receiver and thus the transceiver where it is embedded.

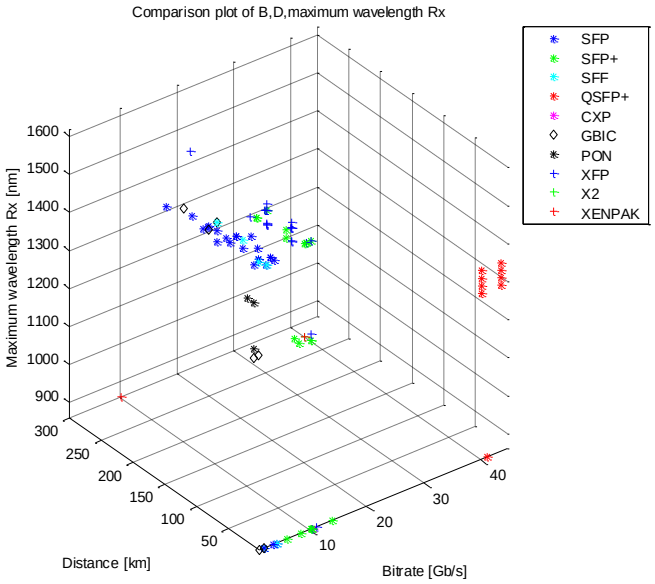

Figure 24 Comparison plot of bitrate, distance and maximum wavelength of the receiver

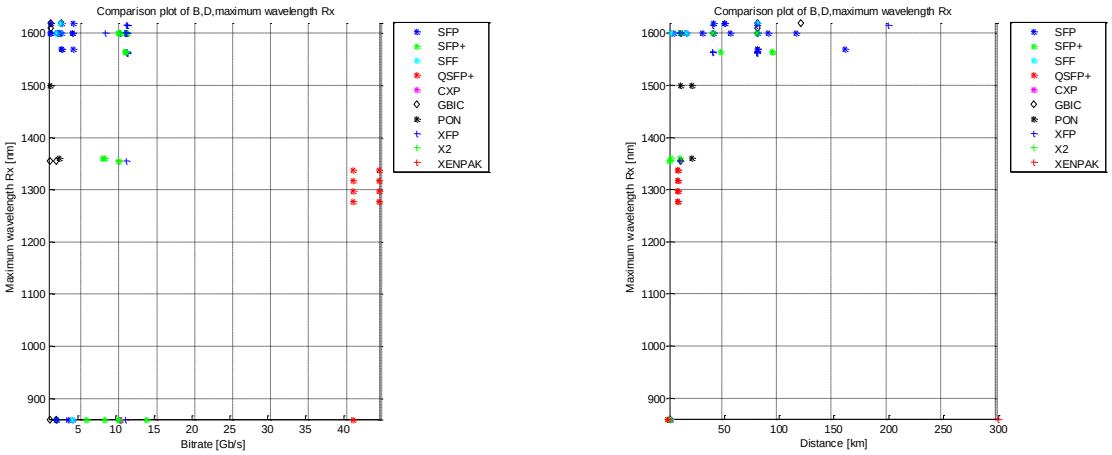

Figure 25 Maximum wavelength of the receiver versus bitrate (left) and transmission distance (right), for different packages

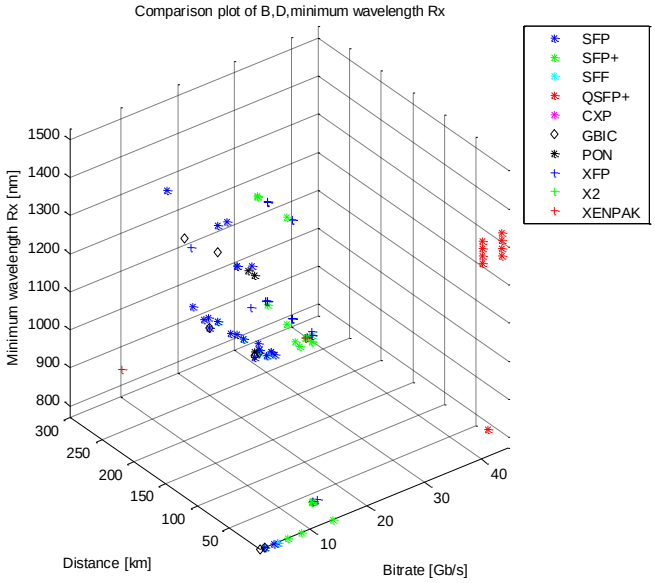

Figure 26 Comparison plot of bitrate, distance and minimum wavelength of the receiver

As in the case of maximum and minimum wavelength of the transmitter, the wavelengths of operation are for the C and L band. It is important that, in the receiver side, the range of tunability is wider that in the transmitter side in order to compensate deviations that can occur in the transmitter laser. One can also depict that the SFP package is the one that includes more products and that as the most diversified tuning range options.

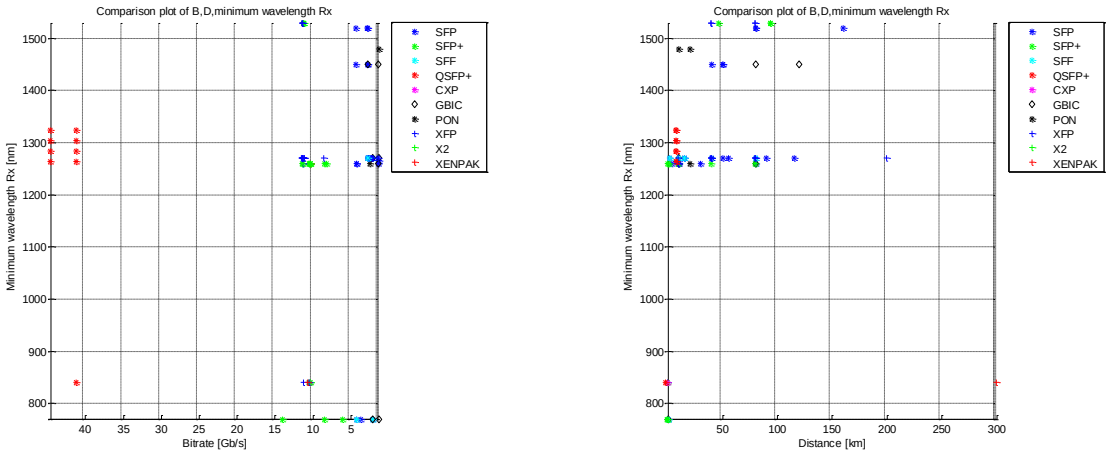

Figure 27 Minimum wavelength of the receiver versus bitrate (left) and transmission distance (right), for different packages

3 PHOTONIC INTEGRATED CIRCUIT COMPONENTS

It is well known that the Internet traffic has grown drastically. The fact that service providers want to sell better quality services, together with a proliferation of video services, leads to the need of higher data rates for the broadband optical access networks. A solution to improve the quality of the service is to combine TWDM and PONs. In FSAN's meeting in April 2012 TWDM was selected to be a primary solution for NG-PON2. [16] In TWDM-PON architecture are used four channels with a different wavelength each. The channel spacing is 100 GHz and the Optical Line Terminal (OLT) transmits 4x10Gb/s (downstream) and receives 4x2.5Gb/s (upstream).Both OLT and Optical Network Unit (ONU) should be tunable over the band of the used wavelengths. Another option to improve the spectrum management as well as the system performance is to use advanced modulation formats. In the deployed and tested systems, the modulation format in use is On-Off Keying Non Return to Zero (OOK-NRZ) mostly for a matter of hardware and implementation simplicity. If one wants to improve the bandwidth of the system, modulations formats such as QPSK can be used at the expense of an increase of system and hardware complexity. Integrated transmitter and receivers that work with QPSK modulation format were already reported. [17] [18].From this state of the art literature one can deduct that the use of advanced formats of modulation such as QPSK will be the next trend in the development of optical transceivers and systems.

In order to allow a large-scale deployment of hybrid PONs, technology development of the optical modules has to be done so that manufacturability and cost effectiveness are achieved. OLT is part of this technology that needs to be further developed. Inside an OLT there are several transceivers. The cost of the transceivers can be further reduced if there were integrated versions whose design is considered to be a very challenging task. A motivation for integrated transceivers is also the fact that integration is a breakthrough towards the reduction of the footprint. A block diagram of a transceiver is presented in Figure 28. In order to design a PIC, the building blocks have to be studied, simulated and modeled for each specific application. This chapter presents the different PIC components not only from a theoretical point of view but also from the application perspective. The main target of this thesis is to understand the components that are the building blocks of a final designed product: a PIC transceiver for hybrid PONs, i.e. PONs that combine WDM and advanced modulation formats.

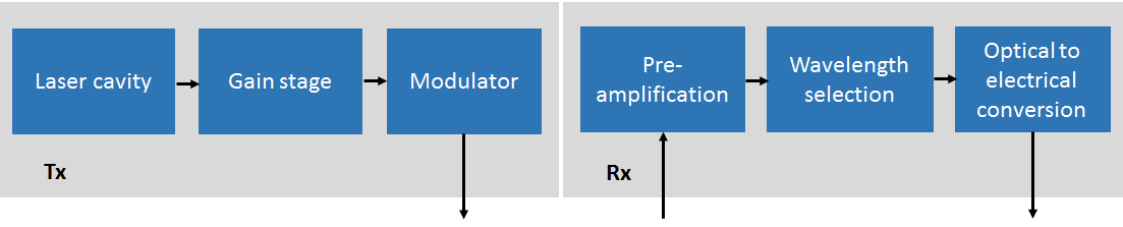

Figure 28 Block diagram of a general transceiver

3.1 Semiconductor Optical Amplifier

The SOA is an active optical circuit element that resembles a semiconductor laser in a sense that both SOA and laser have an optical gain, which is caused by the recombination of electrons and holes that are injected by external current. The main difference between them is that a SOA operates at a higher current density than a laser at threshold.

The first studies on SOAs are back to the 1960s and those first devices were based on GaAs homojunctions operating at low temperatures [19]. Historically, the research on the optical amplifier field is completely related to the research on semiconductor lasers. Most of the research was carried using InGaAsP/InP that produce amplifiers with optical gain in the 1300 to 1600 nm wavelength range. This is one of the reasons why most of the optic transmission systems work in this wavelength range [20]. Nowadays, SOA technology is evolving with an interest in functional applications e.g. photonic switching [19].

3.1.1 SOA Operating Principle and Description

In the semiconductor optical amplifier structure, the active region conveys gain to the input signal. With the use of an external current source, gain is enabled to take place. In order to confine the propagating light in the device, an embedded waveguide is used as one can see in Figure 29 .However, this confinement is weak. Therefore part of the signal is lost into the surrounding cladding regions. The amplification process itself adds noise thus additive noise cannot be avoided. Ripples in the gain spectrum cannot also be avoided as they are introduced by the amplifier facets.

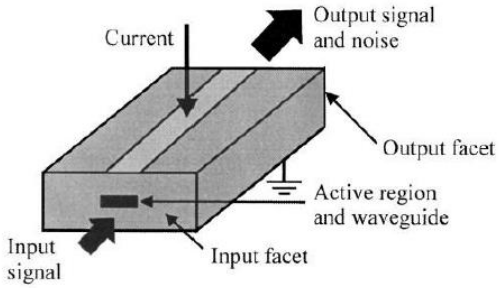

Figure 29 Schematic diagram of an SOA [19]

When an external current source injects carriers in the active region of the SOA, these energized carriers occupy states on an excited state known as conduction band (CB), leaving holes in the ground state that is known as valence band (VB). The population in the ground state will be referred by N_g and the population in the excited state by N_e. From the moment when the

carriers are excited onwards three radiative mechanisms are possible in the semiconductor. These are shown in Figure 30 for a material with an energy band consisting of two discrete energy levels E1 corresponds to the energy on the ground state and E2 to the energy on the excited state.

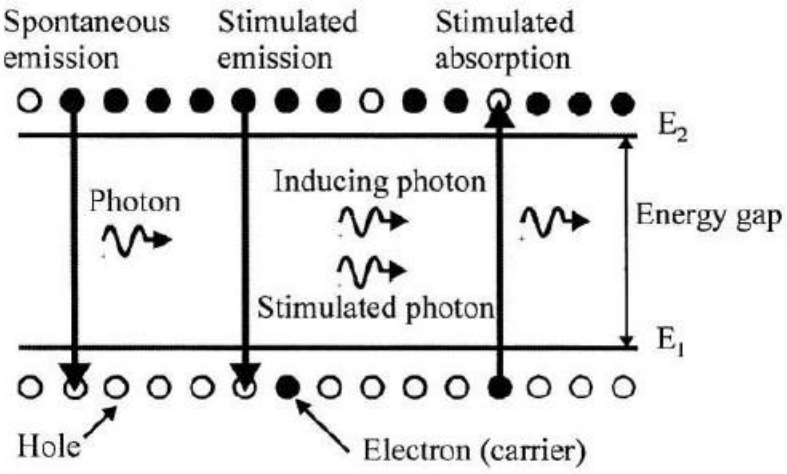

Figure 30Spontaneous and stimulated processes in a two level system [19]

The first mechanism is stimulated absorption. This is a loss process because the incident light photon, which has enough energy to stimulate a carrier from the VB to the CB, is extinguished when this mechanism occurs. The second mechanism is stimulated emission. It occurs when an incident photon has such energy that causes stimulated recombination of a CB carrier with a VB hole. This mechanism is the basis of light amplification: the recombining carrier loses its energy in the form of a photon of light that is identical to the induced photons (in phase, frequency and direction). If the injected current is sufficiently high then a population inversion occurs, i.e. N_e (carriers in excited state) is greater than N_g (carriers in the ground state). In this case the probability of occurring stimulated emission is greater than stimulated absorption, thus the semiconductor will exhibit optical gain. The third and last mechanism is spontaneous emission. This phenomenon is explained by the existence of a probability that a carrier in the excited state spontaneously recombine with a hole in the ground state, emitting a photon with random phase and direction. These photons have a wide range of frequencies and are essentially noise. One can then conclude that as N_e increases the noise also increases and the likelihood of stimulated absorption to occur reduces. One can also verify that the gain is proportional to the difference N_e-N_g (as the difference increases gain also increases) [19].

3.1.2 Optical and SOA Gain

The optical gain depends on several parameters such as frequency and intensity of the incident signal. In order to analyze the gain of the medium, it can be modeled as a two-level system equal to the one studied on the previous subsection. The gain coefficient (gain per unit length) can be written as [20]

$$g(\omega) = \frac{g_0}{1+(w-w_0)^2T_2^2+\frac{P}{P_S}} \tag{3.1}$$

Where g_0 is the peak value of the gain, w is the optical frequency of the incident signal, $w_0$is the atomic transition frequency, P is the optical power of the input signal, P_s the saturation power of the gain medium and T_2 is the dipole relaxation time which is in the range of 0.1 to 1 ps. The saturation power of the gain medium depends on medium parameters such as recombination time and transition cross section.

For low input power, the ratio of the input power to the power saturation is very small and can be neglected thus Equation 3.1 [20] can be simplified as follows:

$$g(\omega) = \frac{g_0}{1 + (w - w_0)^2T_2^2} \tag{3.2}$$

The gain profile is Lorentzian and has its maximum at a frequency equal to w_0 . The gain bandwidth is defined as full width at half maximum (FWHM) of the gain spectrum, for a typical semiconductor is approximately 3THz. When one considers the amplifiers as single elements with gain G defined as the ratio between the output and input power, one can write [20]

$$\frac{dP(z)}{dz} = g(\omega)P \tag{3.3}$$

Where P(z) is the optical power at a distance z (input defined as z=0). For an amplifier with length L and constant g(ω) a solution of Equation 3.3 can be written in order to define the amplifier gain G (ω) [20]

$$G(\omega) = e^{g(\omega)L} \tag{3.4}$$

All these results are based on the initial assumption that the amplifier is operating with low input power. From Equation 3.1 one can conclude that as the input optical power increases, the gain decreases, and that is the origin of gain saturation. Thus, a need of a mathematical analysis of what happens with the increase of input power arises. Considering that $\omega = \omega_0$and performing an analysis similar to the one presented above one can write [20]

$$\frac{dP(z)}{dz} = \frac{g_oP}{1 + \frac{P}{P_s}} \tag{3.5}$$

In the conditions of an amplifier with length L and gain G, the ratio of the output and input power Equation 3.5 is solved [20]

$$G = G_0 e^{\left(-\frac{G-1}{G}\frac{P_{out}}{P_S}\right)} \quad (3.6)$$

Where $G_0 = \exp(g_0 L)$ is the unsaturated gain of the amplifier. One can then conclude that G decreases as the output power becomes comparable with the saturation power. In order to visualize this dependency, Figure 31 allows one to compare the saturation characteristics under two different values of G_0.

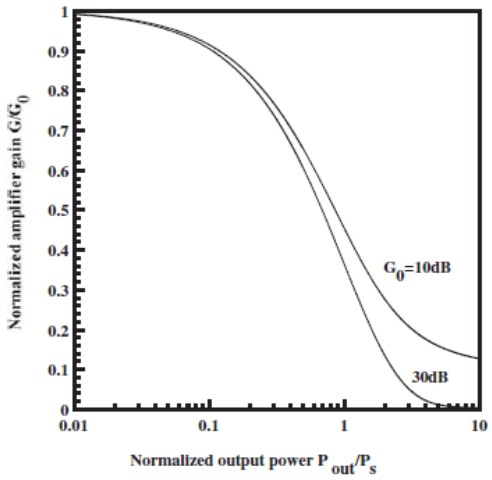

Figure 31 Normalized saturation amplifier gain G/G_0 as a function of the normalized output power [20]

3.1.3 Multiquantum Well Amplifiers

The regular active layer thickness of a SOA is typically 0.1-0.5 μm. However, MQW active layers have a thickness of 100Å or less. In these conditions, the carrier motion is restricted and can be viewed as confined in a one-dimensional potential well. This type of amplifiers are called quantum well (QW) amplifiers. When the active layer is composed with more than one QW, it is considered to be a Multiquantum well (MQW) amplifier. This type of amplifiers has high gain in transverse electric (TE) polarization and high saturation power due to small confinement factor.

Quantum-mechanical effects occur as the thickness of a narrow-gap semiconductor layer confined between two wide-gap semiconductors become comparable to the De Broglie wavelength. Under this condition, the energy of the electrons is quantified in levels E_n. Figure 32 allows one to observe the energy of the electrons and holes when they are confined in a quantum well. In the figure, the energy levels are denoted as E_{1c}, E_{2c}, E_{3c} for electrons; E_{1hh}, E_{2hh} for heavy holes; and E_{1lh}, E_{2lh} for light holes and ħ is the Planck's constant (h) divided by 2π. The calculation of these energies is a well-known problem and for an infinite potential well, the result is [20]

$$E_n = \frac{h^2 n^2}{8 L_z^2 m_n^*} \qquad (3.7)$$

In the equation, m_n^* is the effective mass of the electron on the nth level. With the knowledge of Equation 3.7 and Figure 32, one can conclude that the energy of the emitted photon can be changed by changing the well width L_z.

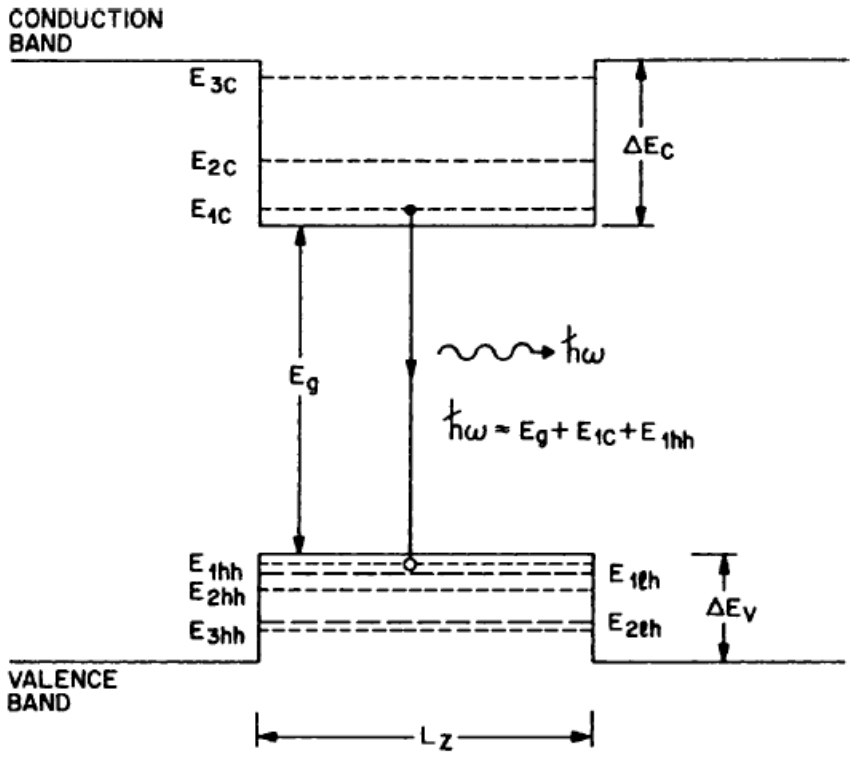

Figure 32Energy levels in a quantum well structure [20]

3.1.4 SOA Modeling

Several authors (e.g. Michael J. Connelly in [21]) have dedicated part of their work to obtain models of different types of SOAs. In the scope of this thesis, the SOA models that were obtained aim to simulate the SOAs of the chosen foundry: SMART Photonics. To do so, SOA parameters were collected in [22] and [23]. The reference for the modeling was set to obtain the gain spectra presented in Figure 33. Thus, the results in this subsection will be performed having it as the base.

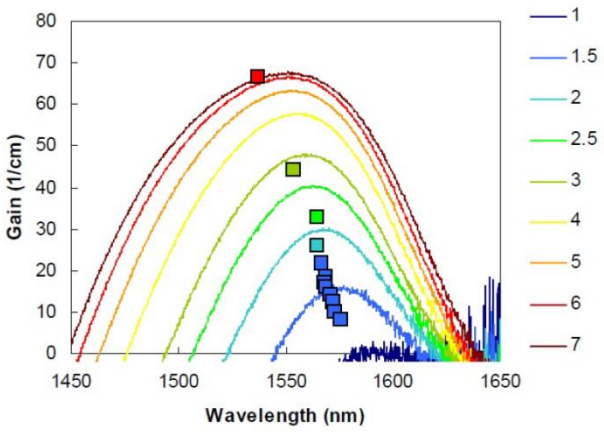

Figure 33 Gain spectra of SOA. The colors indicate the current density in kA/cm² [23]

In order to obtain an accurate model of a SOA, the software VPIphotonics® was used. This software as embedded a block of a SOA with several parameters that can be changed. It is going to be proved that using this block for modeling the SOA is not the best solution. Hence another approach was to use the cosimulation (cosim) feature of VPIphotonics®, which allows the creation of models with the use of Matlab®. This second approach turned also not to be the best solution. A hybrid solution between the first and second method is proved to be the best solution. All of this is discussed in detail in the following subsections.

3.1.4.1 SOA model using VPIphotonics® embedded block

In this subsection, the modeling and simulation of the VPIphotonics® SOA embedded block is presented and discussed. The mentioned block has a vast set of parameters that can be changed in order to model not only physical characteristics of the device but also to improve the simulation where it is used.

The software divides the block parameters in several categories. The ones used in this work were: device structure, optical parameters, carrier dynamics and gain parameters. Device structure allows one to model the physical dimensions of the device and decide either if it is a

MQW or a bulk structure. Optical parameters refer to the parameters that influence carrier losses, confinement and internal reflections. Carrier dynamics, as the category name states, regards how the carrier behaves along the device, defining parameters such as initial carrier density and recombination parameters. The last category is the gain parameters. Within this section, one can define the shape of the gain spectrum (e.g. peak frequency and bandwidth of the amplifier). The parameters of the categories that were not mentioned were left as default, since no information was obtained regarding them. Simulations were done by sweeping their values and their effect was proved not to be relevant in the final gain shape with the exception of parameters Carrier Density, Reference Gain Shape and Carrier Density Reference Index where its final values were the ones that best suit the desired gain shapes. In Appendix A, one can find a table with the chosen full set of SOA parameters.

In order to obtain the gain spectrum, the input and output power of the SOA were measured in order to compute the unsaturated gain of the amplifier (G_0) and obtain the peak value of the gain (g0) at each wavelength using (L is the length of the amplifier)

$$g_0 = \frac{\ln G_0}{L} = \frac{\ln \frac{P_{out}}{P_{in}}}{L} \tag{3.8}$$

The used setup is represented in Figure 34. All the setups on this software have global parameters that allow the user to control the simulation features. In this case the most important is the sample mode center frequency which sets the center frequency of the simulation. The referred parameter was set as player parameter and a sweep using it was done in order to have a full span on the desired wavelengths. Regarding the blocks of the simulation, an input ideal continuous wave with an optical power of 1μW fed the amplifier which its amplitude was measured using a power meter and displayed in a 1D plot for further analysis.

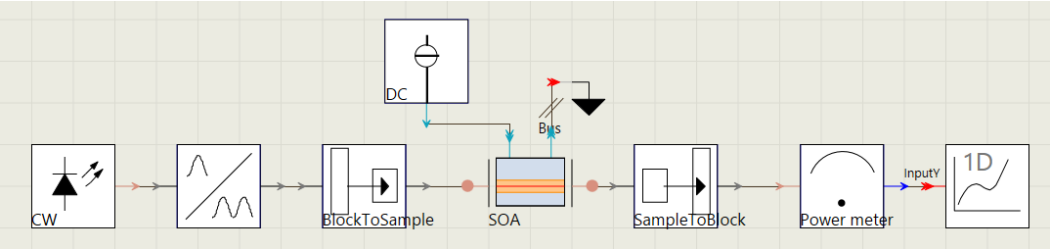

Figure 34 Setup used to characterize the gain spectrum using SOA VPIphotonics® embedded block

The parameters that were used to model the DC source and SOA block are presented in Table 1 and Table 2 respectively. The data was collected in [22] and [23]. In order to obtain different current densities, the value of the DC source had to be changed according to the device dimensions; with it also SOA bandwidth and peak frequency changed as can be seen in Figure 33.

Current density [kA/cm^2]	Current source [mA]	SOA bandwidth [Hz]	Peak Frequency [Hz]
7	168	23.152e12	194.2e12
6	144	22.783e12	194.24e12
5	120	20.379e12	193.9e12
4	96	18.698e12	193.2e12

Table 1 Current source parameters and SOA current density dependent parameters

Category	Parameter	Value	Unit
Device structure	Active Region Type	MQW	n.a.
	Device Section Length	1200e-6	m
	Active Region Width	2.5e-6	m
	Active Region Thickness MQW	84e-9	m
	Active Region Thickness Separate Confinement Heterostructure (SCH)	208e-9	m
Optical parameters	Confinement Factor MQW	0.054	n.a.
	Confinement Factor SCH	0.56	
	Optical Coupling Efficiency	0.9772	
Carrier Dynamics	Linear Recombination	600e-12	1/s
	Biomolecular Recombination	2.62e-16	m^3/s
	Auger Recombination	5.27e-41	m^6/s
	Initial Carrier Density	5e24	1/m^3
Gain Parameters	Gain Coefficient Linear	3.5e-20	m^2
	Carrier Density Transparency	0.4e24	1/m^3
	Gain Shape Model	Parabolic	n.a.
	Gain Peak Frequency	*	Hz
	Gain Bandwidth	*	Hz
	Carrier Density Reference Gain Shape	6e24	1/m^3
	Carrier Density Reference Index	1e24	1/m^3

Table 2 SOA modeled parameters (* seeTable 1)

In the gain spectra of Figure 33 one can see nine gain shapes. However, in the simulation work, only the four corresponding to the highest current densities were studied. This was due to the fact that in the future setups, where this blocks will be used, only the highest current densities are of interest due to their higher gain and stability. The data obtained with the setup presented before, was processed in Excel® and Matlab® in order to be compared with the original gain shapes. The result is presented in Figure 35.

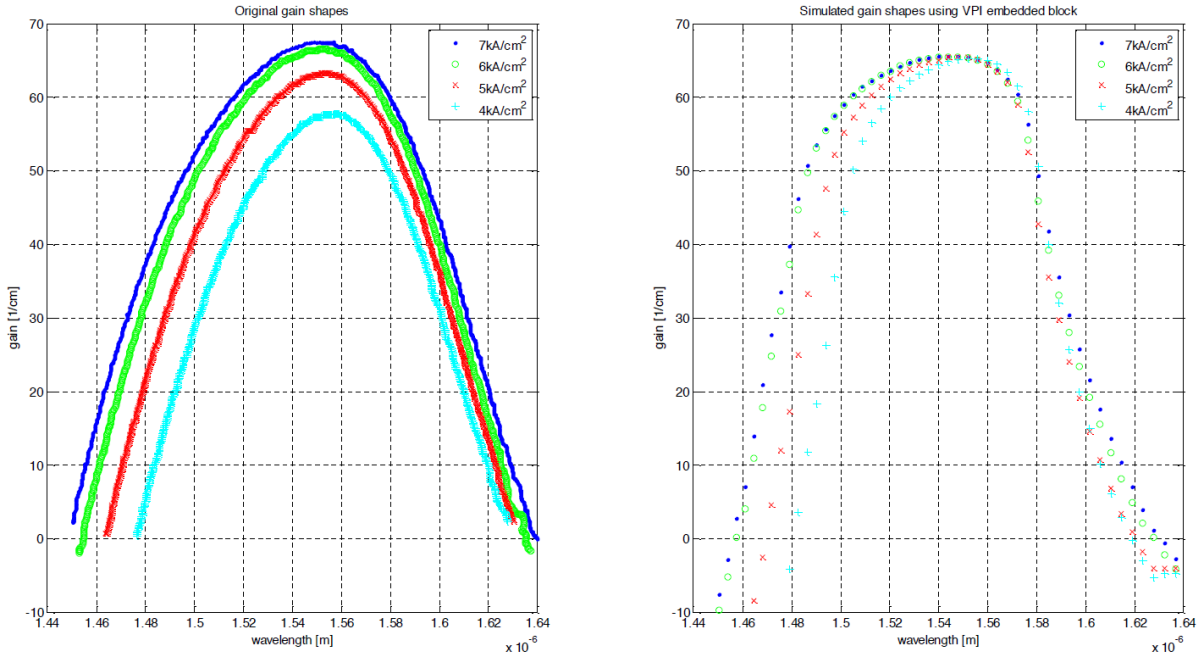

Figure 35 Original SOA gain shapes (left) and obtained SOA VPIphotonics® embedded block gain shapes (right)

From inspection of Figure 35 one can see that the measured gain shapes do not perfectly match the original gain shapes. The curve that best approaches the original gain shapes is the 7kA/cm^2 curve. In the original gain shapes, it is seen that as the current density decreases, the gain shapes is broadened and the gain peak decreases in amplitude and is shifted in the spectrum. In the simulated gain shapes, these behaviors do not occur in the same manner. One can observe the gain peak shift in the spectrum but in terms of magnitude, the behavior, is in part altered. As stated before, the gain profile of a SOA is Lorentzian and in the block the gain shape model was set to parabolic. The other possible option beyond parabolic was to set it flat which would further differ from the Lorentzian behavior. The gain peak shift can also be explained with the fact that the SOA block, is a numerical block that tries to suit as much as possible the real SOAs through its equations and nonlinear behaviors. In this case, the original gain shapes were for a specific foundry in initial conditions that were not taking into account in this model which can alter the global gain shape of the system.

This solution proved not to be the best in terms of modeling a specific SOA. The simulation software provides an interface where one can describe the behavior of the blocks using Matlab® code and use it on more complicated setups. This method is further explained in the next subsection.

3.1.4.2 SOA model using VPIphotonics® cosimulation features

Cosimulation is a technique that uses other software besides VPIphotonics® to handle part of the simulation. In this case, the used software is Matlab®. The setup resembles the one used in the previous subsection and is represented in Figure 36.

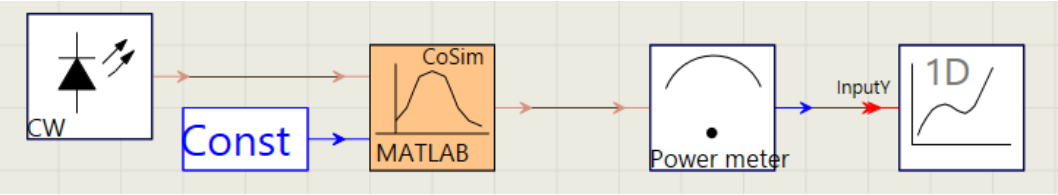

Figure 36 Setup to characterize using VPIphotonics® cosim feature

Despite the block that describes the SOA behavior, the others remain unchanged when compared to the previous setup. The cosim block has two inputs: one is the optical signal and the other is a constant value parameter that allows the user to define the current density. Inside the block, the Matlab® code initially deals with the optical signal characteristics such as sample rate and noise bins frequency. For each sample, a Matlab® function, which contains the modeled mathematical expressions for the different gain shapes, is called. The modeled mathematical expressions were obtained with the use of Excel® tools to fit curves.

The simulation procedure in this setup was the same of the one presented before. The results are shown in Figure 37.

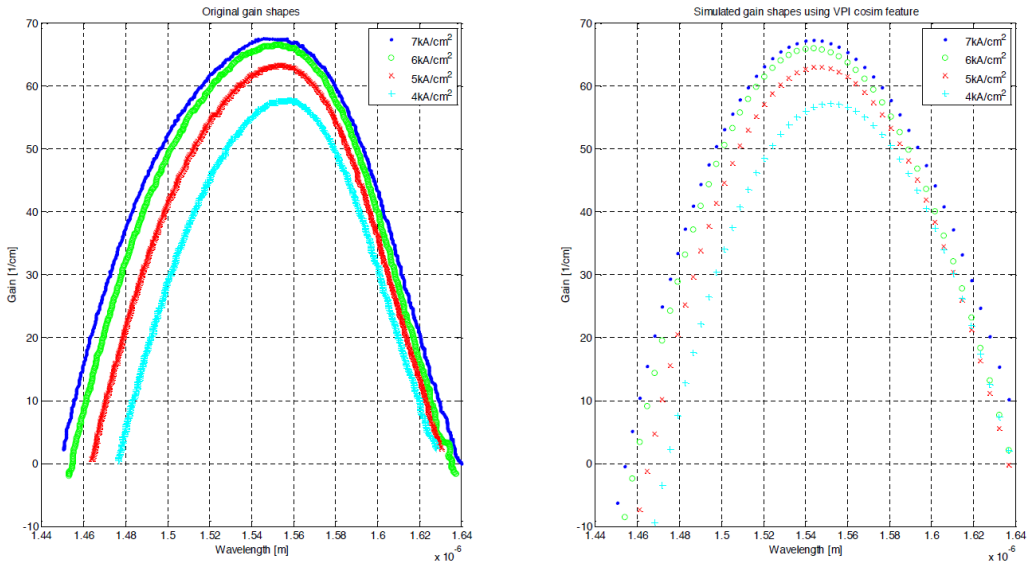

Figure 37 Original SOA gain shapes (left) and obtained SOA gain shapes using cosim feature (right)

When one compares the original and the simulated gain shapes, one can conclude that they resemble to each other. This result was expected, since the core of the Matlab® block is the transfer functions mathematically modulated using the original gain shapes. The objective of obtaining the original gain shapes can be considered as completed. However one can easily conclude that this block is incomplete because if it is used in a more complete setup to simulate larger blocks, the global output will not be realistic. In a mathematical point of view, this block can be considered as a filter with a defined transfer function, thus the block does not behave as a SOA in terms of gain saturation, spontaneous emission and nonlinear effects. Nevertheless, it can be considered a good starting point to obtain the desired gain shapes. A method to introduce the SOA characteristics such as spontaneous emission is to combine the two presented methods, i.e. a setup with a combination of a Matlab® block and an embedded SOA VPIphotonics® block where the former provides the gain shape and the latter provides the SOA characteristics. The tradeoff between their characteristics, the setup and the results are presented in the following subsection. This method is called onwards the hybrid solution.

3.1.4.3 SOA model using hybrid solution

Within this method, the paradigm to obtain the SOA model remains the same. In sum, in the first case, the obtained gain shapes were not as expected and on the second case, although the gain shape was the desired, the block does not completely represent a SOA.

The hybrid solution setup is represented in Figure 38.The considerations made above about all the blocks, except the SOA and the cosim, remain unchanged.

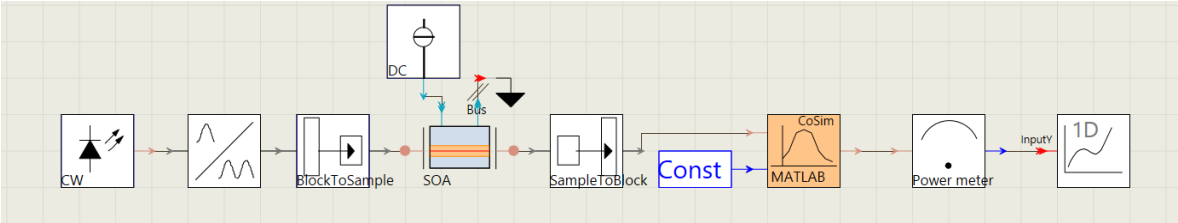

Figure 38 Setup to characterize SOA gain shape using hybrid solution

When assembling this setup, one must be aware of the tradeoff between the gain of SOA and cosim block. Initially, both of them were designed to provide the desired gain shapes. If their characteristics were not changed, the result would not be as expected. Thus, the option made was to set the parameter *Gain Shape Model* of the SOA as flat, which will provide a constant gain through the spectrum, instead of the parabolic shape. The gain provided by the SOA block has to be compensated on the gain of the cosim block in order to, at the end, have the same gain shape. The factor that was compensated is given by:

$$factor = \frac{G_c(1-G_S)}{G_s} \quad (3.9)$$

Where G_c is the gain of the cosim block which was given by the modeled equations and G_s is the SOA gain. This flat gain had to be measured before and processed in the same way, as it was done with the setup of Figure 34. The question that arose was the magnitude of the gain that the SOA should provide. If the SOA had a small gain, a big factor will appear to compensate it at the cosim block, which was not a problem. The problem was in the fact that with small SOA gain, the saturation and spontaneous emission would not be as desired for the gain shapes. The same occurs in the case that SOA provides a gain in the magnitude of the peak gain as in the case of the single embedded block setup. In that situation, although the cosim block could correct the shape, the undesired characteristics would appear. In order to obtain the most suitable value for the SOA a sweep was done with several values of the gain and the result for the linear gain coefficient was 2.1e-20 m^2. The result is provided in Figure 39. One can conclude that the simulated gain shapes resemble the original ones and the behavior of the SOA, as a whole, was taken in consideration thus this model can be used to simulate photonic integrated circuits (PICs) of the SMART Photonics foundry.

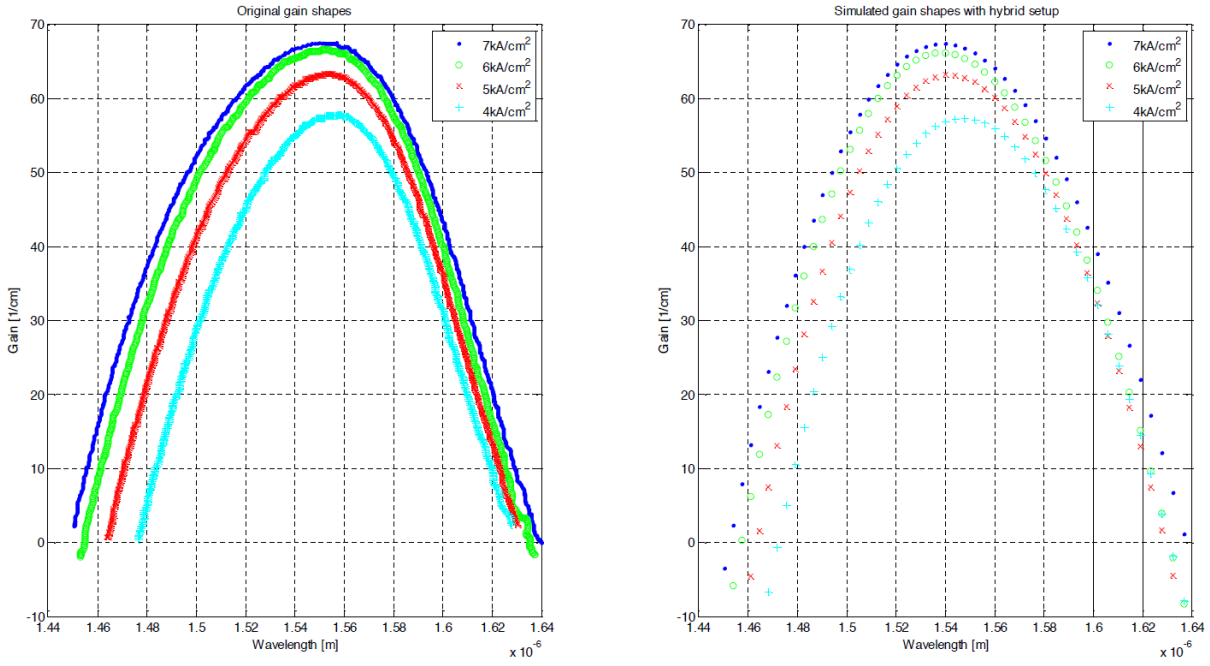

Figure 39 Original SOA gain shapes and obtained gain shapes with hybrid solution

3.2 Arrayed Waveguide Grating

AWG is an optical planar passive device whose applications can vary from wavelength routing to wavelength multiplexing. It is as an imaging device. This means that the field at the array of output waveguides is the image of the field at the input obtained in a dispersive way [24]. AWGs are considered to be an example for optical integration that eliminates the hard work of hand assembly of optical devices [25]. This fact was a motivation on the work done through the years to evolve its architecture and design.

In the literature, AWGs are also known as Phased Arrays (PHASARs). PHASARs demultiplexers were first reported in 1988 and from that moment on, several devices were developed. First, for operation in short wavelengths and then in the long wavelength window. These devices had one input to N outputs. The evolution to N inputs and N outputs was presented by Dragone in 1991. The latter case are the so called wavelength routers which are nowadays used in several multiwavelength network applications [24]. With the development of technology and optical integration, AWGs capable of multiplexing up to 1080 channels with 25-GHz spacing have been reported [26]. AWGs offer many advantages for use such as compactness, fabrication stability, reliability and reduced cost of fabrication and packaging. They also offer high precision on the control of channel spacing enabling its compliance with the ITU-T. [27]

3.2.1 Operating Principle and Description

AWG is composed by: input and output waveguides, two Free Propagation Regions (FPRs) and a phased array of multiple channel waveguides with a constant path difference between neighboring waveguides. A layout of the device is presented in Figure 40.

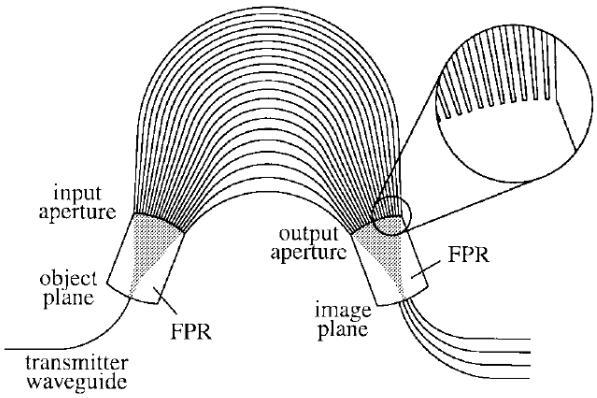

Figure 40Layout of AWG demultiplexers [24]

As an operating point overview one can state that the light inputs in the FPR through the transmitter waveguide and gets diffracted. After that it gets coupled to the waveguides of the array structure. Because the length of each individual waveguide of the array is different, the light inputs in the output FPR in such manner that different wavelengths get focused at different points. This will lead to different wavelengths being coupled to different output waveguides.

The choice of the length of the array waveguides is such that the path length difference between adjacent waveguides is equal to an integer multiple of the central wavelength of the device. For the central wavelength, the fields in the individual waveguides, will arrive at the output aperture with the same phase. The divergent beam at the input aperture is transformed into a convergent one at the output. They both present the same amplitude and phase distribution. An image of the input field at the object plane will be formed in the center of the image plane (see Figure 41). Phase change induced by a change in the wavelength varies linearly along the aperture. This is due to the linear increase of the length of the array waveguides. Because of this fact, the outgoing beam is tilted and the focal point shifts along the image plane thus by placing receiver waveguides properly along the image plane one can obtain spatial separation of the different wavelength channels.

The length difference ΔL between adjacent array waveguides enables focusing. As explained before it should be equal to an integer number of wavelengths and is given by [24]

$$\Delta L = m\frac{\lambda_c}{N_g} \tag{3.10}$$

where m is the order of the phased array, λ_c is the central wavelength and N_g is the effective index of the waveguide mode. By chosing this, the array acts as a lens with image and object planes at a defined distance of the array apertures. This distance is denoted by R_a in Figure 41. This figure depicts a Rowland-type mounting where the receiver waveguides should be positioned along a circle with radius half of R_a.

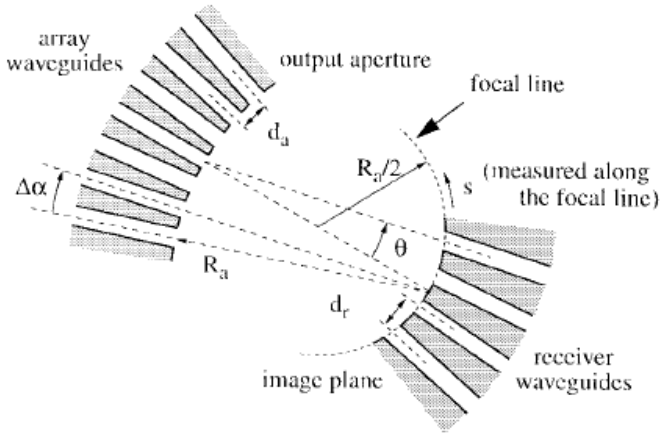

Figure 41 Geometry of the AWG at the receiver side [24]

In Figure 41 it is also shown the dispersion angle θ that results from the phase difference $\Delta\Phi$ between adjacent waveguides. Its relation is given by [24]

$$\theta = \text{asin}\left(\frac{\frac{\Delta\Phi - m2\pi}{\beta_{FPR}}}{d_a}\right) \approx \frac{\Delta\Phi - m2\pi}{\beta_{FPR} d_a} \tag{3.11}$$

in which $\Delta\Phi = \beta\Delta L$ and β, β_{FPR} are the propagation constants of the waveguide mode and the slab mode in the FPR respectively; d_a is the lateral spacing of the waveguides in the array aperture. In the mentioned figure it is also shown $\Delta\alpha$, which is the ratio of d_a to R_a. It defines the divergence angle between the array waveguides in the fan-in and fan-out sections.

From analysis of Equation (3.**11** one can conclude that the response of the phased array is periodical. After each change of 2π in the phase difference between adjacent waveguides the field will be imaged in the same position. The period in the frequency domain is called the free spectral range (FSR) and is defined by [24]

$$\Delta f_{FSR} = \frac{c}{\tilde{N}_g \Delta L} = \frac{f_c}{m'} \; with \; m' = \frac{\tilde{N}_g}{N_g} m \tag{3.12}$$

in which $\tilde{N}_g$ is the group index of the waveguide mode and m' can be interpreted as the order of the beam.

As the far-field intensity of the individual waveguides reduces away from the center of the image plane the focal sum-field will do the same. The central and outer channels do not have the same intensity, thus one can define nonuniformity as the intensity ratio (in dB) between the central and outer channels. In the case when the device has N inputs and N outputs and the FSR equals N times the channel spacing, nonuniformity will be close to 3dB for reasons of power conservation [24]. The insertion loss is mainly due to the diffraction of light into undesired orders. It is proved that in order to have low losses, the waveguide spacing d_a in the array apertures should be as small as possible [24].

Another parameter that is relevant in AWGs is the channel crosstalk. It can be caused by several mechanisms that go from fabrication to design imperfections. In the literature the most common definition is the single channel crosstalk figure. It is the maximum crosstalk value which is measured with one active input channel. There are six mechanisms that cause crosstalk discussed and presented by Smit in [24]. The first one is the receiver crosstalk which represents the coupling between the receivers due to the tails of the field distributions. Another mechanism is truncation. In an ideal case the field would not be truncated but as in the AWG the array aperture is finite, truncation causes crosstalk. Mode conversion is also a mechanism of crosstalk. If the waveguides are not strictly single mode, "ghost" images can appear due to the excitation of the first order modes in the junctions between straight and curved waveguides.The fourth mechanism is coupling in the array. It is induced due to the coupling in the input and output sections in the arrays. The last two mechanisms presented are caused by fabrication

imperfections. The first one is phase transfer incoherence, and is simply explained by the incoherence in the array caused by fabrication imperfections and the second one is background radiation which is due to light scattered out of the waveguides at junctions or rough waveguide edges.

3.2.2 Overview of AWG Applications

3.2.2.1 Wavelength routers

AWGs can be used as wavelength routers when they present a geometry of N inputs and N outputs and its FSR equals N times the channel spacing. For wavelength routing each of the N input ports carry N different wavelengths such that output channel 1 carries wavelength N and channel 1 wavelength N. In the remaining inputs, the wavelengths are distributed in the same way but cyclically rotated by 1 channel as can be depicted in Figure 42.

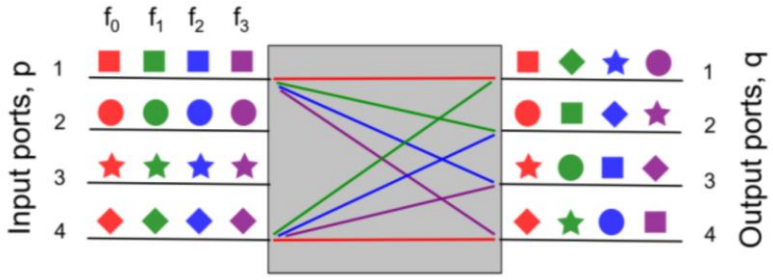

Figure 42 Default wavelength routing rules in an AWG[28]

If one wanted to realize this operation without an AWG, a considerable amount of switch would be necessary.

3.2.2.2 Multiwavelength lasers

Multiwavelength lasers using AWG configuration were first presented by Zirngibl and Joyner [24] and are nowadays widely used specially in integrated optics. A multiwavelength laser consists of an array of broadband SOAs with a multiplexer in a Fabry-Perot cavity. If one or more of the SOAs are excited, the device will start lasing at the passband maximum of the multiplexer at which the SOAs are connected. An important feature of this application is that the different channels are tuned by the AWG and coupled to the fibre, with low loss.

3.2.2.3 Add-drop multiplexers

AWGs can be used as add-drop multiplexers which form a class of wavelength selective switches. Add-drop multiplexers are used to couple the signals at the main input ports to the

drop ports by operating the proper switches. The same is done on the reverse way, i.e. the signals applied at the add ports are routed to the drop ports.

3.2.3 AWG Design and Modeling

The goal of this subsection is to present the design of AWGs for integrated optic circuits. For the designed AWGs, models were created in the VPIphotonics® software.

In the transmitter architecture, the laser cavity is an important building block. An approach to design a multiwavelength laser was presented in the previous subsection. An AWG is used in order to tune the desired wavelength of the channels and the use of SOAs allows the switching among the channels. As explained before, the spectrum of the AWG is periodic in the frequency according to its FSR. This property leads to a problem in the desired application since the spectrum of the lasers will have these repetitions. A simple solution to remove these copies is to add another AWG in the way of the light between the SOAs and the reflectors. This AWG has to have such a transfer function that is passband in the desired lasing wavelengths and stop band in the copies. The AWG that does the tuning of the desired channels is ahead called Tuning AWG (T-AWG) and the one that rejects the copies is onwards called Rejection AWG (R-AWG).

In terms of the transmission parameters, in order to have a WDM grid with spacing of 0.8nm (100GHz at wavelength operation of 1550nm) was chosen and a central wavelength such that one of the channels is 1550nm. This wavelength was selected because is the maximum region gain of the SOAs and the standard fibre have less losses in this region. In terms of channels the T-AWG is 1x4 thus, four different wavelengths will be tuned: 1549.2nm, 1550nm, 1550.8nm and 1551.6nm. The choice of these wavelengths is related to the design of the 3dB directional coupler that is presented in the subsection: 3.5.2 : Directional Coupler Design and Results.

3.2.3.1 AWG design

The AWG design was done with the use of Advanced Simulator for Photonic Integrated Circuits (Aspic®) software. This software enables the analysis of optical circuits without restrictions in dimensions and complexity. The process for simulation and design of the components is based on drag and drop. The software provides different libraries according to the different available foundries where SMART photonics is included.

The AWG model presented in the software provides a set of parameters that can be defined in order to describe its geometry and transfer function. The target to design the T-AWG was to obtain the above stipulated channels and a crosstalk of around -30dB, in order to have low interference between the channels. The size of both AWGs was also a key-factor. As the main goal was to use them in an optical chip, the footprint should be reduced as much as possible. In order to reduce the size of the AWG the FSR should be kept as low as possible. One should also

take in consideration that both spectra should fit as explained above. Thus there is a tradeoff between the FSR of both AWGs.

The modeled parameters were: number of inputs, number of outputs, central wavelength, channel spacing, FSR, input/output waveguide width, spacing between input waveguides, array waveguide width and Rowland I/O mounting. The first four were already discussed and were fixed parameters. Regarding the Rowland I/O mounting it represents a flag with which the user can choose geometry to the FPR similar to the one in Figure 41. The array waveguide width was left as default in order to ease the fabrication process. The input/output waveguide width was set to the value of the waveguides width of the chosen foundry. The remaining parameters were obtained by sweeping their values. In one hand the desired FSR is as big as possible in order to have as less replicas as possible on the other hand, the bigger the FSR the bigger the device which one shall avoid specially in the design of an optical chip. The spacing between input waveguides is the geometrical parameter represented by dr in Figure 41. The spacing between input waveguides influenced the crosstalk of the transfer function, the greater the dr the lower the level of crosstalk. Whereas the increase of this parameter also increases the size of the device thus the desired crosstalk was obtained at the cost of an increasing of size.

In Table 3 one can find the parameters of the T-AWG:

Parameter	**T-AWG**	**Unit**
Number of inputs	1	n.a.
Number of outputs	4	n.a.
Central wavelength	1.5504	µm
Channel spacing	100e9	Hz
Free spectral range	1400e9	Hz
Input/output waveguide width	2	µm
Spacing between input waveguides	5.5	µm
Array waveguide width	1.5	µm
Rowland I/O mounting	Yes	n.a.

Table 3Parameters of T-AWG

The result simulated spectrum and a detail on the desired channels is presented in Figure 43 and Figure 44 respectively.

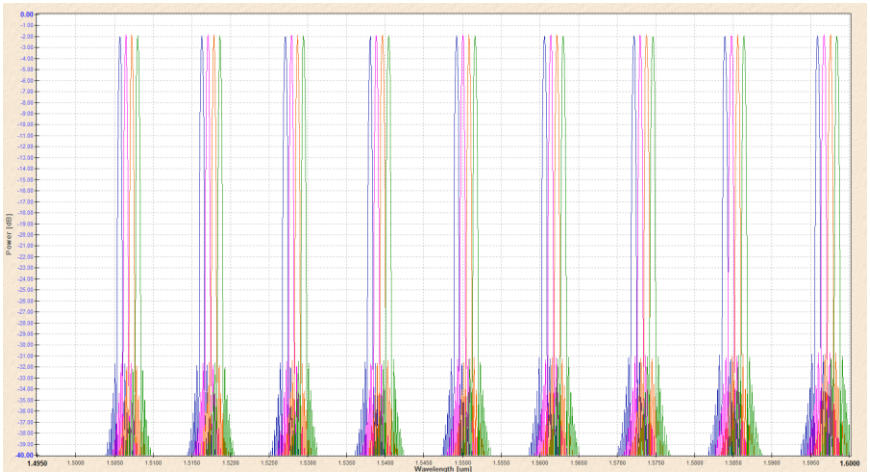

Figure 43 Simulated spectrum for T-AWG

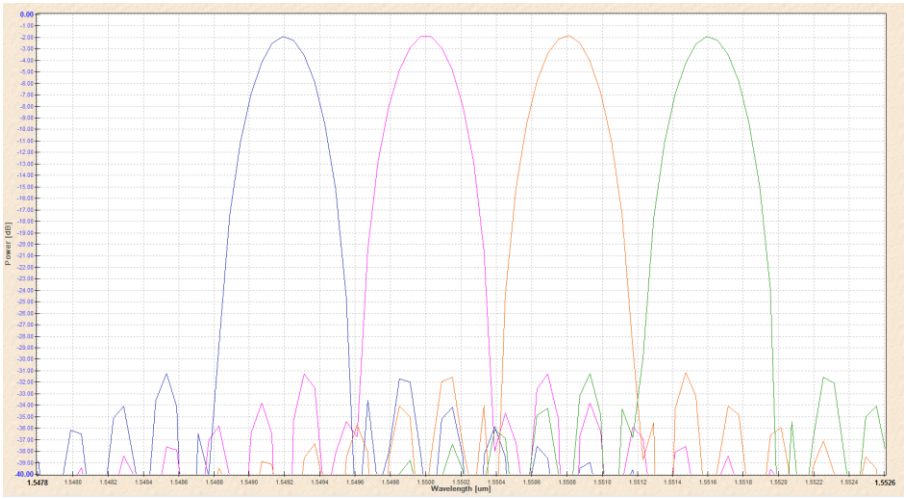

Figure 44 Detail of spectrum of T-AWG

Regarding the R-AWG, the main concern was to suppress the copies using as less space as possible. To do so, in this AWG, the central wavelength was kept the same to be passband in the desired wavelengths. The value for the parameters input/output waveguide width and array waveguide width was left unchanged since the reasoning presented for the T-AWG also applies for this case. The other parameters were obtained through sweeping and simulation of their values.

In Table 4 one can find the values that were used for the R-AWG.

Parameter	R-AWG	Unit
Number of inputs	3	n.a.
Number of outputs	1	n.a.
Central wavelength	1.5504	µm
Channel spacing	180e9	Hz
Free spectral range	1400e9*(5/2)	Hz
Input/output waveguide width	2	µm
Spacing between input waveguides	2	µm
Array waveguide width	1.5	µm
Rowland I/O mounting	Yes	n.a.

Table 4Parameters of R-AWG

As one can see the number of inputs and outputs is changed and the number of the input channels is no longer four. The value could be reduced as long as the transfer function at the output has a bandwidth at least equal to the total at the outputs of the T-AWG. To obtain this, the channel spacing was increased. The spacing between input waveguides was also reduced as the level of the crosstalk in the transfer function of the R-AWG has not the same restrictions as in the T-AWG.

The value of FSR had to be a non-integer multiple of the T-AWG FSR. With it, one can obtain a passband in the central channels and suppress the remaining copies as can be depicted in Figure 45. In bold green is presented the spectrum of R-AWG and the remaining is the already presented spectrum of T-AWG. Thus, only the central channels will be selected for lasing once the images due to the FSR are rejected with the R-AWG.

3.2.3.2 AWG modeling

In order to obtain a model of the presented AWGs, several approaches using VPIphotonics® were done. The main target was to obtain a model that would enable the simulation of more complex schemes where these models could be included. Unlike the case of the SOA, in which the obtained model is easily scalable to be used in all the circuits of the chosen foundry, the models that were obtained for the AWG are only valid for some specific cases which limit the scalability of these models.

The scope of this modeling was to obtain AWGs with the transfer functions that were presented in the previous subsection. VPIphotonics® was used. This software already includes an embedded block for modeling AWG. However this model has several limitations. First of all, it is not bidirectional which is a big constrain when one wants to simulate for example the lasing applications for AWG. In fact, it is possible to build a block with two AWGs that represent a bidirectional one. This example is presented in the tutorials of VPIphotonics® [28]. Unfortunately it turns the simulation slow and can lead to deadlocks during it. Using the embedded bock, one unidirectional model per each AWG (T and R-AWG) was obtained.

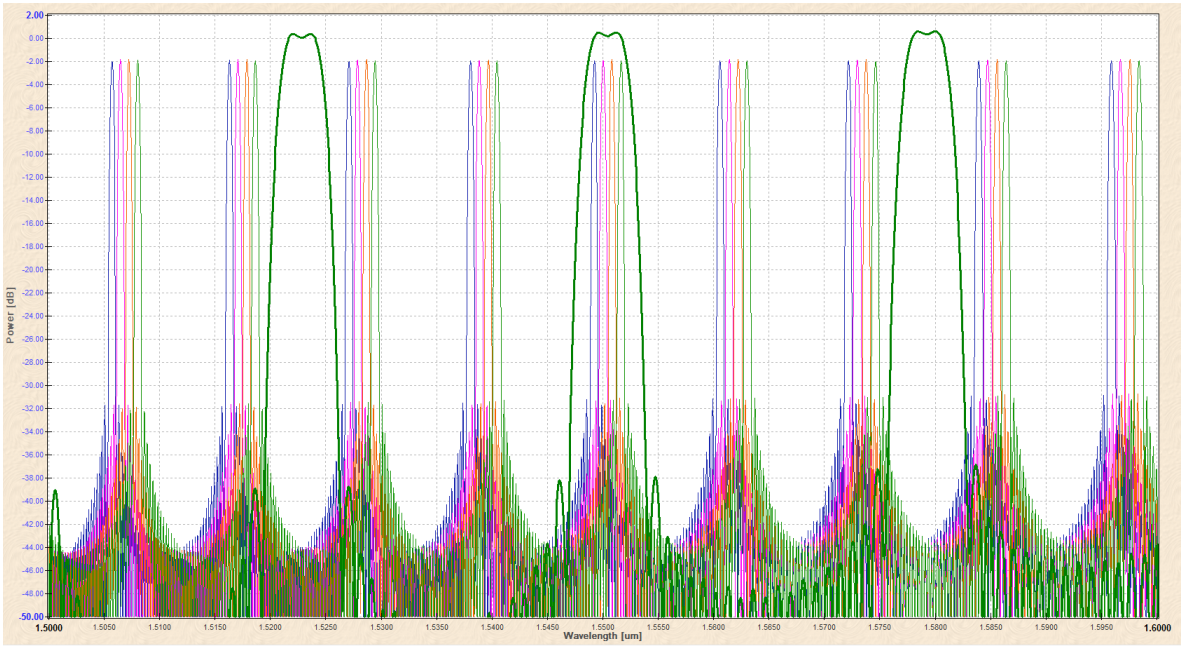

Figure 45 Spectra of T and R-AWG

For the T-AWG the obtained model was the one with one input and four outputs and for the R-AWG one was one input and three outputs so that one can compare the obtained spectra with the ones designed in ASPIC and presented in Figure 45. Bidirectional models were created using cosimulation, by connecting the different unidirectional transfer functions obtained in ASPIC.

3.2.3.2.1 Modeling using VPIphotonics® embedded block

The AWG embedded block, provides a set of categories in which the different parameters can be chosen. The main categories are: geometry, frequencies, passband shape, crosstalk and insertion losses. The category geometry allows one to define the number of input and output ports. The category frequencies define the different channel frequencies, the channel spacing and the FSR. In the crosstalk and insertion losses categories one can define the values of the insertion loss for the different channels and the crosstalk between adjacent and non-adjacent channels. Regarding the passband shape, one can define the shape of the transfer function of the different channels. This definition is done through several parameters such as bandwidth and the shape itself e.g. Gaussian, hyper-Gaussian.

Taking in consideration the parameters presented in Table 3 and Table 4 where one can find the setting for T and R-AWG respectively, the setup presented in Figure 46 was created.

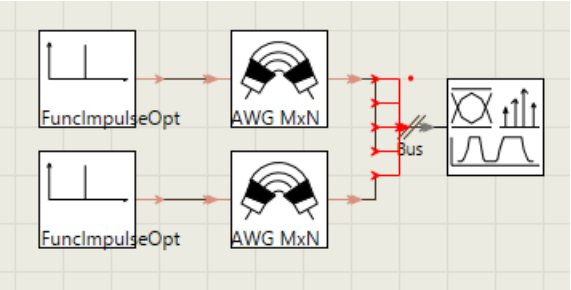

Figure 46 Setup for simulation of AWG embedded block

The AWG presented in the top is the T-AWG. The goal in this simulation was to overlap the spectra of the unidirectional AWGs in order to verify if it will resemble the one presented in Figure 45. The inputs of the AWG are ideal optical impulses. The result is presented in Figure 47. From inspection of the mentioned figure, one can conclude that the simulated models constitute a good approach to the problem. It is worth to mention that the model has the limitation of being unidirectional and that for each AWG in the different applications all the parameters have to be change which is the opposite case of what happened in the SOA case where only the length of the device and the value of the current source needed to be change.

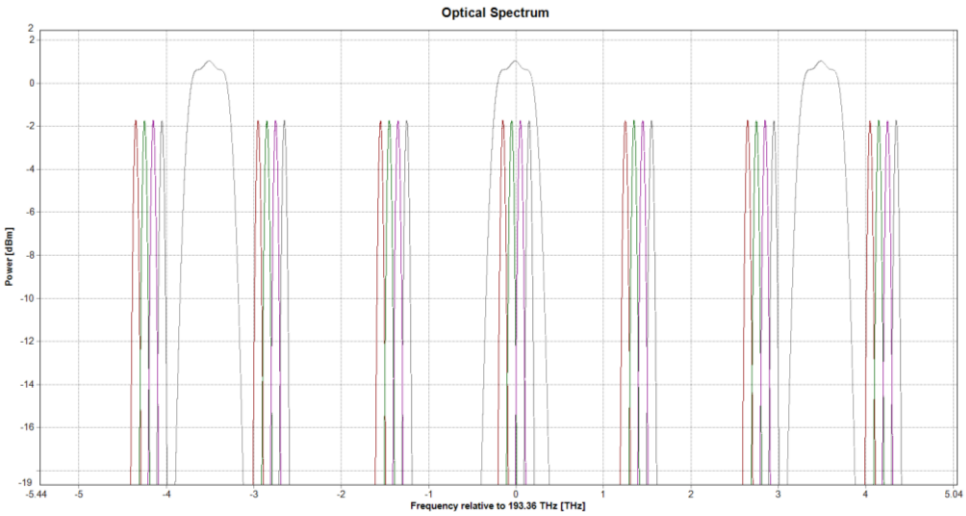

Figure 47 Simulated spectrums of T and R-AWG using VPIphotonics® embedded model

3.2.3.2.2 Modeling AWG using VPIphotonics® cosimulation features

Another approach to obtain a model of a AWG is to use the cosimulation features of VPIphotonics® as it was done with SOA. The models were built using Matlab® description of the measured transfer function in the ASPIC® software. These transfer functions are unidirectional.

Four unidirectional models were then created and then two bidirectional models were assembled.

The ASPIC software provides the feature to export the data of the desired spectrum onto a .mat file that is compliant with Matlab®. In order to obtain the mathematical expression of the transfer functions, a curve fitting was done using the Curve Fitting tool of Matlab®. The approximation done was to the Gaussian shape of the transfer functions of the channels. An example of the inside of a cosim block is presented in Figure 48. On the left side, are the input ports and on the right side are the output ports. The CoSimInputOpt and CoSimOutputOpt are the blocks that convert the optical signal into and out of a Matlab® structure. The CoSim block is the block where the path for the Matlab® file should be provided. This example represents the case of one input and four outputs. One can then conclude that for each output a transfer function is provided i.e. a transfer function per channel. In the case of multiple inputs and one output, the solution is to multiplex the inputs with an ideal multiplexer and then a transfer function is applied.

In order to compare the obtained transfer functions, in the analysis of the results a Matlab® plot with the transfer functions obtained in the ASPIC® software are provided. For the case of the T-AWG the results are presented in Figure 49 and Figure 50.

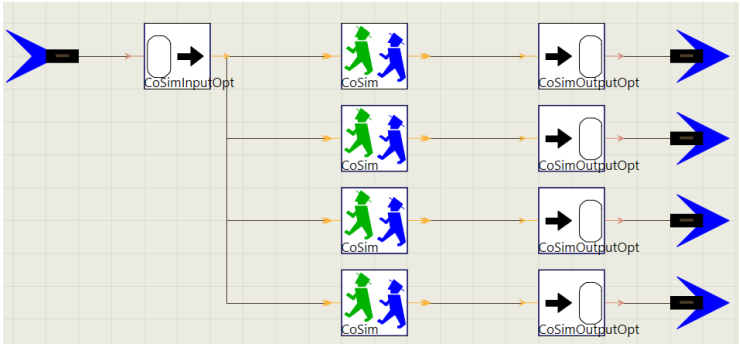

Figure 48 Example of cosim block (one input, four outputs)

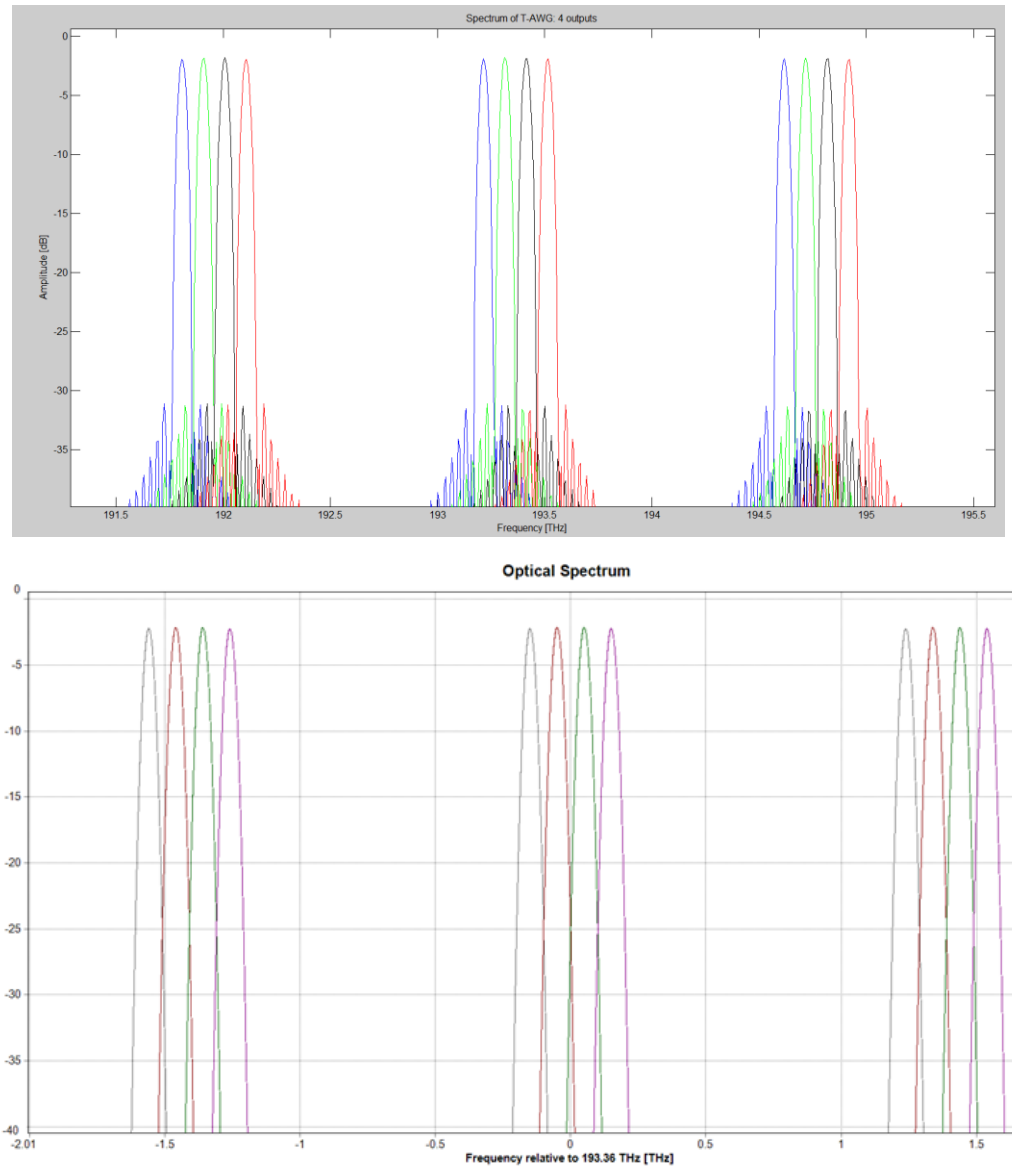

Figure 49 T-AWG spectrum. One input, four outputs. Top: Transfer Function obtained in ASPIC® Bottom: Simulated in VPIphotonics®

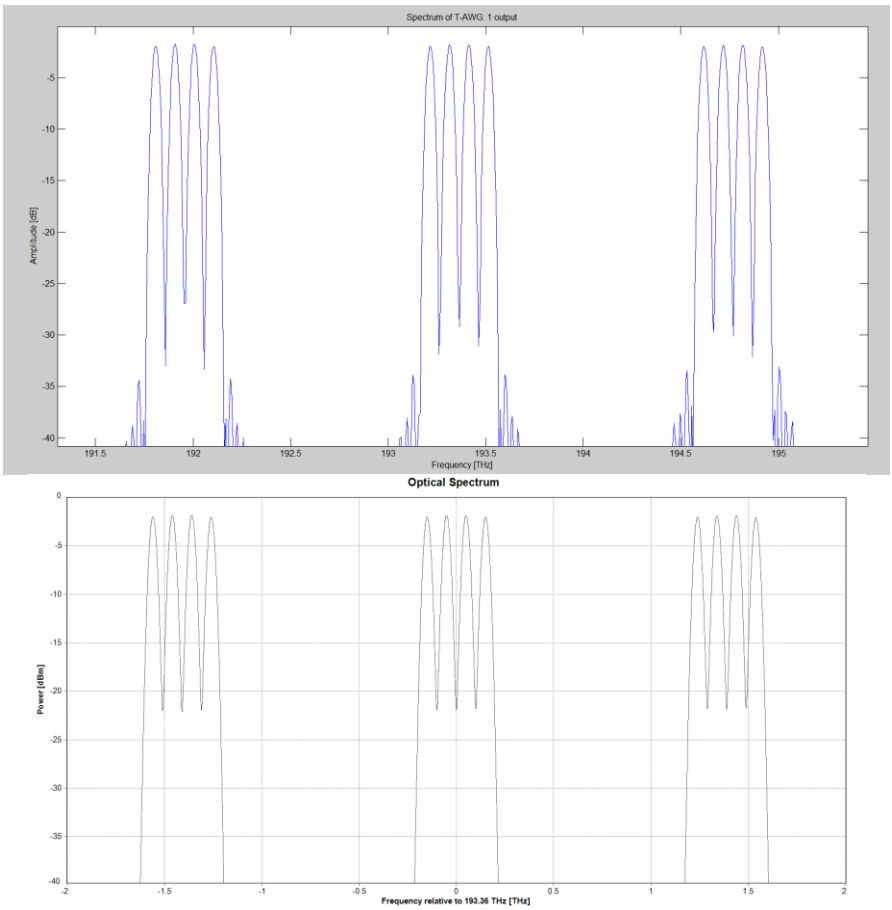

Figure 50 T-AWG spectrum. Four inputs, one output. Top: Transfer Function obtained in ASPIC® Bottom: Simulated in VPIphotonics®

In the case of four outputs and one input, one can conclude that the simulated shapes of the channels are similar to the ones obtained in the design process. The main difference lies on the noise which is present in the designed case. The noise is not present in the simulated AWG due to the limitations of the fitting process. On the other case (four inputs and one output) the noise that has the same behavior. One can also conclude that the minimums in each channel are not the same in terms of magnitude; this is also due to the numerical approximations. These facts do not affect the overall performance of the AWG once the main shape of the transfer function is preserved.

The same analysis can be done in the case of the R-AWG and the results are presented in Figure 51 and Figure 52.

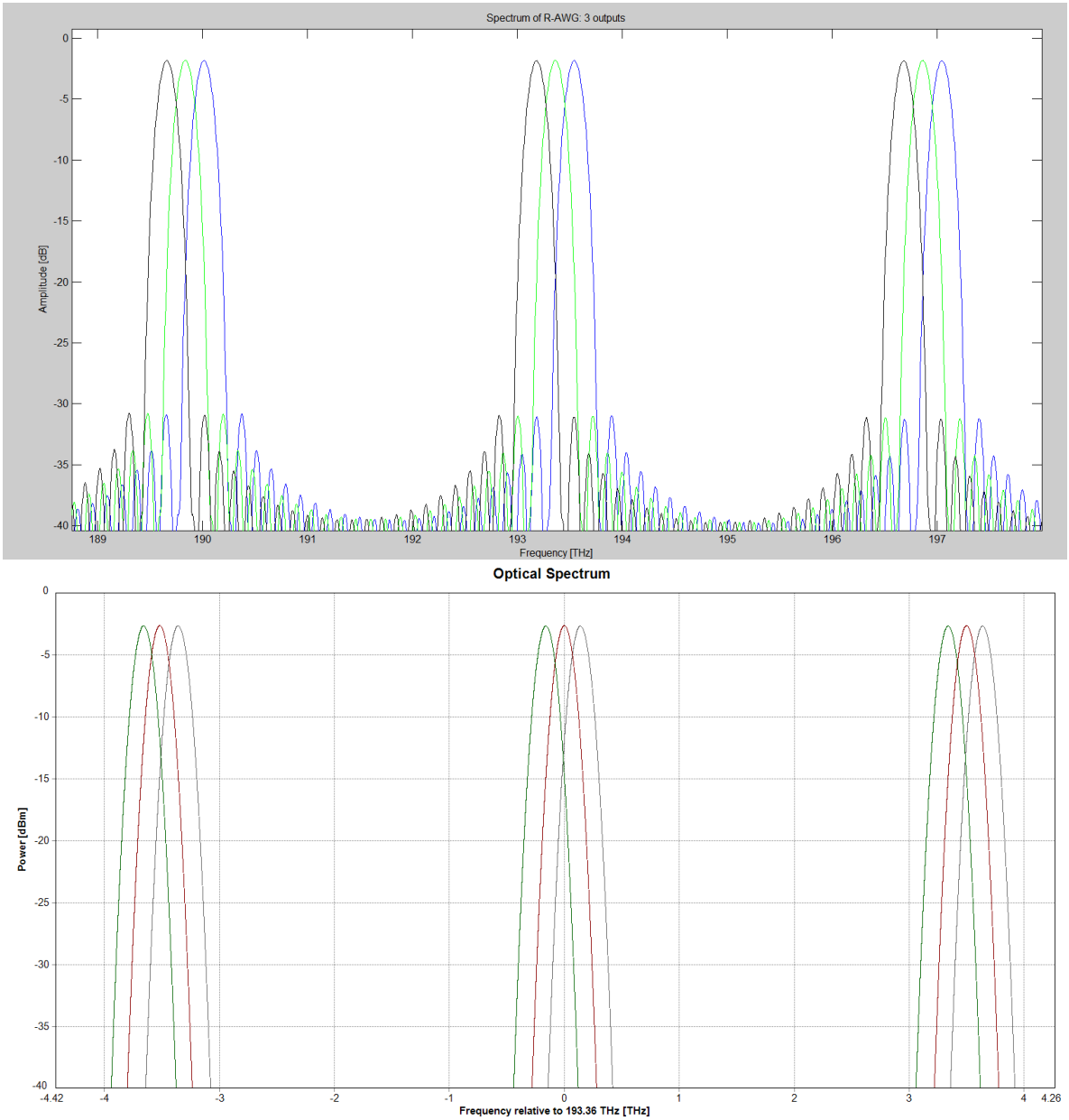

Figure 51 R-AWG spectrum. One input, three outputs. Top: Transfer Function obtained in ASPIC® Bottom: Simulated in VPIphotonics®

-

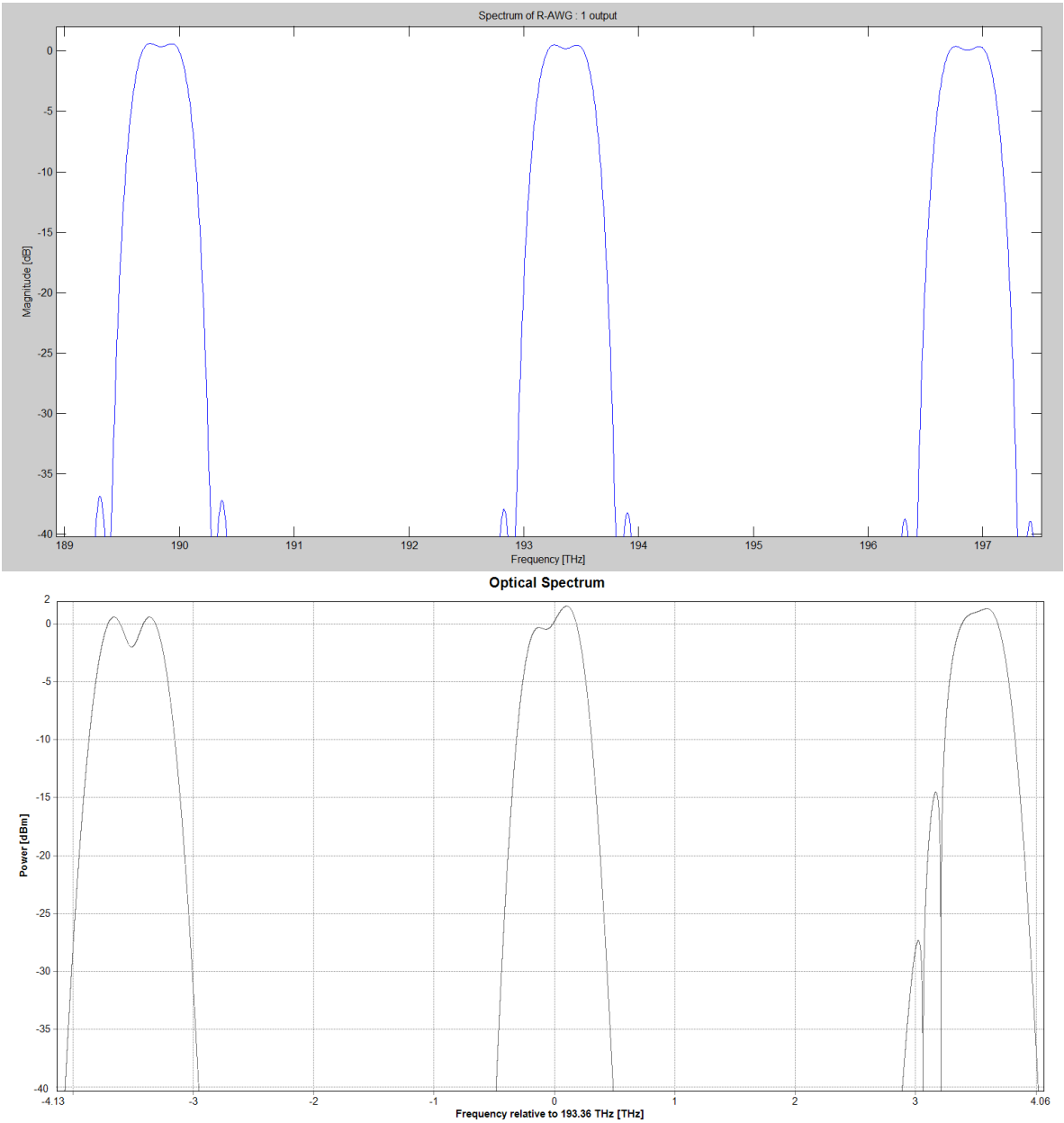

Figure 52 R-AWG spectrum. Three inputs, one output. Top: Transfer Function obtained in ASPIC® Bottom: Simulated in VPIphotonics®

In the case of the R-AWG the reasoning presented to the deviations of the simulated case in relation to the designed one is the same. In this case, it is important to highlight the case of Figure 52 where the differences are more perceptible. These differences are also due to the errors in the fitting. In this case the original transfer function is the result of the overlap of Gaussian transfer functions. This fact turns it more challenging to fit. Whereas, these impairments do not affect the main target which was to obtain an AWG that is passband in the central channel and reject the copies of the T-AWG. If one compare the simulated spectra presented in Figure 49 and Figure 52 one can conclude that this goal is achieved.

In brief, models to simulate T and R-AWG were created. The first approach was to use the embedded block of VPIphotonics® but as this software does not provide directly a bidirectional block the method of cosimulation was used. In this method, four unidirectional models were created and simulated. These models were then combined into two bidirectional models which are presented in Figure 53. On the left is the T-AWG and on the right is the R-AWG. The inputs presented on the left sides are multiport inputs and the output on the right side is a single port output, thus on the top of each device is the Nx1 configuration of each AWG. On the bottom part of the device is the 1XN configuration in which the input ports are on the right sides and the output ports are on the left sides.

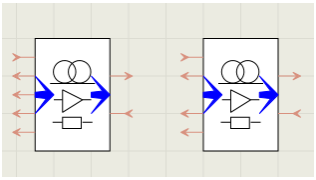

Figure 53 T and R-AWG bidirectional blocks

3.3 Mach-Zhender Modulator

MZM is an optical device that is used for external optical modulation. In the first deployments of optical communications direct modulation was used i.e. the light of the laser was turned on and off according to the data that was transmitted by varying the power of the laser. This type of modulation, although it is simple to implement has several drawbacks such as chirp, inefficient use of the spectrum and relatively low bit rates. A solution to this problems is the so called external modulation. In this technique, the laser has a constant power and the modulation is done through an external modulator such as MZM.

With the use of the external modulation is then possible to modulate light not only in intensity but also in phase, frequency and polarization. This allows the use of advanced modulation formats such as QPSK or 16-Quadrature Amplitude Modulation (QAM) which leads to a more efficient use of the spectrum and higher data rates.

3.3.1 Operating Principle and Description

It is possible to change the refractive index of a material and thus the refractive index of the waveguide. This is done by applying an external voltage via a coated electrode. One can then conclude that the optical carrier can be modulated in phase [29]. It can be proved that the phase modulation function can be assumed to be linear to the applied external voltage *u(t)*. [29]. The voltage that is necessary to apply, to obtain a phase shift of π, is denoted by V_π and thus one can write [29]

$$E_{out}(t) = E_{in}(t)e^{j\frac{u(t)}{V_\pi}\pi} \tag{3.13}$$

If one desires to obtain also intensity modulation, the principle of interference has to be applied. The structure employed for intensity modulation is the MZM whose structure is presented in Figure 54.

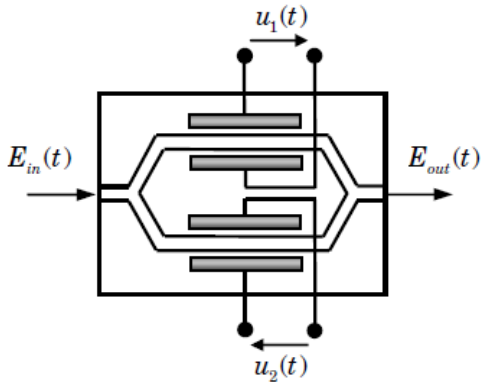

Figure 54 Optical Mach-Zehnder modulator [29]

It is presented a dual-drive MZM because both arms can be driven independently. The light inputs and through a Y-junction is split into two beams. Each of the beams go through the phase modulator of each arm and the phase shifts are defines as [29]:

$$\emptyset_i(t) = \frac{u_i(t)}{V_{\pi i}}\pi \, , i = 1,2 \tag{3.14}$$

where [30]

$$u_i(t) = V_{bias\ i} + V_{RF\ i}, i = 1,2 \tag{3.15}$$

The fields are then recombined at the Y-junction on the output. The interference can vary between constructive and destructive. The former case occurs if the relative phase shift is 0 and the latter if the relative phase shift is π. The relation between the input and output electric fields can be expressed by Equation (3.**16** assuming no insertion loss on the device and that at both Y-junctions the splitting ratio is 50/50 [31].

$$E_{out}(t) = \frac{1}{2}(e^{j\emptyset_1(t)} + e^{j\emptyset_2(t)})E_{in}(t) \tag{3.16}$$

MZM can present two modes of operation: push-push mode and push-pull mode. In the push-push mode only phase modulation is possible and occurs when $u_1(t)=u_2(t)=u(t)$ and $V_{\pi1}=V_{\pi2}=V_\pi$ .In the push-pull mode, intensity modulation is performed, e.g. if $u_1(t) = -u_2(t) = \frac{u(t)}{2}$ and $V_{\pi1}=V_{\pi2}=V_\pi$ the phase shift in each arm becomes symmetrical enabling destructive interference leading to intensity modulation. The expression of the output field can then be written as [31]

$$E_{out}(t) = \cos\left(\frac{u(t)}{2V_\pi}\pi\right)E_{in}(t) \tag{3.17}$$

by squaring this equation the relation between input and output power is obtained [31]

$$\frac{P_{out}(t)}{P_{in}(t)} = \frac{1}{2} + \frac{1}{2}\cos\left(\frac{u(t)}{V_\pi}\pi\right) \tag{3.18}$$

From inspection of the power relations one can conclude that the power transfer function of a dual drive MZM operating in push-pull mode is periodic with a period $2V_\pi$.

The dual drive MZM has two points of operation: quadrature and minimum transmission. The classification is dependent upon the bias voltage $V_{bias\ i,i=1,2}$ .The device is operating at the quadrature operating point, when the bias voltage equals half of V_π . The DC bias voltage has a value corresponding to half of the maximum power of the transfer function. The minimum transmission point of operation occurs when the power is the lowest possible. All this is summarized in Figure 55.

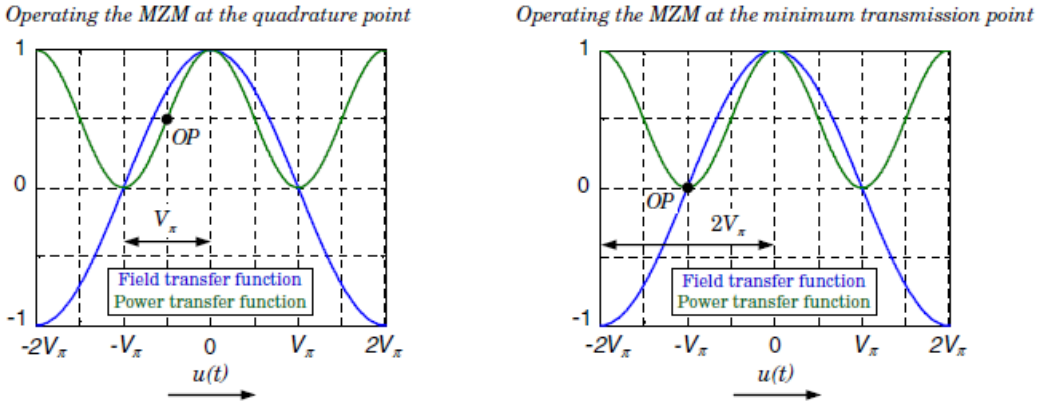

Figure 55 Points of operation of the MZM [29]

3.3.2 IQ Modulator

The MZM in the push-pull mode allows intensity modulation and binary phase modulation. In order to obtain advanced modulation formats the IQ modulator presented in Figure 56 shall be used.

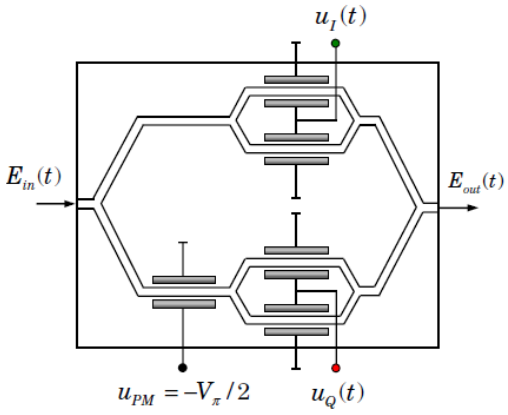

Figure 56 Optical IQ modulator [29]

The IQ modulator consists of two MZM modulators and a phase modulator. The incoming light is equally divided in two arms: the in-phase (I) and the quadrature (Q). A relative phase shift of π/2 is added in one of the arms. In each arm, intensity modulation is performed by operating the MZMs in the push-pull mode at the minimum transmission point. The principle of IQ modulation (Figure 57) is achieved and one can write [29]

$$\Delta\varphi_I(t) = \frac{u_I(t)}{V_\pi}\pi, \Delta\varphi_Q(t) = \frac{u_Q(t)}{V_\pi}\pi \tag{3.19}$$

Assuming that the device has no losses, the light is equally split into both arms and the driving voltage of the phase modulator is as expressed in Figure 56 ($u_{PM}=-V_\pi/2$) one can conclude [29]

$$\frac{E_{out(t)}}{E_{in}(t)} = \frac{1}{2}\cos\left(\frac{\Delta\varphi_I(t)}{2}\right) + j\frac{1}{2}\cos\left(\frac{\Delta\varphi_Q(t)}{2}\right) \quad (3.20)$$

Using the knowledge of Equation (3.**19)** and Equation (3.**20)** the amplitude modulation $a_{IQM}(t)$ and the phase modulation $\varphi_{IQM}(t)$ can be obtained using [29]

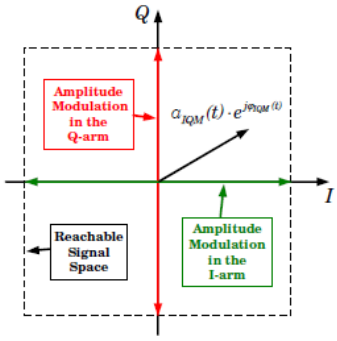

Figure 57 Principle of IQ modulation [29]

$$a_{IQM}(t) = \left|\frac{E_{out}(t)}{E_{in}(t)}\right| = \frac{1}{2}\sqrt{cos^2\left(\frac{u_I(t)}{2V_\pi}\pi\right) + cos^2\left(\frac{u_Q(t)}{2V_\pi}\pi\right)} \quad (3.21)$$

and

$$\varphi_{IQM}(t) = arg\left[\cos\left(\frac{u_I(t)}{2V_\pi}\pi\right), \cos\left(\frac{u_Q(t)}{2V_\pi}\pi\right)\right] \quad (3.22)$$

3.3.3 Mach-Zhender Modulator Modeling and Modulation Examples

This subsection has the purpose to present a model for the MZM available in SMART photonics foundry. With the presented model, a modulation example will be given. OOK-NRZ was chosen because is the one in use in access networks and is the simplest case of intensity modulation. It is a modulation format in which the output signal has two levels corresponding to the logical levels '0' and '1'. During the bit period, only one of these levels is used.

3.3.3.1 Mach-Zhender modulator modeling

In order to obtain a model of the MZM the software VPIphotonics® was used. The model in this software, is based on $LiNbO_3$ (lithium niobate) technology [28] which is not the technology used by the chosen foundry (InP – indium phosphide). However, the embedded block of VPIphotonics® was the only model used because there was not enough information, available from the foundry, (e.g. S21 parameters) to create a model with cosimulation. The parameter that was given most importance was V_π. It was used to simulate the driving of the device. In the design manual [23], is stated that there is a change of 12-15°/V.mm. Choosing a length of 2mm and assuming 13.5°/V.mm it yields to a V_π=6.75V.

With the intention of obtaining OOK-NRZ modulation the setup presented in Figure 58 was used.

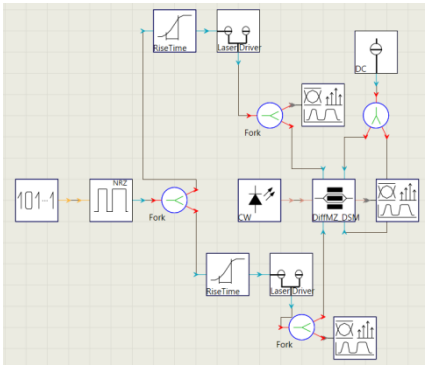

Figure 58 Setup to modulate the light with OOK-NRZ

The central block is the DiffMZ_DSM which is the VPIphotonics® embedded block for the MZM. At its left there is a continuous wave source which inputs in the MZM the light to be modulated. The left top and bottom DC inputs represent the DC level of the RF input signal which was set to 0 to operate at the minimum transmission point. The remaining blocks have the purpose to generate and show the RF signal to drive the MZM. The data is randomly generated at the left most block and it goes to an NRZ coder, the signal is then split into two branches which of them have a RiseTime block and a LaserDrive. The RiseTime block has the purpose to transform rectangular input pulses into smoother output pulses in order to band-limit the modulated optical signal. The LaserDrive sets the voltage level of the signal. This is the block that differentiates the two branches while in the upper branch the driving amplitude is set to $\frac{V_\pi}{2}$ in the lower branch it is set to $-\frac{V_\pi}{2}$ in order to obtain the conditions for the push-pull mode of operation. The plots of the driving signals as well as the modulated light are presented in Figure 59.In it, u2 represent the driving signal of the lower arm, u1 the driving signal of the upper arm and the modulated signal is the output of the MZM. One can conclude that the desired result is obtained and the modulated signal, in the time domain resembles u1.

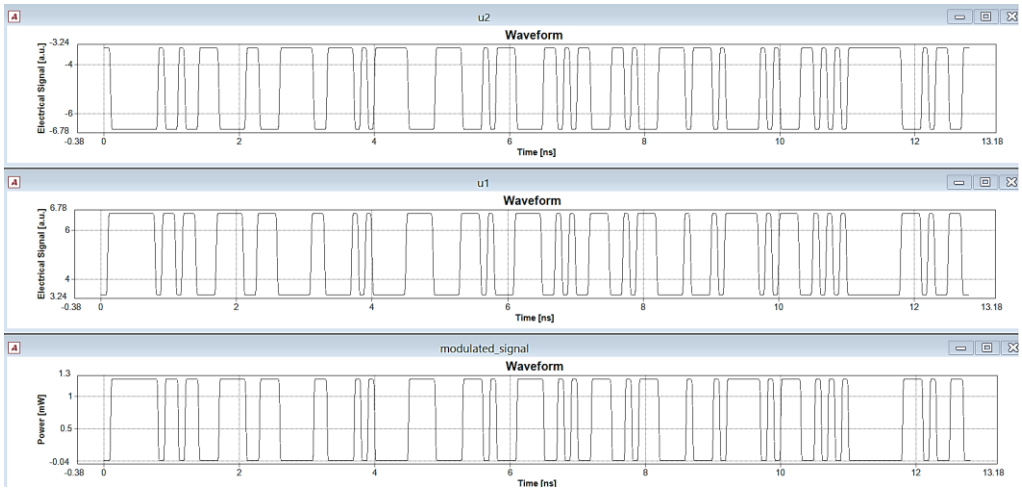

Figure 59 Wave shapes of driving signals and modulated OOK-NRZ signal

3.4 Multi-Mode Interference Devices

MMI devices are integrated optic components that use the self-imaging principle in order to obtain multiple images of the input field profile at certain positions along the device. During the last two decades, developments have been accomplished in the design and integration of MMI devices which combined to their multi-applications scenario made these devices very common in PICs [32]. A MMI device is composed by a multimode waveguide where the interference phenomena occur and at the extremes has N input and M output access waveguide which have a defined width and position and are tapered to single mode waveguides. MMI devices have many advantages such as robustness, reliability and ease of fabrication. As examples of application of MMI devices can be pointed out: optical gates, ring lasers and switches [33]. In Figure 60 one can find an example of MMI device (2x2 coupler) with its access waveguides.

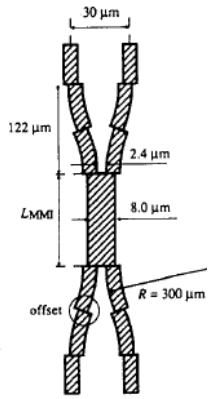

Figure 60 MMI device example (2x2 coupler) [34]

In order to understand the operation of MMI devices, the self-imaging principle has to be understood. This principle was first studied more than 150 years ago and it stated by Lucas B. Soldano and Erik C.M. Pennings as: "Self-imaging is a property of multimode waveguides by which an input field profile is reproduced in single or multiple images at periodic intervals along the propagation direction of the guide" [34].

3.4.1 Operating Principle and Description

With the purpose of understanding MMI devices the deduction of the propagation constants of the different modes should be done. The phenomenon of light interference occurs in multimode waveguides. A step-index multimode waveguide of width W_M with ridge and cladding refractive index n_r and n_c respectively at a free-space wavelength λ_0 supports *m* lateral modes

with mode numbers v=0,1,...,(m-1). The propagation constant of each mode can be deduced to be [34]

$$\beta_{\mathrm{v}} = k_0 n_r - \frac{(v+1)^2 \pi \lambda_0}{4 n_r W_e^2} \qquad (3.23)$$

where $k_0 = \frac{2\pi}{\lambda_0}$ and $\mathrm{W_e}$ is the fundamental width of the waveguide which takes in consideration lateral penetration depth of each mode fields. It is observed that the effective widths of all modes can be approximated by the effective width of the fundamental mode [34]. In most of the literature $\mathrm{L_\pi}$ is defined as the beat length of the two lowest-order modes and is expressed by [34]

$$L_\pi = \frac{\pi}{\beta_0 - \beta_1} \approx \frac{4 n_r W_e^2}{3\lambda_0} \qquad (3.24)$$

Leading to the definition of the propagation constant spacing [34]

$$(\beta_{0-}\beta_v) \cong \frac{v(v+2)\pi}{3L_\pi} \qquad (3.25)$$

Using the guided-mode propagation analysis (MPA) [35] one can define the field profile along the waveguide in order to understand where to find the desired images. At a position z the field can be written as [34]

$$\Psi(y,z) = \sum_{v=0}^{m-1} c_v \psi_v(y) e^{j(\beta_0 - \beta_v)z} \qquad (3.26)$$

where c_v are the field excitation coefficients and $\psi_v$modal field distribution of mode v. At a distance z=L, L being length of the device, and by substituting Equation (3.**25** into Equation (3.**26** yields to [34]

$$\Psi(y,L) = \sum_{v=0}^{m-1} c_v \psi_v(y) e^{j\frac{v(v+2)\pi}{3L_\pi}L} \qquad (3.27)$$

According to the modal excitation, interference can be classified as general and restricted. The former refers to self-imaging mechanisms that do not depend on modal excitation the latter is the opposite i.e. refers to self-imaging mechanisms that are obtained by exciting certain modes alone [34].

The exponential term in Equation (3.**27** is called the mode phase factor and in order to obtain a single image, this factor has to be equal either to 1 or $(-1)^v$. The first condition represents a direct replica of the input field. In the second condition, even modes will be in phase and the odd modes in antiphase. Overall, general interference leads to the conclusion that single images of the input field will appear at a distance even and odd multiple of $3\mathrm{L_\pi}$.

Regarding multi-fold images, they are formed at intermediate positions. With the proper mathematical analysis, one can conclude that N images are obtained at the distances [34]

$$L = \frac{p}{N}(3L_\pi) \tag{3.28}$$

$$with\ p \geq 0\ and\ N \geq 1\ which\ are\ integers\ with\ no\ common\ divisor$$

and the field will have the form [34]

$$\Psi(y, L) = \frac{1}{C}\sum_{q=0}^{N-1} \Psi_{in}(y - y_q)e^{j\varphi_q} \tag{3.29}$$

with [34]

$$y_q = p(2q - N)\frac{W_e}{N} \tag{3.30}$$

$$\varphi_q = p(N - q)\frac{q\pi}{N} \tag{3.31}$$

C is such that |C|=$\sqrt{N}$, p refers to imaging periodicity along z and q refers to each of the N images along *y*. These last two equations are helpful tools in the design of the device in order to obtain the position as well as the phase at the outputs. With these facts one can conclude that multi self-imaging mechanisms allow the realization of NxN or NxM couplers. The amplitude of the N output fields is $1/\sqrt{N}$ and the phases are given by [34]

$$\varphi_{rs} = \frac{\pi}{4N}(s - 1)(2N + r - s) + \pi\ , r + s\ even \tag{3.32}$$

$$\varphi_{rs} = \frac{\pi}{4N}(r + s - 1)(2N - r - s + 1), r + s\ odd \tag{3.33}$$

Concerning the restricted interference, Soldano and Pennings [34] divide it into two cases: paired and symmetric interference. Each of them is defined by the excitation requirements. In the case of paired interference each even mode leads its odd partner by a phase difference of π/2 at z=L_π/2 (the 3dB length). In the symmetric interference the image is obtained by linear combination of the even symmetric modes. The summary of the characteristics of the general and restricted interference is presented in Table 5.

Interference mechanism	**General**	**Paired**	**Symmetric**
Input x Outputs	N x N	2 x N	1 x N
First single image distance	$(3L_\pi)$	(L_π)	$(3L_\pi)/4$
First N-fold image distance	$(3L_\pi)/N$	$(L_\pi)/N$	$(3L_\pi)/(4N)$
Excitation requirements	none	$c_v=0$ *For v=2,5,8,…*	$c_v=0$ *For v=1,3,5,…*
Input(s) location(s)	any	$y = \frac{\pm W_e}{6}$	y=0

Table 5 Summary of characteristics of the general, paired and symmetric interference mechanisms

3.4.2 Multimode Interference Devices Application Examples

MMI devices have been, in the last years, used in a big variety of applications. Most of these applications regard photonic signal processing such as optical gates, optical couplers, optical switches and ring lasers [32]. It can also be stated that for future optical networks, optical routers will be needed because they can provide high throughputs and low power consumption. Important developments have been made in this field, optical logic gates have been developed and reported such as in [36].

In this section, two applications of MMI devices will be presented: switching and optical logic gates. In the latter case, a special focus is given and a specific example is presented.

3.4.2.1 Switching applications

Switching functions can be achieved with MMI devices by utilizing nonlinear effects in its regions. In Figure 61 it is presented a 1x2 switch based on active MMI regions. As the three regions are composed from active materials, one can conclude that each of these regions can be enabled to act as a gain or loss region in order to achieve switching.

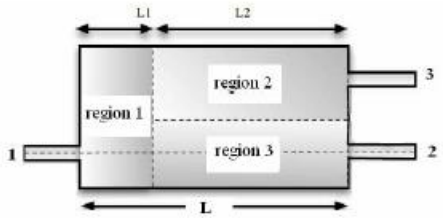

Figure 61 Active MMI regions based switch [32]

3.4.2.2 Optical logic gates

As in the optical switching application, optical logic gates can be obtained with the aid of nonlinear effects of the material and their operation is similar. Nevertheless the use of the nonlinear material effects has several drawbacks such as low transmission capability, requirement of high optical intensity and limited speed of signal processing [32].

In Figure 62 an optical logic gate based on MMI device is presented. The device consists of three inputs, three outputs and a MMI region. All the inputs and outputs waveguides are single-mode ridge waveguides based on Si which has the plasma dispersion effect [37]

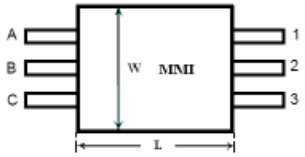

Figure 62 Optical logic gate scheme [32]

The device can function as an OR, NOT, NAND and NOR gate simply by switching the optical signal to different input waveguide ports. The major drawback in this implementation is that all the signals must have the same phase, wavelength and polarization which in practice is very difficult to realize.

On- chip logical gates are, nowadays, an emerging field of research. In [36] it is presented a MMI device that implements XOR and AND logic gates without the use of nonlinear optics. The device uses photonic-crystal waveguides as they can adjust the propagation by modifying rod diameters. The optimization of the modification of rod diameters was done through a genetic algorithm and the device proved to present acceptable ON and OFF logic-level contrast ratio in the whole C-band. The logic levels at input are set by the phase (φ) of the input signals. In the XOR case the logic information is summarized in Table 6 and the field distributions in all cases is presented in Figure 63.

Input ports				**Output port**
A		**B**		**X**
logic	φ	**logic**	φ	**logic**
0	π	0	π/2	0
0	π	1	- π/2	1
1	0	0	π/2	1
1	0	1	- π/2	0

Table 6 Functions of XOR logic gate [36]

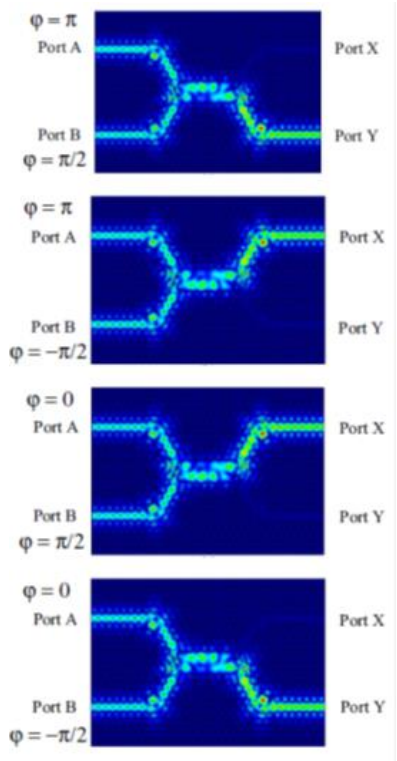

Figure 63 Field distributions of XOR logic gate. [36]

3.5 Optical Directional Coupler

Optical directional coupler is a passive component that is constituted of an array of waveguides placed together. The working principle of a directional coupler is to transfer energy between adjacent waveguide cores. This device is nowadays commonly used in PICs, as it is a component easy to fabricate and to integrate. Among its functions one can point as examples: light branching, filtering, splitting and wavelength independent splitting [38].

In Figure 64 it is presented an example of a double input double output device with its geometric parameters. One can conclude that the device is constituted of three main parts: two transition portions (edges) and one coupling portion (center). The transition portions make the connection to and from the coupling portion where the light transfer occurs. The separation between the waveguides at the end of the transition section has to be such that no coupling occurs.

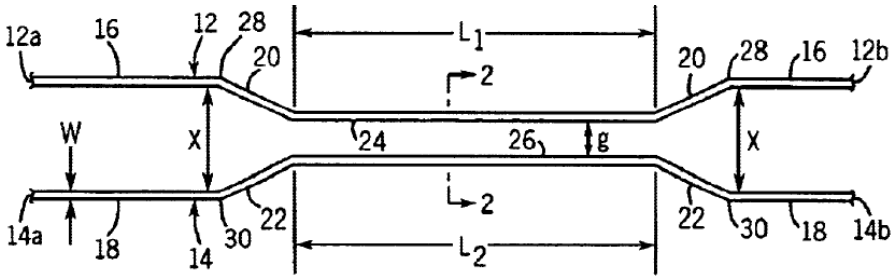

Figure 64 Double input, double output directional coupler [39]

3.5.1 Operating Principle and Description

In order to understand the optical directional couplers one must understand the coupled mode theory. It presents the general theory of coupling in an N array waveguide. In the scope of this thesis, a general introduction on coupled mode theory is given and then a special focus on 2x2 (two inputs, two outputs) directional couplers is made.

3.5.1.1 General Introduction on Coupled Mode Theory

The coupled mode theory starts to assume that the eigenmodes of the coupled waveguide array can be represented by the guided modes of the individual array. A coupled waveguide array composed of N coupled waveguides, supports N guided modes whose amplitude can be represented by the amplitudes of the guided mode of the individual waveguides. It means that when optical power is launched into one waveguide of the array it is interchanged between the guided modes of all the waveguides that form the array [40]. In other words, one can see optical interaction as the beating between the symmetric and anti-symmetric supermodes of the array.

The exchange of power occurs due to the evanescent tail of the guided mode of the waveguide where the power is launched and due to the natural modes of the remaining waveguides of the array. [38]

3.5.1.2 2x2 Waveguide Directional Coupler

The geometry of the 2x2 directional coupler was generally presented in Figure 64. The region where the coupling occurs consists of two single-mode waveguides that are closely placed in parallel.

It is possible to demonstrate that the array of the two waveguides supports two modes (called the supermodes): a symmetric and an anti-symmetric mode. When light is launched into one of the waveguides it excites a linear combination of the supermodes. As symmetric and anti-symmetric modes have different propagation constants, one can depict that along the distance of propagation the system develops a phase difference between them. The phase difference between the supermodes can lead to occurrence of cancellation in one waveguide and addition on the other at certain positions. This leads to a power transfer from one waveguide to another. This phase difference between the modes is periodic, thus a periodic exchange of power between the waveguides takes place along the propagation length. Power transfer can only be total if the two waveguides are equal [41].

In the case of symmetric coupler formed by two identical waveguides it can be shown that the transfer matrix of the device is given by:

For the amplitude [41]

$$\begin{bmatrix} A_1(L) \\ A_2(L) \end{bmatrix} = \begin{bmatrix} \cos(kL) & isin(kL) \\ isin(kL) & \cos(kL) \end{bmatrix} \begin{bmatrix} A_1(0) \\ A_2(0) \end{bmatrix} \quad (3.34)$$

For the electric field [28]

$$\begin{bmatrix} E_1(L) \\ E_2(L) \end{bmatrix} = \begin{bmatrix} \sqrt{1-\alpha} & i\sqrt{\alpha} \\ i\sqrt{\alpha} & \sqrt{1-\alpha} \end{bmatrix} \begin{bmatrix} E_1(0) \\ E_2(0) \end{bmatrix} \quad (3.35)$$

where k is the coupling coefficient that measures the strength of coupling and is given by [38]

$$k = \frac{\beta_s - \beta_a}{2} \quad (3.36)$$

with β_s, β_a the propagation constants of the respectively symmetric and anti-symmetric modes of the individual waveguides; α is the couple factor that varies from 0 to 1 and specifies the amount of power that is transferred from one waveguide to the other.

In the case of only the first input is excited, one can conclude that [41]

$$P_1(L) = A^2 cos^2(kL) \tag{3.37}$$

$$P_2(L) = A^2 sin^2(kL) \tag{3.38}$$

By inspection of Equation (3.**37**and Equation (3.**38** it is easy to determine that it is relatively easy to control the amount of power that is transferred from one waveguide to the other. For example, in the case of $L = \frac{\pi}{4k}$ an equal power distribution is achieved obtaining a 3 dB coupler.

3.5.2 Directional Coupler Design and Results

In this subsection it is presented the design of a 3dB directional coupler. The 3dB couplers have several applications in PICs such as power splitters or as part of integrated coherent receivers.

In order to design the directional coupler, the software OptoDesigner® was used. OptoDesigner® is a software from Phoenix Software® that allows the simulation of light propagation through integrated optic devices. In the process of designing a PIC, this software is used for placing the components together, simulate some of them and generate the mask for the foundry. OptoDesigner allows one to use several methods of simulation. In order to simulate the directional coupler Beam Propagation Method (BPM) is used by OptoDesigner® to simulate the device. This method uses a start field and computes the light propagation using discretized Maxwell equations [40]. In OptoDesigner®, the simulations are done through component description in the programming language C++. The main reason to the choice of this software is that it has embedded libraries of the SMART Photonics foundry. These libraries have already pre-programmed building blocks such bending sections, waveguides, SOAs and MMI where the users can change the parameters that best fit their situation.

As stated before, the target in this subsection is to obtain a 3dB directional coupler. The chosen central wavelength of operation of this device is 1550 nm. This choice was done for two main reasons, the first one regards software limitations. The BPM method in OptoDesigner® can only be used in the range from 1500 nm to 1600 nm. The second reason is that most of the technology of SMART Photonics is optimized for 1550nm (e.g. SOAs have maximum gain at this wavelength).

The design of the component was done through iterative simulations that had the goal to optimize its performance i.e. have as close as possible to half of the input power at each output. In Figure 65 one can find the final layout of the device. The pink arrow denotes the flow of the simulated light. The inputs are at the left side and the outputs at the right side. In order to analyze the dimensions of the device, one can use the rulers presented in the referred figure. A design based on an iterative process was chosen instead of a design based on the solution of the

equations presented on the previous section due to the complexity of solving the equations, specially obtaining the coupling coefficient.

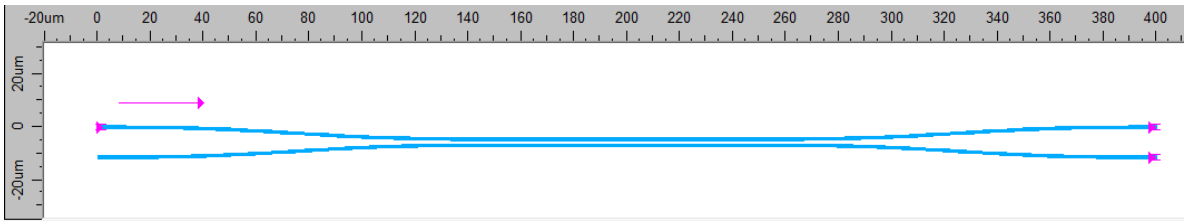

Figure 65 Final layout of the designed 3dB directional coupler

Before the iterative process design of the coupling region the transition region was designed. At the input and output of the device, there must be no coupling. In the chosen technology of the SMART Photonics foundry the defined distance to avoid coupling is 10µm [23], thus the core of both waveguides must be placed at this distance. To bring the waveguides close to each other to the interaction region, an S-bend was used. An S-bend is a simple waveguide with a curvature angle. In the chosen foundry there is a limitation to the fabrication of the curvature angle, this limitation established the length of the S-bend. Maximum curvature was used to reduce the footprint of the device as much as possible.

In the design process there were several degrees of freedom: waveguide width, coupler length (i.e. interaction region length) and distance between waveguides in the interaction region onwards called coupler distance. The first step on the design was to choose the waveguide width. After this choice some coupler lengths were tested. For each pair of waveguide width and coupler length the enhanced coupler distance was obtained through an iterative process that will be presented shortly.

The choice of the waveguide width was almost arbitrary with the only condition that the waveguide should be single mode. The chosen waveguide width was 1µm, this is a single mode width and as it is presented next it allows low loss coupling. The next step was to obtain the coupler length, the criteria in this case is that it should be chosen sufficiently large to observe at least a complete coupling of energy from one waveguide to the other [42]. For the same coupler distance, several coupler lengths were set. It was observed that the referred criterion was met for a length of 100 µm.

Concerning the coupler distance, as the other two degrees of freedom were already fixed, a sweep was done to this variable in order to obtain the desired result: half of the input power at each output. In order to launch power in one of the inputs the software provides a *ModeLauncher.* The user defines the position to put it as well as the beam characteristics (power and phase).In the simulations it was chosen the upper input and the *ModeLauncher* is the pink triangle present at the input side of Figure 65. For the outputs, the software provides a Mode*Overlap*. The user can choose where to place them. In Figure 65 *ModeOverlaps* are the pink triangles at the end of the output waveguides. At each iteration, the software outputs the

numerical value of the *ModeOverlaps* (power intensity). The algorithm consists of a loop in which the stop condition is related to the amplitude of the field at the opposite output where the beam is propagated. A beam with a unitary input is launched in the top input and the measurement is done at the bottom output. The starting point of the distance between the waveguides is 0.4 μm as this is the minimum separation that the foundry process can achieve [23]. At each iteration the value of the *ModeOverlap* of the bottom output was measured and compared to 0.5, if this condition was not met the coupler distance was increased by 0.001μm.

The resulting coupler with the presented design process was already shown in Figure 65. With the BPM simulation one can visualize how the light propagates through the device. The result is presented in Figure 66 .The value of the top and bottom *ModeOverlap* is 0.5, hence one can conclude that, according to the simulation, the device does not present any loss. Regarding the phase of the overlaps it is important to state that there is a 90° degrees phase shift between the phases of the *ModeOverlaps* as it was expected from the analysis of the equations presented in the previous subsection. This feature is very important in the architecture of a coherent receiver.

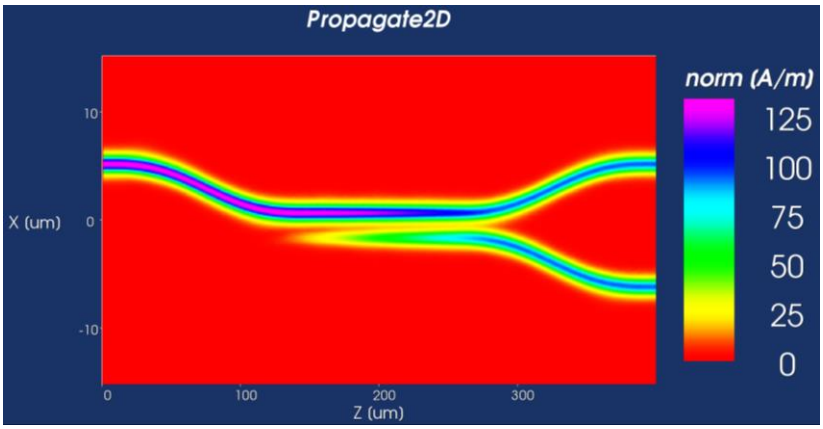

Figure 66 Propagation of the light through the 3dB coupler

The bandwidth of operation of the 3dB coupler is narrow as all its design (length and gap between waveguides) is wavelength dependent. In subsection 3.2.3 AWG Design and Modeling, it was stated that the choice of the four wavelengths was related to the 3dB directional coupler. This was done so that the operations of the devices match. The choice of the wavelengths was based in two criteria: unbalance and phase difference between the output waveguides. By unbalance one can understand the difference of the amplitudes of the *ModeOverlap* i.e. a measure of the deviation from a splitting ratio of 50/50 between the outputs. The designed device was simulated over a wavelength grid with 0.8nm of spacing. The results are presented in a form of a plot in Figure 67. One can conclude that the phase difference is a multiple of 90° in the entire simulated band, thus the criterion that allows the choice of the channels was based on the unbalance. The channels: 1549.2, 1550, 1550.8 and 1551.6 are the ones that present an unbalance smaller than 0.5% thus those were the chosen ones.

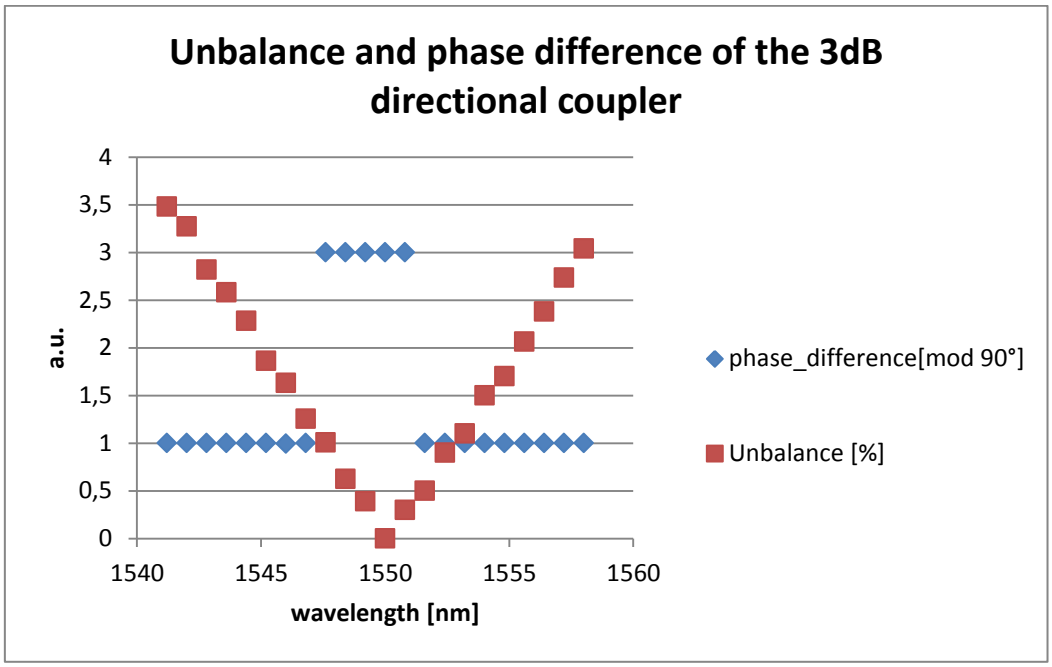

Figure 67 Unbalance and phase difference of the 3dB directional coupler

3.6 Photodetectors

A photodetector is a device that transforms the optical input into an output electrical signal. It is used in the reception block of a transceiver. The characteristics of a photodetector are similar to the ones of a light source i.e. it should have fast response, high sensitivity, low cost and small size.

In this section, the reader can find the theoretical background of photodetectors in terms of their main performance features. After that overview, two different types of photodetectors are presented: *p-i-n* photodiode (PIN) and avalanche photodiode (APD). In the end an architecture to improve the operation of PIN is presented: PIN photodetector with preamplification.

3.6.1 Introductory Concepts

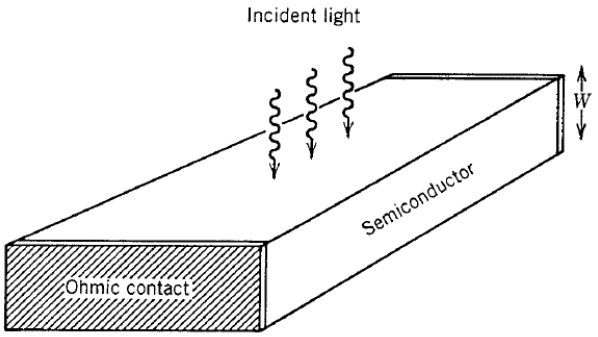

Figure 68 Model of semiconductor photodetector [43]

A simple model of a photodetector is presented in Figure 68. It is constituted by a semiconductor slab and the light inputs at the top and is partially absorbed along its width W. If the energy of the photon is higher than the band gap energy of the semiconductor, an electron-hole pair is generated. A photocurrent I_P is then created and one can write [41]

$$I_P = R_D P_{IN} \tag{3.39}$$

where P_{IN} is the input power and R_D is the responsivity of the device. Responsivity is a photodetector feature that represents the photocurrent generated per unit of incident optical power. Responsivity can be expressed as [41]

$$R_D = \frac{q\eta}{hf} \tag{3.40}$$

with q the electron charge, h the Planck's constant, f the photon frequency and η the quantum efficiency. Quantum efficiency is the probability that an incident photon will produce an electron-hole pair. It is given by the ratio of the output electron flux to the input photon flux.

The responsivity of a photodetector is directly related to its design and it is wavelength dependent thus different materials suit different applications and wavelengths. In Figure 69 one can observe the dependence of the responsivity with wavelength for Silicon-Si, Germanium-Ge and Indium Gallium Arsenide-InGaAs. One can conclude that the responsivity increases with the increase of wavelength. This is due to the fact that there are more photons present for the same optical power, however one can also notice that this increase has a cut-off wavelength. This cut-off wavelength represents the point where the photons do not have enough energy to overcome the gap of the material i.e. the energy of the photons is smaller than the energy gap of the material.

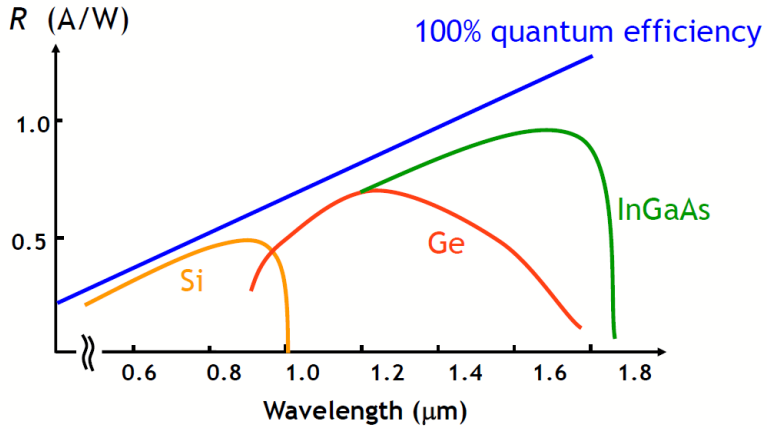

Figure 69 Wavelength dependence of responsivity [44]

Another physical characteristic of the material is the absorption coefficient α. Assuming that there is an antireflection coating in the model presented in Figure 68 the power transmitted can be expressed as [41]

$$P_{tr} = e^{-\alpha W} P_{in} \tag{3.41}$$

as the absorbed power is the difference between the input and transmitted power, one can revisit the concept of quantum efficiency and define it as [41]

$$\eta = \frac{P_{abs}}{P_{in}} = 1 - e^{-\alpha W} \tag{3.42}$$

By inspection of Equation (3.**42)** it is possible to conclude that when the absorption factor is zero, the quantum efficiency is also zero and the quantum efficiency approaches 1 when $\alpha W \gg 1$. With this reasoning one can determine that the device should have the width as big as possible. That is not true. In photodetectors there is a tradeoff between bandwidth and responsivity. The bandwidth of the photodetector is given by the speed of the response of the device to the incident optical power. In order to quantify the bandwidth, two time constants must be analyzed. One is the time constant of the equivalent RC circuit (τ_{RC}) which defines the rise time of the

device. The rise time is the time that takes the current to go from 10 to 90% of its final value when an abrupt optical power is received. The other time constant is the transit time(τ_{tr}) that represents the elapsed time from the moment the photons are absorbed until the carriers are collected. This points to the conclusion that the smaller the width the bigger the bandwidth leading to the tradeoff presented before. With these two time constants, the bandwidth can be defined as [41]

$$\Delta f = \frac{1}{2\pi(\tau_{RC}+\tau_{tr})} \tag{3.43}$$

The last parameter that one should take into account as an introductory concept of photoreceptors is the dark current I_D. This current is generated in the photodetector in the absence of any optical signal. In a good photodetector it should be negligible (few nA), although in high-sensitivity receivers this parameter has to be considered.

3.6.1.1 p-n Photodiode

A reverse-biased p-n junction is based on a region called depletion region. In this region a built-in electric field opposes the flow of electrons from the n to the p side and holes from the p to n side. When light illuminates the depletion region an electron-hole pair is generated through absorption. Due to the built-in electric field electrons accelerate and drift to the n and p side respectively. The result flow current is proportional to the input optical power and thus a reversed bias p-n junction is also called p-n photodiode. This device and its operation principle are presented in Figure 70.

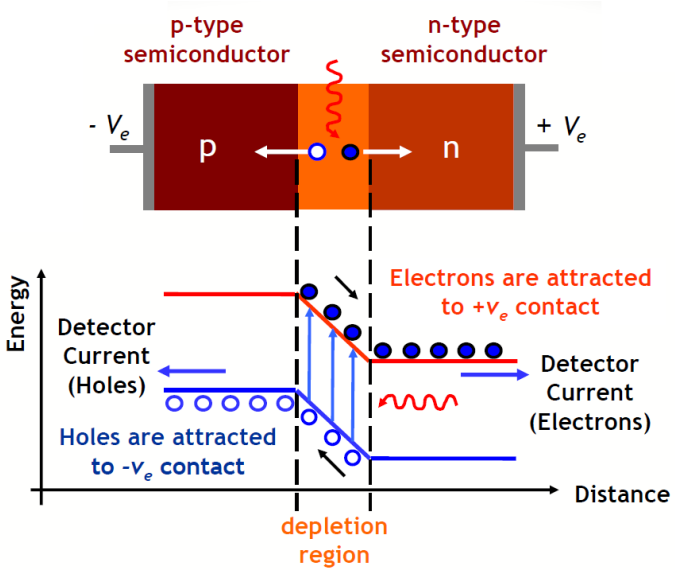

Figure 70 p-n photodiode and its operation principle [44]

The major drawback of the p-n photodiode is the diffusive component in the photocurrent. It is due to the absorption of incident light outside the depletion region. When this phenomenon happens, electrons generated in the p-region have to diffuse to the boundary of the depletion region before they can drift to the n-region. The same happens with the holes that are generated on the n-region. Diffusion is a slow process and thus it affects the bandwidth of the device and distorts the temporal response of a photodiode as can be seen in Figure 71.

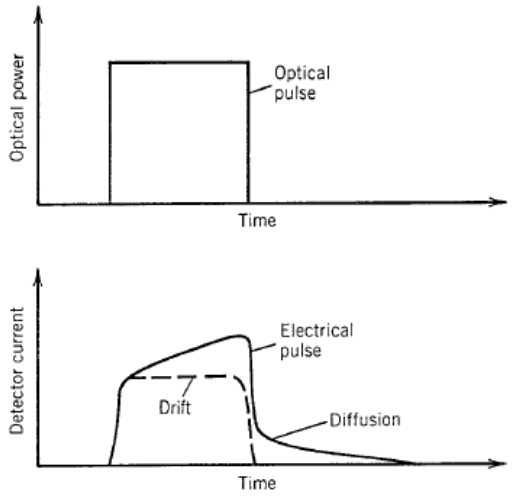

Figure 71 Drift and diffusion current effect on the response to an optical pulse in a p-n photodiode [43]

3.6.2 p-i-n Photodiode

As stated before, there is a tradeoff between quantum efficiency and bandwidth in the p-n photodiodes which is due to the diffusion of the carriers as it is a slow process. A solution to this problem is the PIN. In this device a layer of undoped semiconductor material is introduced between the p and n regions increasing the width of the depletion region as can be seen in Figure 72.

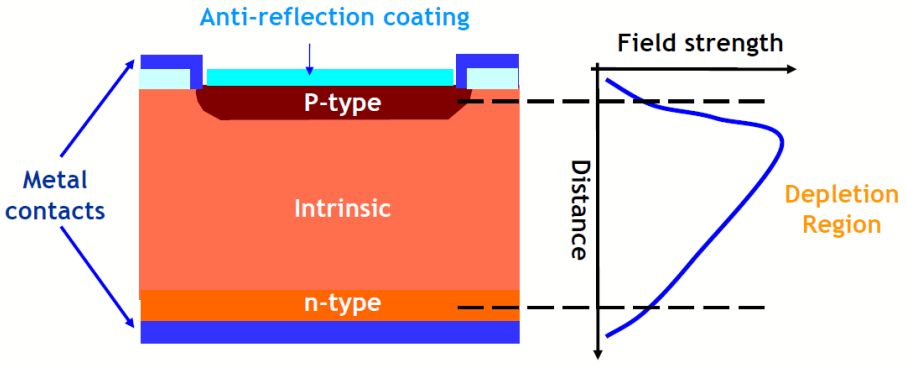

Figure 72 PIN scheme and field strength versus distance relation [44]

The major difference between a p-n photodiode and a PIN is that in the latter the drift current dominates over the diffusion due to the intrinsic layer. Most of the semiconductors do not absorb photons (i.e. they are transparent) in the range of the wavelengths used in fibre optic communications, e.g. InP only absorbs at $\lambda<0.92\mu m$ [45]. Hence a material that absorbs photons in the desired wavelength region should be used in the intrinsic region. The most common solution is the InGaAs that is not transparent in the range 1.0-1.65 μm. With the conjugation of InP in the p and n region and InGaAs in the i region one can conclude that this solution suits most of the optical communications applications. With the increase of the width of the depletion region one obtain then an increase in the absorption of incident light that leads to an increase in the quantum efficiency of the photodetector.

PIN not only produces signal current but also a noise current called shot noise. This shot noise is due to the fact that the photocurrent is not continuous but a collection of pulses that correspond to the electron-hole pairs created. If these pulses are approximated by Dirac pulses, the shot-noise spectrum is white and its mean square value is given by [45]

$$\overline{i_{n.PIN}^2} = 2qI_{PIN}.BW \qquad (3.44)$$

where q is the electron charge, I_{PIN} the current generated in the PIN and BW the bandwidth over which the shot noise was measured. By inspection of Equation (3.**44)** one can conclude that the shot noise current is signal dependent i.e. with an increase of the optical power the shot-noise also increases. However one can also conclude that root mean square value only increases with the square root of the signal amplitude, thus there is still a gain in signal to noise ratio.

3.6.3 Avalanche Photodiode

All photodetectors have a minimum current for a proper operation. This current depends on the input power and is described in Equation (3.**39)**. For a PIN the responsivity is limited by the quantum efficiency. This feature is improved in an APD as it is designed to provide an internal current gain. This device is similar to the PIN and is also reversed biased, the major difference is that it has an additional layer known as the multiplication layer where the internal current gain occurs. As in the PIN, the absorption layer is typically made of InGaAs and n,p and gain region are made of InP because it can support higher electric field which increases the performance of the photodetector. One can find in Figure 73 a scheme of an APD where the layers are depicted as well as the field strength along them.

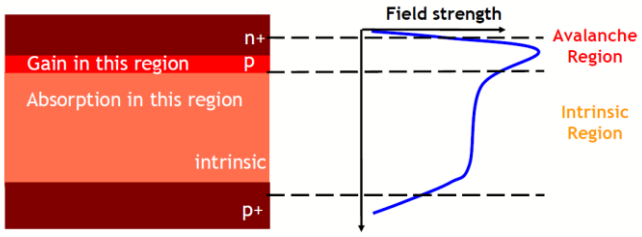

Figure 73APD scheme and field strength versus distance relation [35]

The physical phenomenon that describes the current gain is known as impact ionization. As the avalanche region provides an higher internal electric field, an accelerating electron can acquire sufficient energy to generate a new electron-hole pair i.e. an electron in the conduction band gives part of its kinetic energy to an electron in the valence band that ends up in the conduction band leaving a hole behind. This process works as in an avalanche: a single primary electron generated through the absorption of a single photon generates several electrons and holes that contribute to the photodiode current. The dimension of the impact ionization phenomenon depends on the material and has two coefficients α_e and α_h that are the impact ionization coefficient of electrons and holes respectively.

The gain of the device is designated by the avalanche gain or multiplication factor (M) and can be expressed as [41]

$$M = \frac{1 - k_a}{e^{[-(1-k_a)\alpha_e d]} - k_a} \tag{3.45}$$

where d is the thickness of the gain region and k_a is the ratio of the impact ionization of the holes to the impact ionization of the electrons. In the situation of $k_a = \alpha_e d = 1$ the APD gain becomes infinite. This condition is known as avalanche breakdown. The avalanche factor is sensitive to the reverse bias voltage which leads to the conclusion that this should be well controlled. Moreover, it is also temperature dependent thus control electronic is needed and a limitation to the use of this device in optical systems arises. Due to the gain region, the responsivity is also increased M times when compared to a PIN thus, the responsivity of an APD can be obtained by multiplying by M the right side of Equation (3.**40)**.

The gain region not only introduces gain but also noise, thus APD is a noisier device when compared to PIN. It is important to notice that the quantified avalanche gain is in reality the average gain of the device as the primary carrier is not always multiplied by the same factor i.e. some photons can generate 9 electron-hole pairs and some can generate 13 electron- hole pairs. The mean square noise of the noise current of the APD can be expressed as [45]

$$\overline{i_{n.APD}^2} = FM^2 2qI_{PIN}.BW \tag{3.46}$$

where F is excess noise factor, and I_{PIN} is the current generated by a PIN with the same responsivity and under the same input power of the APD under study. The excess noise factor also depends on the reverse voltage and can be expressed as [45]

$$F = k_A M + (1 - k_A)\left(2 - \frac{1}{M}\right) \quad (3.47)$$

Because the APD gain can only increase at the expense of an increase of the noise, one can conclude that it is possible to determine an optimum APD gain as a function of the material properties (k_A), amplifier noise and received power level.

The bandwidth of the device also decreases with the increase of the gain. The device can be analyzed as an amplifier and thus one can notice that the product of the gain bandwidth remains approximately constant and it is used to quantify the speed of an APD.

In conclusion, one can state that APD's major benefit is to provide gain. With this feature weaker signal can be detected in comparison with PIN. On the other hand, it requires higher bias voltage, is noisier, more sensitive to variations in temperature and bias voltage and is more expensive than a PIN.

3.6.4 PIN Photodetector with Optical Preamplifier

As was stated in the previous section, APD offers the possibility to detect weaker signals than with PIN although this is done at the cost of bandwidth reduction. APD are only in use for applications up to 2.5Gb/s because it is very challenging to fabricate these devices with a gain-bandwidth relation useful for applications with higher bitrate. The solution in these applications is a receiver architecture with an optical amplifier before the PIN, which allows higher sensitivity and speed at the cost of complexity and money.

The most common solution is to use an EDFA as the optical amplifier due to its high gain and low noise in the range of 1530-1560 nm. In the process the received signal starts to be combined with the light of an external pump power. This combined signal goes then through an Erbium doped fibre with a defined length where the amplification occurs due to the stimulated emission. An optical isolator needs to be used in order to prevent any reflected power to go to the amplifier which can cause instability. Before the PIN there should be also a filter that is used to reduce the noise power that is generated in the EDFA. The architecture is depicted in Figure 74.The gain of the amplifier is dependent of the length of the Erbium doped fibre and the power of the pump. With an EDFA one can obtain a gain (G) ten times higher than the one that is obtained with the APD. The current produced by the PIN photodiode can be expressed as [45]

$$I_{OA} = GRP \quad (3.48)$$

where R is the responsivity of the photodiode and P is the power before the amplifier.

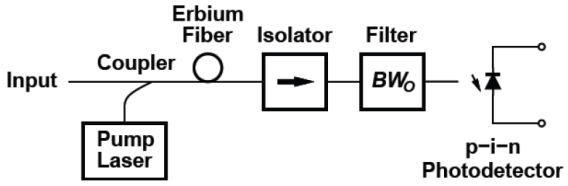

Figure 74 PIN with EDFA as optical preamplifier [46]

Although EDFAs are the best solution in terms of gain and noise, the SOAs are the best solution in an integrated receptor because they can be integrated with the PIN in the same InP substrate. Considering the scenario where an SOA is utilized there are three configurations that can be tested. The first one is used as reference and is where the signal inputs directly the PIN. The second is the case where an SOA is put before the PIN. The last one is the one where an optical filter is put between the SOA and the PIN. Using a SOA of high gain (greater than 20dB) and low noise, the author of [47] obtained the following results:

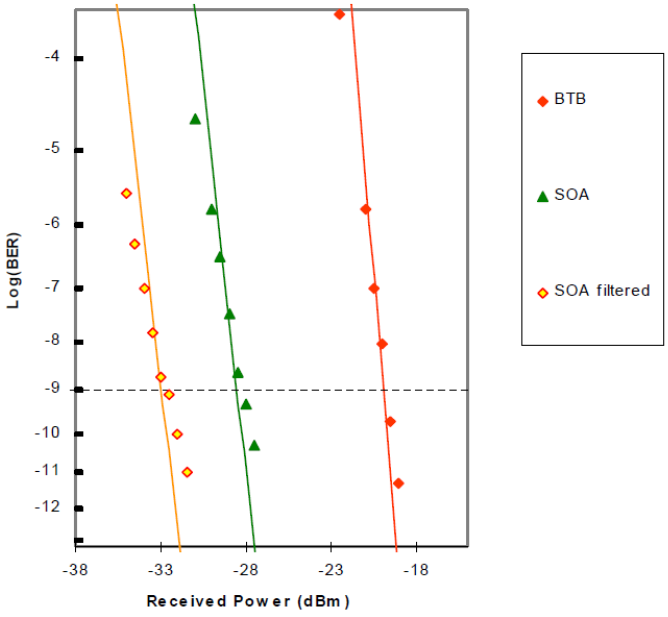

Figure 75 BER characterization of an SOA pre-amplified PIN receiver at 10 Gb/s [47]

Defining the receiver sensitivity as the received signal power for a particular BER, one can then conclude that there is an increase of the sensitivity with the use of the SOA. Analyzing the sensitivity for a BER of log(BER)=-9, the increase is over 5dB which can be considered a good improvement in the performance. When the filter was used, an increase of about 3dB, in relation to the previous case, is obtained. This value can be very useful in practical applications but one has also to consider the increase of the complexity and footprint of the integrated circuit.

4 PHOTONIC INTEGRATED TRANSCEIVER DESIGN

By collecting the information that is presented on the previous chapters one is then able to design a PIC. The design of a PIC consists of bringing together the basic building blocks that were presented. Although, as one may expect it is not as straightforward as that: there are procedures to follow as well as the tradeoff designs to be taken into account.

In order to do a better realization of a PIC, there are design rules to be followed. The design rules have the purpose to stipulate the distance that should be kept among the different components of the circuit. Regarding the separation between two waveguides there are two major limitations: coupling distance and technological limitation. The minimum separation that two waveguides can have is 400 nm and the minimum separation that guarantees no coupling is 10μm. The separation between waveguides and phase modulators is 10μm. The distance between two phase modulators is also 10μm which is given by the minimum distance between two metal contacts. Although in the case of deep waveguides their minimum distance to the phase modulator is 19μm. The separation between waveguides and gain sections is 30μm. The last case is the separation between metal pads and waveguides which is advised to be 5μm. Also one should take in consideration the crossing of two waveguides that should be done with a 90° angle in order to avoid crosstalk. All this information are given by the foundry [23].

It is also important to have an overview of the design flow. The first step is to design an application and then translate this application into an optical circuit by using the building blocks. In second place one should design and simulate the building blocks according to the specifications of the application. With the building blocks ready, one can then select one of the pre-defined cells that the foundry offers and then place the different building blocks on the mentioned cell following the design rules. In the end, after the debugging of possible errors with the aid of the software, the mask is generated and sent to the foundry.

In this chapter, the design process of a transceiver is presented. The chosen approach is top-down. A main overview of the transceiver circuit is first presented as well as the main features of it. Then the choice of the pre-defined cell and the different sections of the chip are presented.

According to the previous explanation the first design step is the application design. It defines the features that the final product should have. The transceiver should be tunable over different wavelengths with a spacing of 100GHz, at 1500nm, in order to be WDM compliant, in this case the transceiver comprises 4 different channels. It should also support the modulation formats QPSK and OOK-NRZ. Only one wavelength would be transmitted and received at a time. The local oscillator (LO) in the reception can be either input on the chip or a replica of the generated for transmission. With these specifications and using the building blocks presented in the previous chapter the block diagram of the optical circuit is presented in Figure 76. The only block that was not presented before is the one represented by RFT that is an MMI reflector which

is a standard building block of the foundry and works as a mirror with a defined reflection coefficient.

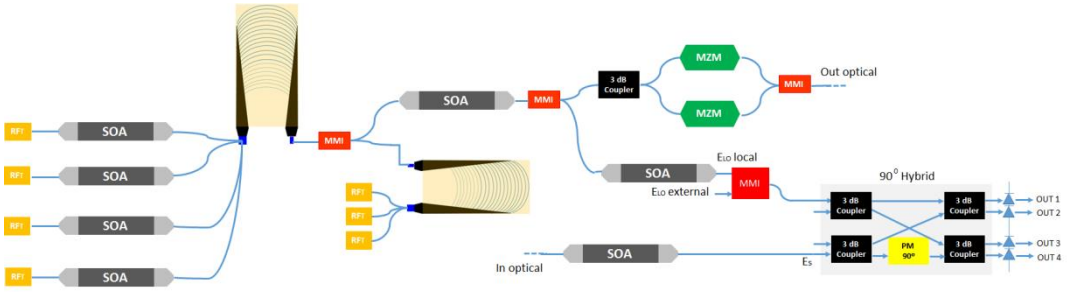

Figure 76Block diagram of the optical circuit of the transceiver

It is possible to identify three main blocks in the optical circuit: laser cavity, transmission (includes amplification and modulation) and reception. The laser cavity is composed by the devices in the light path from one set of reflectors to the other. The transmission is from the leftmost MMI to the *Out optical* excluding the bottom branch that exits the MMI before the 3dB coupler of the transmission. The remaining part belongs to the reception circuit. Each of this blocks' architecture is presented in detail shortly.

The choice of the pre-defined cell is also a step in the design procedure. As there are active elements in the circuit, one should choose among one of the layouts available for active cells.SMARTPhotonics foundry provides five layouts for the active cells which are presented in Figure 77. They differ in the position and number of the active zones on the cell. All the cells have a 4x4.6 mm^2 area.

Figure 77 Layout of the active cells [23]

Due to the geometry specifications of the components, the AWG is the one that has the bigger footprint inside the chip. Additionally, as one can observe on the block diagram of the circuit, most of the circuit is composed of passive devices thus cell number 3 could be rejected as it presents more space for the active region than the passive ones.

The performance of the optical modulator is optimized if they are placed in the same orientation of the active regions [23]. The optical modulators should be then positioned on the horizontal. In order to obtain the desired phase shift these devices are 2 mm long which is almost half the size of the chip thus cell number 1 and number 4 could not be used. The remaining cells are number 2 and number 5. The main difference between them is the active region of 1500 µm that is presented on the top left and bottom right of the cell number 5. According to the scheme presented in Figure 76, 7 SOAs and 4 PINs were used, the active regions in cell 2 are enough for these requirements as it will be seen in the next sections, thus cell 2 was chosen which also allows more room for the passive devices when compared to cell 5.

4.1 Laser Cavity

The idea behind the operation of the laser cavity was already presented in 3.2.2.2:Multiwavelength lasers. This part of the circuit has four SOAs, seven RFTs, two AWGs and an MMI. The extremes of the cavity are the two sets of reflectors. The AWGs, are the ones designed in 3.2.3.1:AWG design. The signal exits the laser cavity to the transmission block through the MMI.

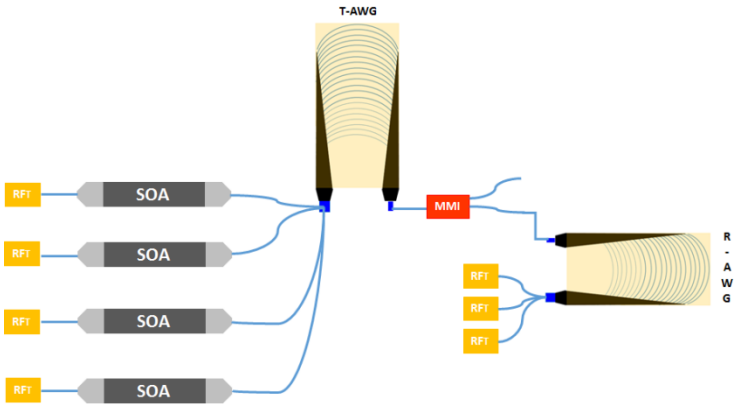

Figure 78 Block diagram of laser cavity

4.1.1 Operating Principle

In Figure 78 it is presented the block diagram of the laser cavity. The reflectors create a loop for the light between the SOAs and AWGs. Initially, the SOA is excited and it starts to amplify noise. The role of the T-AWG is to tune the amplified noise to a signal with a maximum at the maximum of the channel passband shape. As this tuning occurs, the noisy signal becomes a signal with a defined spectral component. The SOA in the steady state is then amplifying the light beam. The R-AWG is used to reject the copies of the signal created by the T-AWG due to its FSR.

The transceiver only emits one wavelength at a time. In order to choose which wavelength is used, the correspondent SOA is excited. The T-AWG has a geometry of 4x1, each of the 4 inputs is connected through an SOA and then a reflector. As each channel corresponds to a different wavelength, the switching of the correspondent SOA allows one to choose the desired operating wavelength.

4.1.2 On Chip Implementation

The on chip implementation of the laser cavity is presented in Figure 79.Only the optical components are shown in order to be easier to understand the picture. As one can depict, the devices that occupy more room are the AWGs and the bigger one is the T-AWG. The SOAs have to be placed in the active regions. As it was presented before, the gain of the SOA increases as the length of it increases however one should have to take in consideration the total number of the active areas and saturation phenomena. Each active region on the right top of the cell is 500 μm long, considering that there are eight active regions with those characteristics available and that the need is four SOAs in total the solution was to connect two active regions and make SOAs 1000μm long. In sum four 1000μm were obtained and all the active regions on the top right of the cells were used.

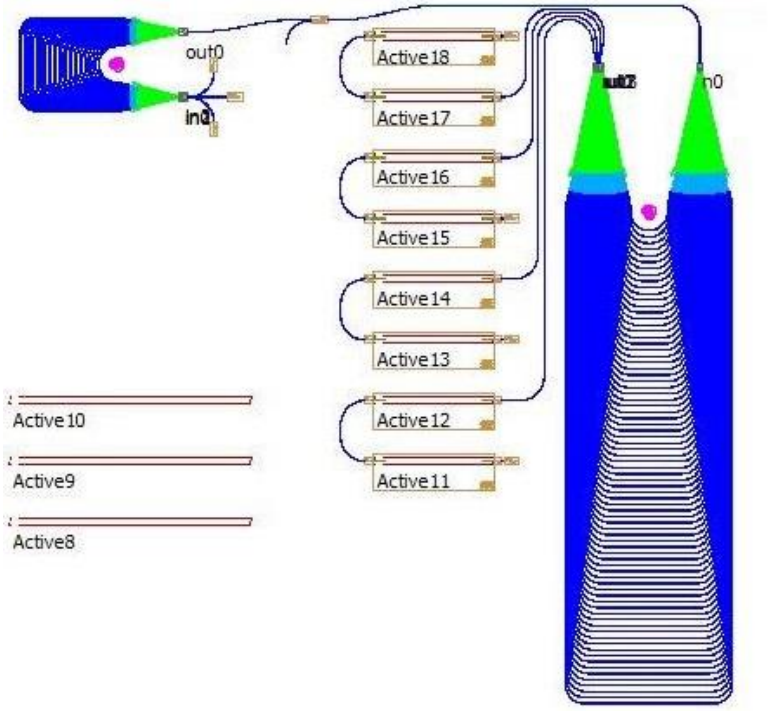

Figure 79 Aspect of laser cavity on the chip

On the chosen foundry technology there are two types of waveguides: deep and shallow waveguides. Each of them has its own features and use. For example, deep waveguides are

advised to be used in the connections of the different components in order to reduce the losses. Devices such as couplers are warned to be designed in shallow waveguides. The SOAs are done in shallow waveguides, and in order to connect them, deep waveguides were used. Thus, at the edges of the SOAs a deep to shallow transition was used. The deep to shallow transition is a standard building block presented in the library that allows both low loss and compact design and has a total length of 33μm.

The block that one can see at the right side of Active11 is the MMI reflector. This block can be connected to deep waveguides and in this design case is single input. The device is 26.2μm long, has an insertion loss of 2dB and a reflectivity of 0.5 to 0.6. In a worst case scenario, there are 5dB of losses in the device however this is the only feasible solution present at the moment since this is a nouvelle technology that is still in growth. An example of an MMIR is presented in the bottom of Figure 80. In the top it is presented a 1x2 MMI, where at the output there are 2 images of the input. In the MMI reflector, the device is cut at the position where the two images are. This cut is done in such a way that there is a reflection from one image to the other and there is constructive interference as it is reflected to the input.

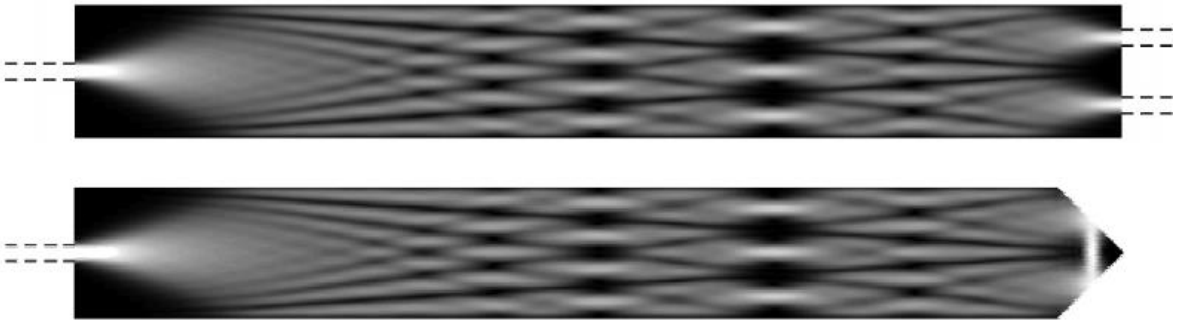

Figure 80 MMI examples. Top: MMI 1x2 Bottom: MMI reflector 1x0 [22]

4.2 Transmission Block

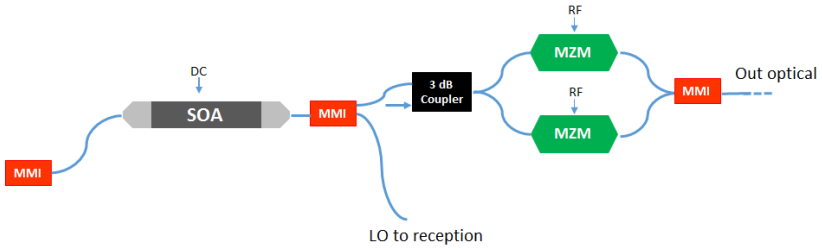

Figure 81 Block diagram of transmission block

The transmission block comprises the beam amplification and signal modulation. The input beam comes from the laser cavity and this block has two outputs. One is the modulated optical chip output and the other is the LO that is needed for the coherent detection in the reception block.

4.2.1 Operating Principle

After the laser cavity the signal goes through an SOA. The purpose of this SOA is to boost the quality of the signal so that the LO and the signal to be modulated have as much power as possible.

Following the amplification part, the signal is divided in the MMI which has one input and two outputs, having half of the original signal at each output. In the transmission block, the light goes then to the modulator. In Figure 56 (page 52) it is presented the IQ modulator. The light is divided into two equal beams which each of them follow to a MZM. In one of the branches an additional phase modulator is added so that one component is in-phase and the other is in-quadrature. Intensity modulation is performed in each branch in the MZM and the beams are then combined at the output of the two branches. In the designed case, the light is first divided in a 2x2 3dB coupler and then is directed to the two MZM. Each MZM is composed by an MMI at the input that splits the beam into two phase modulators where the RF signal is applied to modulate the light signal. At the output of the MZM another MMI is applied to combine the beams from each of its arms. The combination of the light coming from I and Q branches is done in an MMI with two inputs and one output. The signal outputs then the chip. One can then conclude that the chip, depending to the RF driving signals of the MZM, supports advanced modulation formats as well as OOK-NRZ. In order to obtain OOK-NRZ, the RF signals of the I branch should lead the ones from the Q branch by 90°in order to cancel the phase difference between the two branches. The logical information in both MZM must be the same.

The major difference that one can detect between the architecture presented in Figure 81 and the one that was described in the previous paragraph is that the input MMI that divides the beam to the I and Q branch and the additional phase modulator in the Q branch are replaced by a 2x2 3dB coupler. The 2x2 3dB coupler was presented in 3.5.1.2: 2x2 Waveguide Directional Coupler. It can be concluded that if only one input is used at the outputs one finds the original beam equally divided with the feature that there is a phase difference between the outputs of 90°. Those are the requested characteristics for the IQ modulator. With the replacement of the MMI and phase modulator by the 2x2 3dB coupler, the complexity of the design is simplified as well as the space on the chip is optimized. While in an on chip phase modulator, in the chosen foundry and to obtain a 90° phase shift, is 1 mm long and the MMI is 41.6μm long, the designed 2x2 3dB coupler is only about 400μm long.

4.2.2 On Chip Implementation

The on chip implementation is presented in Figure 82. The shadowed part of the chip is the laser cavity that was presented before as well as the room for the reception block. The rest of the chip concerns the transmission block. The RF and DC pads once again are omitted in order to simplify the interpretation.

On the top of the chip, the beam exits the laser cavity through the MMI. As the active regions on the top right side of the chip were used for the laser cavity, the active region used in this block is one of the central ones. These active regions are 1000μm thus the amplification part of the block is a 1000μm SOA. Once again, deep to shallow transitions are used at the edges of the SOA as well as in the MMI that follows the SOA. The MMI has one input and two outputs, one output is for the LO of the coherent detector and the other goes to the bottom part of the chip through a deep etched waveguide.

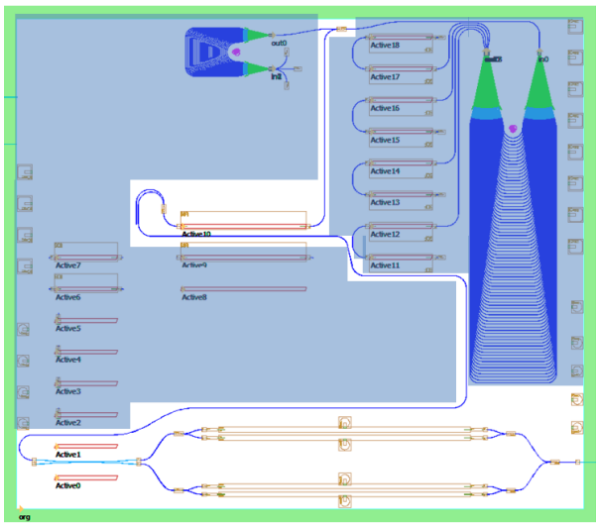

Figure 82 On chip laser cavity (shadowed) and transmission block

In the bottom of the chip is the IQ modulator. The device on the left is the 2x2 3dB coupler that was designed in 3.5.2:Directional Coupler Design and Results. Deep to shallow transitions were used at its edges because it was designed in shallow waveguide. The signal is split in two paths. Each path is composed of a 1x2 MMI, two phase modulators and a 2x1 MMI. At the end of both paths, a 2x1 MMI is used to combine the I and Q components and the modulated signal outputs the chip. The set of 1x2 MMI, two phase modulators and 2x1 MMI composes the MZM. Regarding the phase modulators they are placed in a parallel position to the active regions in order to obtain maximum efficiency from them [23]. The chosen length of the devices as well as the computation of V_π were already presented in 3.3.3.1:Mach-Zhender modulator modeling.

4.3 Reception Block

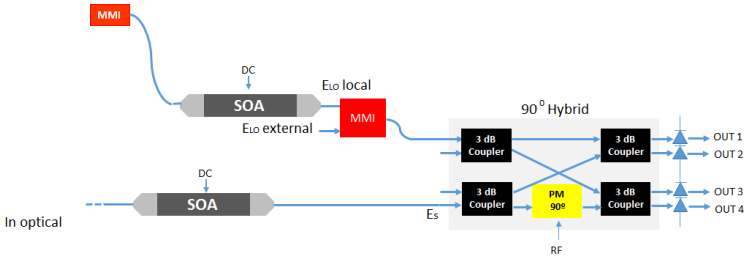

Figure 83 Block diagram of reception block

The reception block can be divided in two parts: the pre-amplification and the coherent reception. The latter one comprises the path of the LO and the 90° hybrid. The 90° hybrid is a key component in coherent receivers. In order to choose the best architecture for this device, in this section the theory and practical options of it are studied.

4.3.1 Operating Principle

SMARTPhotonics foundry only has available for reception PINs. With the analysis of the section where the receptors are presented one can conclude that in case the case that a PIN is used, pre-amplification is a good strategy to improve the signal reception. As it was presented in 3.6.4: PIN Photodetector with Optical Preamplifier, the best solution for preamplification is to use an EDFA. However this type of amplifiers was not available. Hence, an SOA was used for this purpose. In Figure 83, the SOA used for pre-amplification is the one on the bottom left. The signal enters the chip is pre-amplified on the SOA and goes to the 90° hybrid.

Before presenting the 90° hybrid one can be first introduced to the LO path. The LO is used for the homodyne detection. The LO, in order to the chip perform homodyne detection should be at the same frequency of the signal that is received. The simplest implementation is to obtain a replica of the beam generated in the laser cavity. This is the beam that comes from the top left MMI on the scheme. The beam is then amplified in order to optimize its performance. The SOA can also operate as a switch as it is explained ahead. In this design an external LO was also used. This external LO and the LO that comes from the laser cavity are the inputs of a 2x1 MMI. With the addition of the external LO, one can have the option to perform coherent detection using the LO generated inside the chip or with an external one. This guarantees not only the operation of the chip if the transmitter part is malfunctioning but also the tunability to different wavelengths than the ones generated on the transmitter side. With this feature, the device is able to operate in more versatile and expandable network scenarios.

If one wants to choose to use the external LO, the SOA in the path of the LO should be switched off and the external LO should be input on the chip. On the other way around if one wants to use the generated signals as LO, the SOA should be switched on and no signal should be injected on the optical input of the chip corresponding to the external LO.

4.3.1.1 Phase-Diversity Homodyne Coherent Detection

The detection techniques can be divided into two major groups: direct and coherent. Direct detection is simply implemented with a photodiode and is used to recover information from OOK-NRZ signal for example. On the other hand, coherent detection is a synchronous process and thus an extra laser is needed in order to be used as LO in the receiver. The difference between the angular frequency of the signal (ω_s) and the one of the LO (ω_{LO}) is called the intermediate angular frequency (ω_{IF}) (IF). Depending on the value of IF, coherent detection can

be classified heterodyne or homodyne. If the IF is much bigger than half the bandwidth of the carrier determined by the bit rate, it is heterodyne detection. If the IF is null one has homodyne detection. The difference is presented in Figure 84. Thus, one can conclude that in homodyne detection, the frequency of the signal and the frequency of the LO are the same.

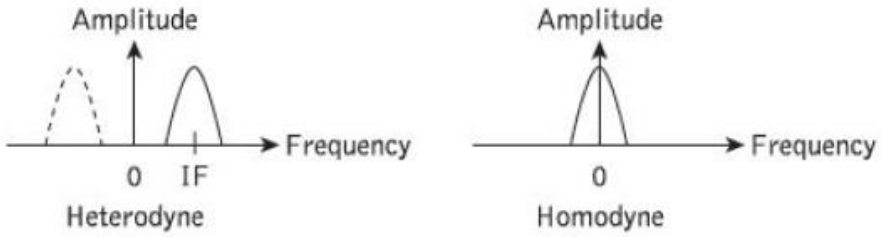

Figure 84 Spectral comparison between heterodyne and homodyne detection [31]

It can be proved that with homodyne detection one can not obtain both in-phase and quadrature components [31]. However, if one uses a 90° shifted version of the LO all the information of the complex amplitude can also be extracted. That is the phase-diversity homodyne detection which implementation is shown in Figure 85.

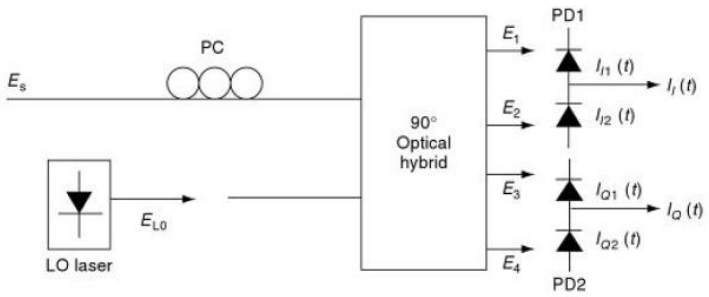

Figure 85 Illustration of phase-diversity homodyne detection principle [31]

The output fields of the 90° optical hybrid are given by:

$$E_1 = \frac{1}{2}(E_s + E_{LO}) \quad (4.1)$$

$$E_2 = \frac{1}{2}(E_s - E_{LO}) \quad (4.2)$$

$$E_3 = \frac{1}{2}(E_s + jE_{LO}) \quad (4.3)$$

$$E_4 = \frac{1}{2}(E_s - jE_{LO}) \quad (4.4)$$

These outputs are detected in balanced photodetectors. The implementation of the 90° optical hybrid was a great concern on the scope of this thesis. Its operation as well as several practical implementations were studied and are presented briefly in the next subsection.

4.3.1.1.1 90° Optical Hybrid

The 90° optical hybrid has several implementations. In this work, the goal was to obtain an architecture that could be integrated with the building blocks available in the chosen technology. To do so, the journal article by Matthias Seimetz and Carl-Michael Weinert [48] was studied. It presents three different implementations and a comparison among them. The first option was to use four 3dB couplers and a phase delay in one of the branches. It requires an active control loop to stabilize the 90°balance. The second one is a 4x4 MMI coupler which by properly choosing the input ports as well as a correct dimensioning of the device, the needed 90° property is inherently given. The last option is to use a normal 3dB coupler combined with two polarization beam splitters (PBS). This setup requires specific polarization states of both LO and signal. In Table 7 one can find a comparison of the three options.

Device	Commercially available?	Pros	Cons
3-dB coupler & phase delay	Yes	Structure can be also used for DQPSK demodulation	Active control loop required
4x4 MMI coupler	No	Stable phases, broadband, integration of balance detectors	Spot size converter integration
3-dB coupler & PBS	Discrete components	Easy built-up with discrete components	Polarization requirements, more an option for laboratory

Table 7 Availability, pros, and cons of different 2x4 90° hybrid options [48]

By gathering the information on the table one can start to exclude the option of 3-dB & PBS because it is difficult to integrate and has polarization requirements for the inputs which would increase the complexity of the system. Between the 3-dB coupler & phase delay and the 4x4 MMI coupler options, in theory the 4x4 MMI coupler would be the best option. It would occupy less room on the chip, offer more stability to the chip and would be less complex because it would not require the active control loop. An integrated wideband device with this architecture was already fabricated and tested [49]. However, the spot size converter that must be used for integration is not available in the SMARTPhotonics foundry thus the choice was a 3-dB coupler & phase delay.

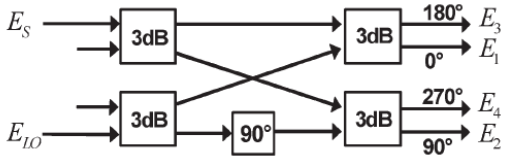

Figure 86 90° hybrid with four 3-dB couplers and a phase delay [48]

The chosen configuration is presented in Figure 86. The relative phase shift of the four output signals is depicted in the figure. One can also compute the fields at the output by using the transfer matrix presented in 3.5.1.2: 2x2 Waveguide Directional Coupler yielding to [48]

$$\begin{bmatrix} E_3 \\ E_1 \\ E_4 \\ E_2 \end{bmatrix} = \frac{1}{2}\begin{bmatrix} E_s - E_{LO} \\ -jE_s - jE_{LO} \\ -jE_s - jE_{LO}e^{j90^\circ} \\ -E_S + E_{LO}e^{j90^\circ} \end{bmatrix} \tag{4.5}$$

One can notice that the additional phase shift of 90° was written separately. This was done to highlight that a small deviation on this phase shift, leads to the degradation of the reception process. In order to solve this problem, an active control loop should be implemented. The authors of [48] propose an implementation of this control loop. The control loop is to be implemented outside the chip thus a specific hardware implementation is not discussed in the scope of this thesis. The idea behind the implementation is to add a control signal to the input signal with a wavelength different than the LO (which is the same as the data signal). Then the control signal heterodynes with the LO and data signal. After the 90°hybird and balanced detection, two electrical control signals can be extracted. One for the I component and the other for the Q. The control signals can only be extracted by bandpass filtering at an intermediate frequency (w_{IF}) that is given by the difference of the wavelength of the control signal and the wavelength of the data signal. This intermediate frequency has also to lie outside the bandwidth of the data signal in order to avoid interference between the control signals and the I and Q photocurrents. The control signals have a phase shift φ to each other that is related to phase deviation in the hybrid. Denoting by I_{CTR} the resulting current after combining the control signals in a mixer, one can write [48]

$$I_{CTR} \sim -\frac{1}{2}[\cos(2(w_{IF} + \varphi_{Ctr} - \varphi_{LO}) - \varphi) + \cos(\varphi)] \tag{4.6}$$

where φ_{Ctr} is the phase of the control signal and φ_{LO} is the phase of the LO. In Equation (4.**6)** one can observe a double frequency term and a DC term. By low pass filtering the control current, only the DC term remains. This DC term is zero for phase shifts of the form $90^\circ + n * 180^\circ(n\ integer)$ but not for the other phase shifts. This control current, inputs in the phase modulator in order to obtain stable operation of the 90°hybrid.

4.3.2 On Chip Implementation

One can observe the on chip implementation of the reception block in Figure 87. The laser cavity and the transmission part correspond to the shadowed part. The DC and RF pads are not shown in order to simplify the reader's task.

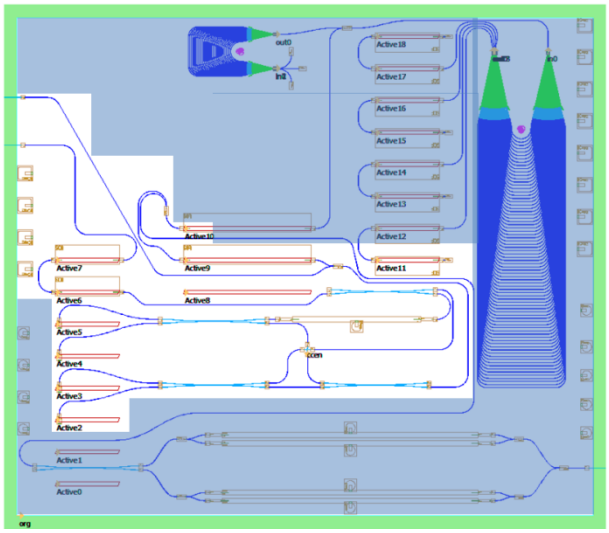

Figure 87 On chip laser cavity and transmission block (shadowed) and reception block

At the left side of the chip there are two optical inputs. The one on the top corresponds to the external LO and the remaining corresponds to the input data signal. In order to perform preamplification, the input data signal is driven to the left side active regions. They were used in order to avoid the crossing between waveguides. These active regions are 500μm long. In order to obtain a 1000μm SOA, two active regions were connected. The external LO is directly connected to a 2x1 MMI. As the input of the chip is a shallow etched waveguide, first there is a shallow to deep transition followed by the deep etched waveguide that conducts the external LO to the MMI. The other input of the MMI is the LO that is generated in the laser cavity. This signal, after leaving the MMI that was already presented in transmission block is then amplified in the active region 9 which has a length of 1000μm. At the input and output of the SOAs, MMIs and 3dB couplers were always used a deep to shallow and shallow to deep transition respectively.

The remaining part of the design concerns the 90°hybrid. The 2x2 3dB couplers are the ones presented in 3.5.1.2:2x2 Waveguide Directional Coupler. The additional phase modulator is used in the upper branch. It is the same building block as in the arms of the MZM although since in this case only 90° phase shift was needed, the length of the device is 1 mm. In the IQ modulator the chosen orientation of the phase modulator was to be parallel to the active regions in order to obtain maximum performance. Between the right and left 2x2 3dB coupler one should take in consideration the crossing of the waveguides. The crossing was of great concern in order to avoid crosstalk. It is not recommended that deep etched waveguides cross, thus deep to shallow and

shallow to deep transitions are placed and the crossing of the shallow waveguides is done at 90° as this is the angle that presents less losses [23]. After the four outputs of the 90° hybrid, the signals go to the PINs. The length of the waveguides between the output of the 90° hybrid and the PINs was made the same so that no additional phase shift is added among the output signals. As in the chosen foundry, balanced detectors are not available, PINs were used. PINs have to be placed in active regions and are 30μm long. Not much information is available about them in the design manual [23] as they are considered to be a new component. Four electrical signals output then the chip, as can be seen in Figure 88 where all the DC and RF pads are included.

4.4 Final Design Considerations

The final layout of the chip is presented in Figure 88. It includes the DC and RF pads and wires. The brown ones represent the DC and the blue the RF pads. The DCs are used for the SOAs and the phase modulator on the reception. The RFs are used for the IQ modulator and PINs.

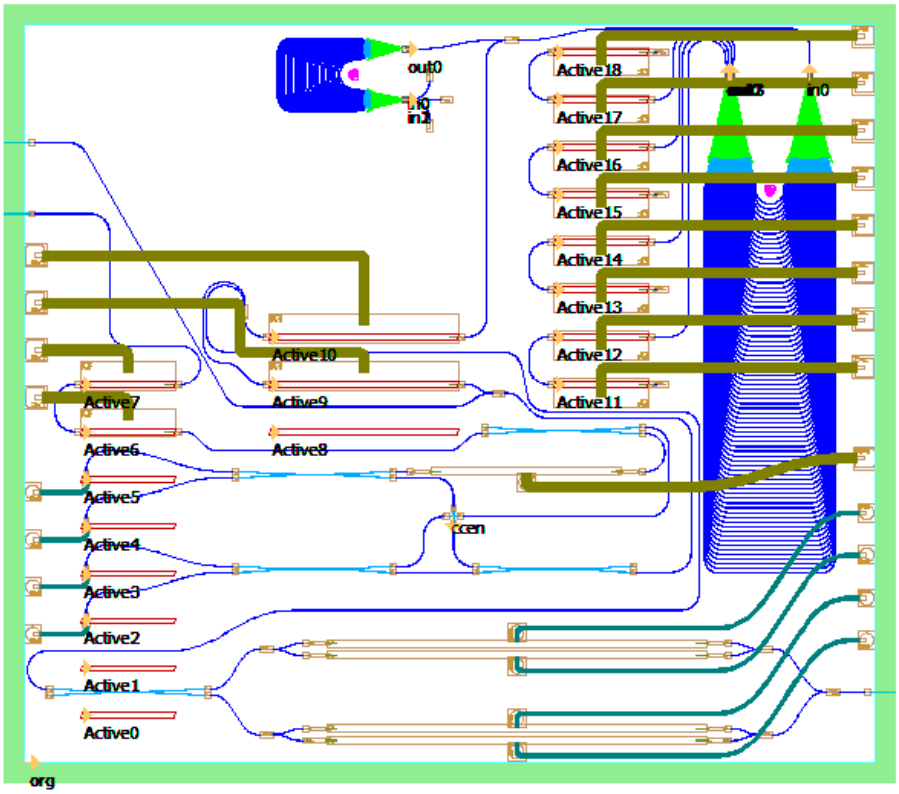

Figure 88 Final layout of the chip

At the edges of the chip, there are the DC and RF pads. Their size and position can be changed, however one should take in consideration physical limitations. Regarding the optical inputs and outputs (IOs), if two are adjacent at least 125 μm should be left between them. This is the value of the diameter of the fibre that can be connected to the chip. Two consecutive RF/DC

IOs should be left apart at least 100μm. This distance is a physical limitation imposed by the bonding machine of the department. The bonding wires are placed in the DC/RF pads during the bonding process.

The last step on the design process is the submission of the design. First one has to open the MaskEgineer® software that is part of the Phoenix Software® pack. After opening it, the Design Rule Check should be run in order to find if the design can be produced in the foundry process. If no problem is shown in the Design Rule Check process, one can start to export the mask for the foundry. This process generates several files which should be zipped and sent to the foundry. Among the generated files is the final mask layout that is presented in Figure 89. With the mask created, the active zones that are not in use should be deleted.

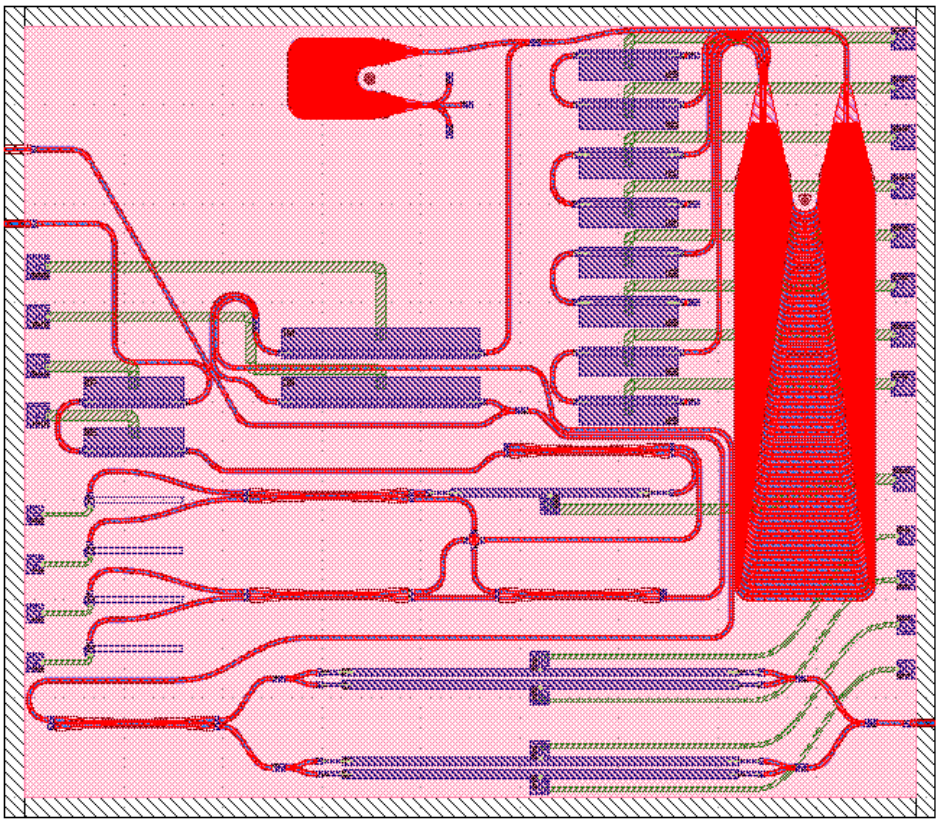

Figure 89 Final mask layout of the chip

5 LABORATORY EXPERIMENTS AND RESULTS

Up to this point of the document, PIC components were presented. Some of them were also designed and modulated. With these components, an optical chip was designed. The circuit of the chip is a tunable transceiver that supports four wavelengths of operation that are separated by 100GHz which are features for a WDM system. The chip also enables the use of higher order formats of modulation and the option to use as LO an external input or the on-chip generated laser. In this chapter, it is presented the laboratory work done to emulate the designed chip.

Laboratory work was done to test how the chip works in a system. Lasing was done through a feedback loop as in the laser cavity of the chip. This signal was then modulated in an IQ modulator and with a coherent detector, the signal was detected and characterized in back to back and after 40 km of Standard Single Mode Fibre (SSMF). The reception system was tested in two ways: when the LO was the laser created in the feedback loop and when an external light source was connected. In order to characterize the system, error vector magnitude (EVM) was measured for different values of power at the input of the coherent receiver. Eye diagrams and constellations of the received signal were also obtained so that a deeper comparison could be done.

5.1 Laboratory Setup

In the laboratory, two setups were used. This was done to test the reception system in two ways: when the LO was an external cavity laser (ECL) and when it was the laser generated in the feedback loop. In Figure 90 one can see the setup of the former and in Figure 91 one can analyze the setup of the latter. For each setup, measurements were done for back to back and with 40km of SSMF.

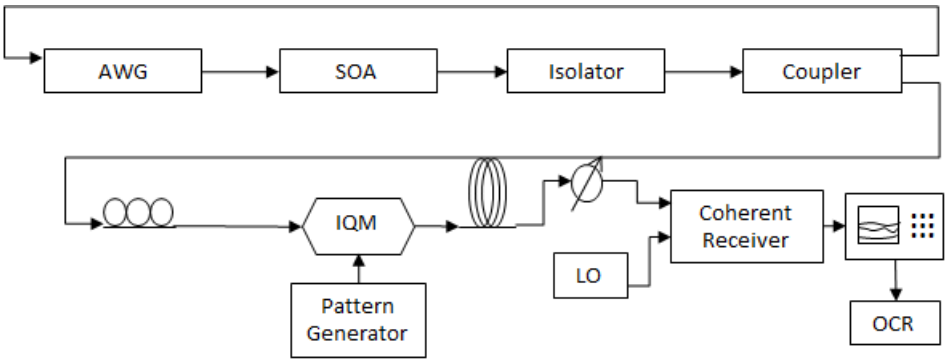

Figure 90 Laboratory setup with ECL as LO

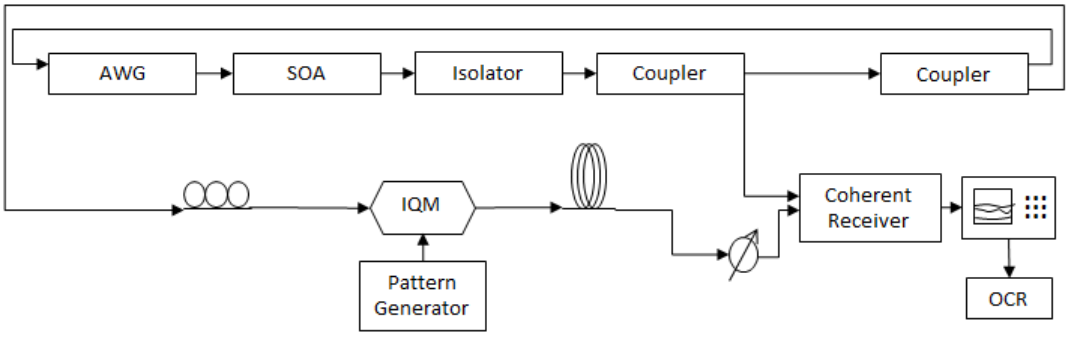

Figure 91 Laboratory setup with generated signal as LO

One can conclude that both setups are similar in the upper branch. This branch is the feedback loop where the laser is generated. The difference between Figure 90 and Figure 91 is that in the latter one, an extra 50/50 coupler is added and the light generated in the laser feedback loop is used at the input of the coherent receiver. With the presented setups one can verify that fibre was used between the IQ modulator and the variable optical attenuator (VOA). In each setup, this module of fibre was removed in the back to back experiments.

The analysis of the setup can start on the feedback loop. The leftmost device on the block diagram of the setup is the AWG. It had 40 channels and a channel spacing equal to the one used in the chip design i.e. 100GHz. Following the AWG there is a C-Band SOA (SOA-S-OEC1550). Before the 50/50 coupler, an isolator was used to guarantee that there was no reflected light going to the SOA. This was done to improve the performance of the feedback loop. At the output of the 50/50 coupler, in the setup where the ECL is used as LO one half of the signal is used to feed back the loop (input of the AWG) and the other outputs to the polarization controller (PC) . In the other case (generated laser as LO), one output of the coupler goes to the LO input of the coherent receiver and the other to another 50/50 coupler whose outputs feedback the loop and go to the PC.

The next part of the setup regards the signal modulation and transmission. It includes the PC, the IQM, the pattern generator and the fibre (in the case of 40 km experiment). The IQM is a 22.5GHz IQ modulator that is driven by a pattern generator (SHF12100B). At the output of the IQ modulator there is a QPSK 10Gb/s signal that is sent to the fibre in the case the transmission over 40km of fibre was tested. The fibre was a SSMF which had an attenuation coefficient of 0.2dB/km and dispersion of 17 ps/nm/km.

The reception of the signal is performed in the remaining components. A VOA is used in order to limit the power at the coherent receiver input whose maximum input power is -6dBm. The coherent receiver is composed by a 90° hybrid and a pair of balanced detectors. In the case that the local oscillator in use is the external one, it is an ECL with a linewidth of 100 kHz. This is a C-Band tunable laser that was tuned to the frequency of the obtained signal in the laser feedback.

The resulting electrical signal, is then digitalized by a 50GSa/s real-time oscilloscope (Tektronix DPO72004B). The oscilloscope was connected to the Optical Coherent Receiver (OCR) analyzer via Ethernet.

OCR is a digital signal processing software whose interface was developed in Matlab® GUI in Instituto de Telecomunicações, Pólo de Aveiro. Its main use is in systems that employ multi-level modulation such as QPSK. As it is known, this type of modulation format require coherent detection and can also be transmitted through the same channel with two polarizations. The software analyzes the transmission system using the parameters: EVM, BER and eye-diagram characteristics. The software also performs the compensation of the received signal using real time digital signal processing (DSP). Additionally, it compensates transmission impairments such as polarization mode and chromatic dispersion.

5.2 Laboratory Results

After exiting the laser cavity, the beam was modulated at a rate of 10Gb/s. In order to characterize the reception of the different signals, the power at the input of the coherent receiver was swept using the VOA .

For the different values of the power at the input of the coherent receiver, with the aid of OCR the signal characteristics were measured. In this subsection the generated laser, the spectrum of the received signal, the signal constellations, the variation of the EVM with power at the input of the coherent receiver and the eye diagrams are presented and discussed. The EVM were obtained for 4096 recovered symbols, over 3 independent measurements.

The signal constellation is a representation in the complex plane of the positions of the received modulated symbols. Ideally, no deviation from the precise constellation points at the reception should be noted. However, this is not what occurs in real systems. Noise, delay and phase noise are also present and lead to the deviation of the points. EVM can be considered to be the measure of this deviation (i.e. it measures how far the points are from the ideal locations). EVM is an important metric in a system and can be related to other metrics of the system such as BER and SNR [50]. As a reference, for the limit performance when the system presents a BER of 10^{-3} the corresponding EVM is approximately 32.4% or -9.79 dB. The eye diagram is a method to display the signal where different received symbols are overlaid. It allows one to have a perception of the quality of the system in terms of threshold level in amplitude and time.

The presentation of the results is divided in three sections. The first one regards the obtained laser signal in the feedback loop and the remaining two to the setups that were presented before. For each setup the analysis of back to back and after 40km of SSMF is performed.

5.2.1 Laser Obtained with the Feedback Loop

At the output of the laser feedback loop the optical spectrum analyzer (OSA) APEX-AP2441 was used before the transmissions measurements were done in order to verify the quality of the obtained signal and characterize it.

The spectrum of the obtained laser is presented in Figure 92. The wavelength peak was located at 1550.3nm. Other channels of the AWG were tested around 1550nm however this was the one that proved to perform better in terms of power and linewidth of the generated signal.

The characterization of the laser signal was done by measuring two parameters: power (peak and total) and linewidth (at 3 and 20 dB below the peak of the signal). The total power was measured with a power meter and the other parameters were measured with the OSA.

The peak power of the signal was 6.3 dBm and the total power was 7.4 dBm. Ideally, the peak and total power should be the same because the ideal linewidth of a laser is zero (unique spectral component). However, one can conclude that the power of the signal is concentrated around the laser peak which is a good feature. The power at the output of the laser was a concern because it should be enough to enable good performance of the IQ modulator and the coherent receiver in the case it is used as LO.

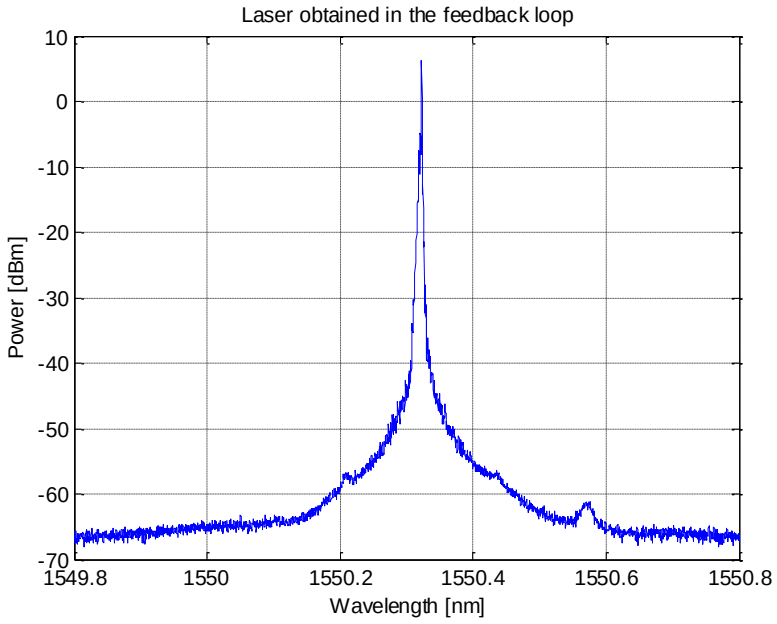

Figure 92 Spectrum of the laser obtained with the feedback loop

The linewidth of the laser is due to phase and frequency fluctuations caused by spontaneous emission. In the system tested, the widening of the linewidth causes a degradation on the performance of the IQ modulator and especially on the coherent receiver because

homodyne detection only occurs if the frequency of the signal is equal to the one of the LO. The measurement of the linewidth of the laser can be very time consuming and difficult. The technique used in the laboratory was to directly use the option of measuring the linewidth with the mentioned OSA. The 3dB linewidth measured was 0.0009434 nm. In terms of frequency at 1550.3nm this corresponds to 117.7MHz. The last measured parameter was the 20dB linewidth that was 0.0049943 nm. At 1550.3 nm it is equivalent to 622.9MHz. When these values are compared with the linewidth of the external laser that was used as LO which was 100kHz one can state that they differ. This can lead to degradation in the performance of the system where the created laser is used. One should notice that this laser was obtained with discrete components interconnected which lead to losses and instability of the feedback loop degrading the quality of the generated signal. Monolithically integrated feedback-lasers with narrow linewidth (150 kHZ) were already reported [5]. This can lead to the conclusion that the integrated version of this laser can perform even better than the one tested in laboratory.

5.2.2 Results of Setup with ECL as LO in the Coherent Detector

The received spectrum of the signal for a power of -27dBm at the input of the coherent receiver is presented in Figure 93. As expected, the signal is in the baseband which is due to the fact that homodyne detection was used. Moreover, as stated before the signal was modulated at 10Gb/s which means that there are 5 GBaud. This is the reason to have the first null of the spectrum at that frequency. As the spectrum has a sinc shape, the other nulls are the integer multiples in frequency of this value which correspond to the obtained spectrum. Relative to the power density, the values presented in the correspondent axis refer to a power density after the DSP in the OCR was applied. This DSP has a normalization value which leads to a shift of the spectrum in the vertical axis.

With the setup presented in Figure 90, first for a case in which no fibre was used the resulting variation of EVM for different powers at the input of the coherent receiver is presented in Figure 94 (left). From its analysis, one can determine that with an increase of the power at the input signal, a decrease of the EVM occurs leading to better performance of the system. For coherent receiver input power greater than -30dBm, the variation of the EVM is not very significant and one can conclude that the system is in a stable operating point. It is also important to notice that in back to back mode of operation, not even with -41dBm at the input of the coherent receiver the mentioned limit performance of -9.79dB of EVM is achieved.

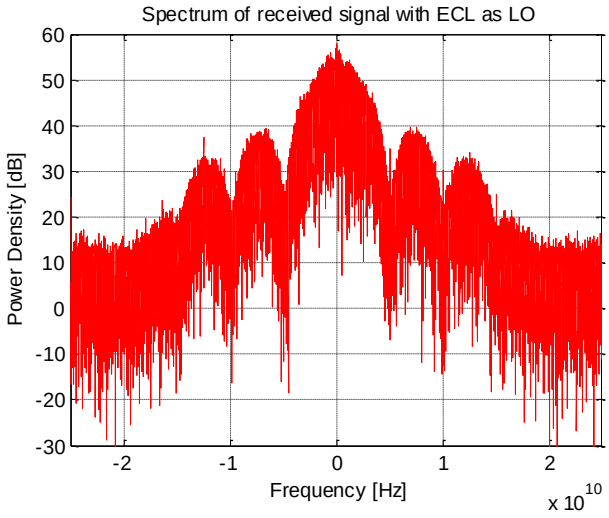

Figure 93 Spectrum of the received signal with ECL as LO

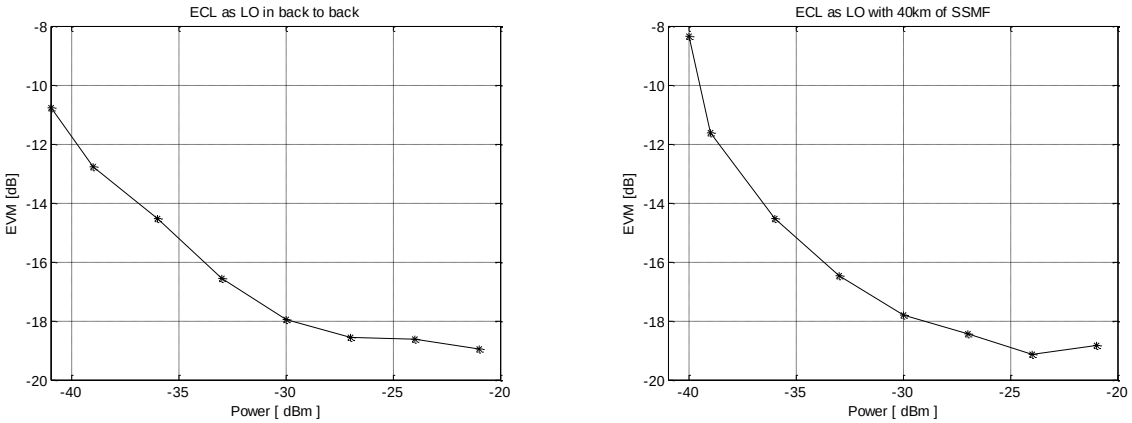

Figure 94 Relation of EVM and power at the input of the coherent receiver with ECL as LO. left: back to back right: with 40km SSMF

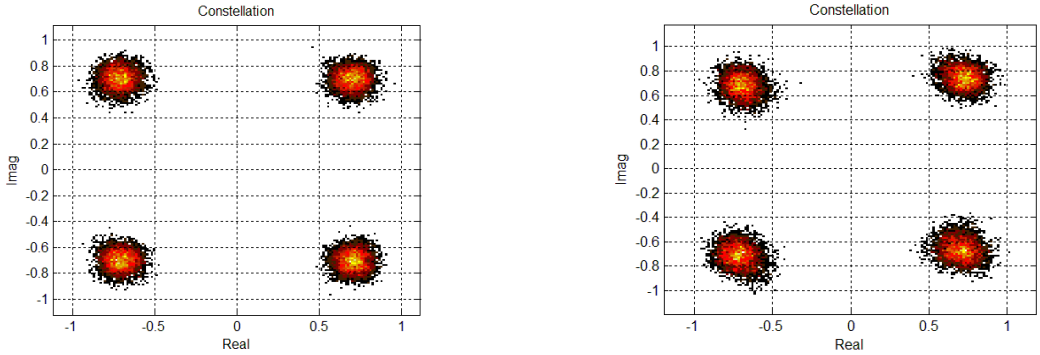

Figure 95 Constellation of the received signal for -27 dBm with ECL as LO. left: back to back right: with 40km of SSMF

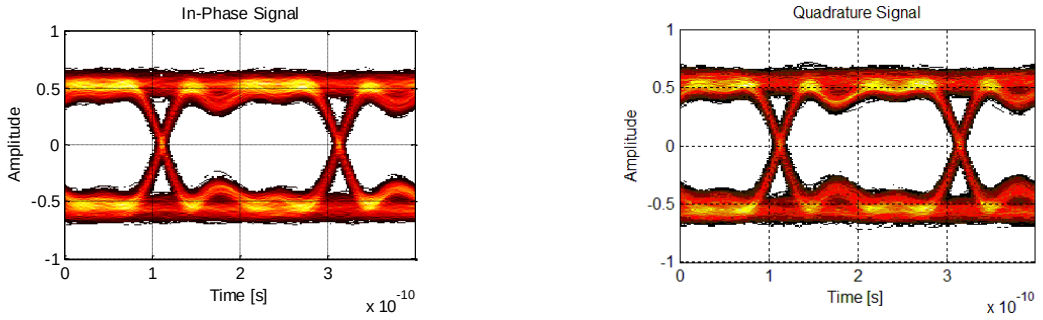

Figure 96 Eye diagram of the received signal for -27dBm in back to back. Left: in-phase Right: quadrature

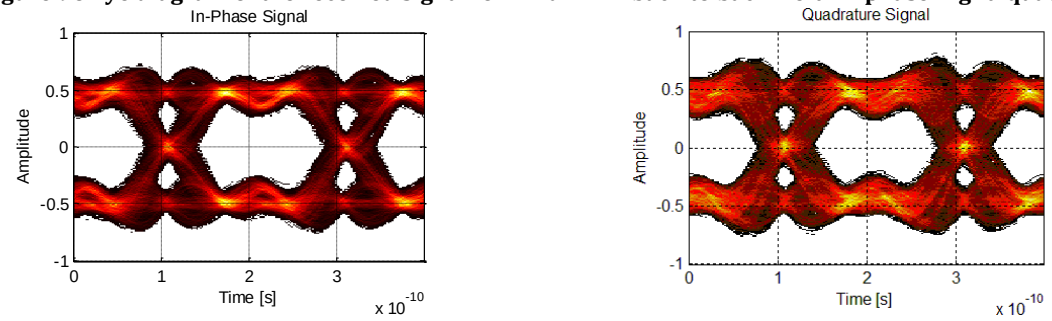

Figure 97 Eye diagram of the received signal for -27dBm with 40km of SSMF. Left: in-phase Right: quadrature

The results for the case in which 40km of SSMF was used are presented in Figure 94 (right). As in the case of back to back one can conclude that for powers equal or greater than -27dBm, the system is in a stable operation point as the variation of the values of EVM are small. As in the previous case, with a decrease of power, the value of EVM increases. Using fibre, with the decrease of power, the increase of EVM is more visible. Also, the limit level for the system performance (-9.79dB) is achieved before -40dBm. Thus, the introduction of the fibre, as expected degrades de performance of the system. For a better analysis and comparison of the result, the constellation of the signal and eye-diagrams were obtained for both cases with -27dBm at the input of the coherent receiver. The results are presented in Figure 95, Figure 96 and Figure 97. Regarding the constellations of the signal, one can observe that both have small deviation from the ideal points as it was expected from the analysis of the EVM values. It is also possible to state that in the constellation corresponding to the case in which the fibre was used, the points of the constellation are more scattered, which is due to the dispersion introduced in the fibre. Concerning the eye diagrams, the differences between the back to back and 40km of fibre are more visible. In the back to back case, the eye diagram is open in terms of amplitude and time which respectively lead to good threshold level and good sampling time. The jitter (time taken in the crossing states) is small as well as the noise for the '1' and '0' level. On the other hand, the eye diagram of the system with 40km of fibre has more noise in the '1' and '0' levels which lead to a worse decision level when compared to the previous case. Moreover, the jitter in this case is bigger and is cause by the dispersion of the fibre.

5.2.3 Results of Setup with Generated Laser as LO in the Coherent Detector and Comparison with the case of ECL as LO

In this subsection the results of the setup presented in Figure 91 are presented as well as a comparison with the results that were obtained in the previous subsection. The parameters for the case of the setup with generated laser as LO in the coherent detector were taken for an input power at the detector of -24 dBm, which as it will be presented allows the system to be in a stable point of operation.

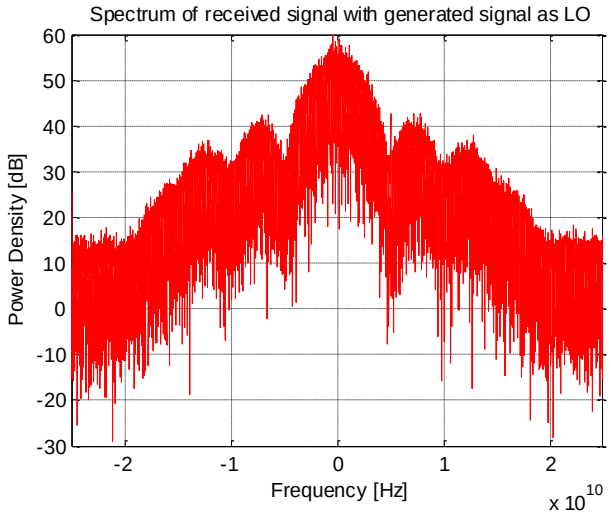

Figure 98 Spectrum of the received signal with generated signal as LO

In Figure 98 one can find the spectrum of the received signal of the setup under study. As in the case of the spectrum of Figure 93 the signal is in baseband due to the homodyne detection and the first null correspond to the frequency at which the symbols are transmitted (5 GBaud). However there are differences between the spectra. They concern the side lobes of the sinc shape. In the case under analysis, the noise is predominant on the side lobes and one can not clearly identify the sinc shape beyond the main lobe. These differences can be explained by the fact that the generated laser inputs less power in the coherent detector than the ECL LO. Also, the linewidth of the generated laser is bigger than the one of the ECL.

The plots of the variation of the EVM with the power at the input of the coherent receiver for back to back and using 40km of SSMF are presented in Figure 99. From their examination one can conclude that with the increase of the power there is a decrease on the EVM as in the previous case. Comparing the results of both setups one can conclude that the lower limit of the EVM is higher in the case where the generated signal is used as LO. This means that even in a stable mode of operation, when using the generated laser as LO, the deviation of the received symbols from the ideal points in the constellation is larger than in the previous case. When one uses the generated laser as LO even in back to back case the performance limit of -9.75dB for the

EVM is met for input power smaller than -34 dBm in both cases. One can also conclude that, in this case, with the reduction of power there is a more accentuated increase of the EVM when compared to the case in which ECL was used as LO. The constellations for the input power of -24 dBm are presented in Figure 100. Once again, the scattering of the received symbols on the plot is more visible in the case when the fibre was used, which was expected due to the dispersion introduced by the fibre. By comparing the obtained constellations of both setups, the difference of the quality of the received signal becomes more evident. The constellations of the setup that uses the ECL as LO, are more concentrated around the ideal points for the back to back and 40km of SSMF case. This can lead to a relaxation on the parameters of the threshold levels when compared to the case that the generated signal is used. These results are corroborated with the eye diagrams that are presented in Figure 101 and Figure 102. The amplitude of the noise on the '1' and '0' region increased when compared with the results of the previous setup. One has then to solve the tradeoff between the reduction of complexity of the system by using the generated signal as LO and the reduction of complexity of hardware specifications for the threshold levels by using the ECL as LO. The differences between the two studied setups can be explained by the fact that the generated laser inputs less power in the coherent detector than the ECL LO. Also, the linewidth of the generated laser is larger than the one of the ECL.

In sum, one can conclude that the system performs better when the ECL is used as LO. However, stable operation can also be achieved when the generated signal is used as LO. One should be aware that in that situation a penalty on the system performance occurs which leads to constraints in the threshold levels and an increase of the needed power at the input of the coherent detector.

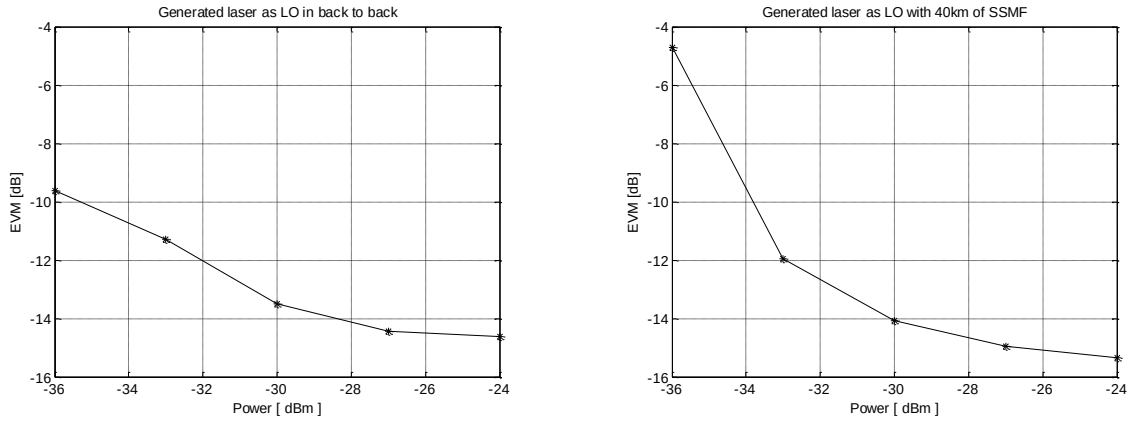

Figure 99 Relation of EVM and power at the input of the coherent receiver with generated signal as LO. left back to back right: with 40km of SSMF

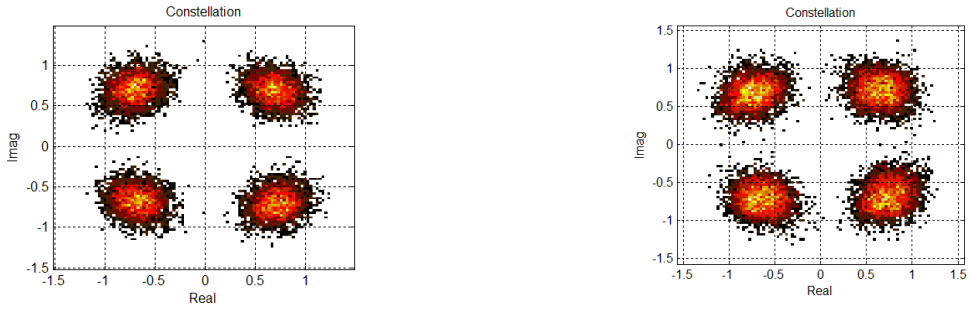

Figure 100 Constellation of the received signal for -24dBm with generated signal as LO. Left: back to back right: with 40km of SSMF

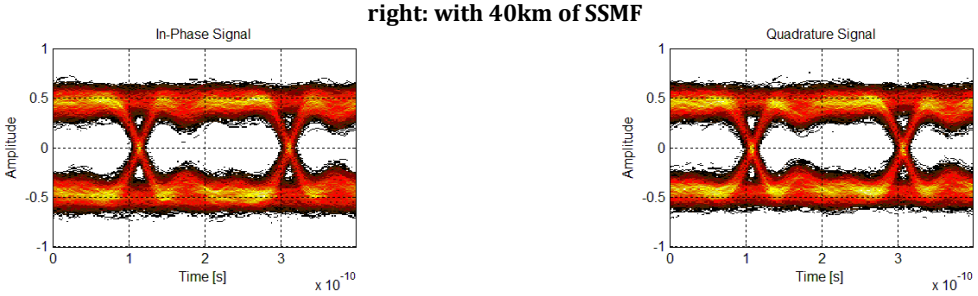

Figure 101 Eye diagram of the received signal for -24dBm in back to back. Left: in phase Right: quadrature

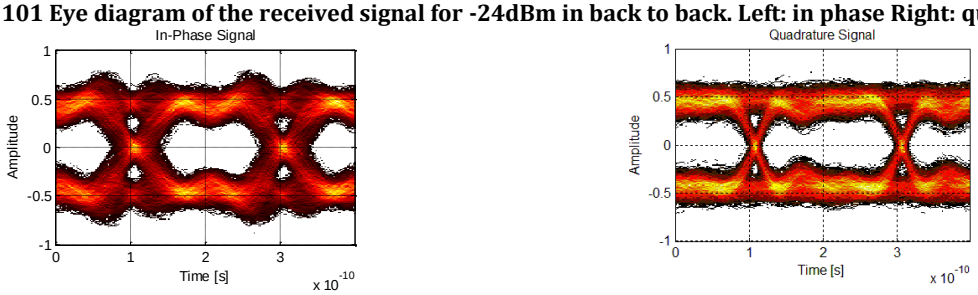

Figure 102 Eye diagram of the received signal for -24dBm with 40km of SSMF. Left: in-phase Right: quadrature

6 CONCLUSIONS AND FUTURE WORK

Nowadays the majority of the world population is connected by networks. New paradigms of entertainment, shopping and even human relations appeared. Every day the network users become more eager for information and its speed. These expectations all around the world are bringing the network capacity to its limit.

In order to satisfy the customers, the service providers already realize that optical communications are the solution. This technology enables bitrates in the order of Terabits. However, the current standards applied and under development are not still able to achieve fibre's capacity of transmission. Many researches have been carried out to improve the transmission bitrates. All of them use higher order modulation formats such as QPSK. The spectral efficiency to provide higher bitrates can not be offered by on-off keying modulation, thus the use of advanced modulation formats is mandatory. These modulation formats convey the information in phase (QSPK) and phase and amplitude (QAM). Coherent detection is then needed because direct detection only recovers the information in the amplitude of the carrier.

Another trend that needs to be followed in optical communications is the PICs. From the service providers perspective the cost per client and application is very important. The fact that a single chip can comprise the functions of several discrete components can only mean one thing: saving. Saving in terms of room, costs and power. The chips save the time and work from assembling the different discrete components and enable mass production which lead to a massive reduction of costs. With PICs, the power consumption is reduced as well as the complexity of the networks. Moreover, the stability of operation of the networks increases as the probability of component failure decreases. From a user perspective, the preference for small devices is well known especially when they provide an increase on the performance of the system which is what occurs with PICs.

With the design of a PIC in mind, a chapter in this thesis was devoted to present its different component. A theoretical overview was given for each of them and the design and modulation of specific components was also presented. The obtained models are for a specific foundry (SMARTPhotonics) and were done in the VPITransmission® platform. The components for the several parts of the final transceiver were designed separately. So that, in the chapter of the design of the PIC they can be put all together in the respective block of the circuit.

In the part of the document relative to the design of the integrated transceiver, the architecture of the circuit was discussed and divided into blocks. The different blocks were then designed using the components that were presented before. As a final result, a transceiver for hybrid PONs was obtained. The term hybrid refers to WDM networks that support advanced modulation formats. The device is tunable over 4 channels separated by 100GHz in the C-band. It supports transmission of advanced modulation formats and coherent, tunable reception over the same channels. In the receptor, there is the option to choose which LO to use for the coherent

detector. Either it can be used a replica of the laser generated in the transmission block or an external light source.

To test how the chip's architecture works in a system, laboratory work was done. A setup was assembled in order to emulate the designed chip. A feedback loop identical to the one on the chip was created in order to obtain and characterize the laser. The result was a laser with 6.3dBm of peak power and a 3dB linewidth of 117.7MHz. Regarding the reception block, the results were divided into two setups that differed on the LO used in the coherent detector (ECL or generated signal). The system was characterized using EVM, , constellations and eye-diagrams for a bitrate of 10Gb/s through a sweep of the power at the input of the coherent receptor. Tests for back to back and with 40km of SSMF were performed. The conclusion was that the system performed better in the case that the ECL was used as LO. This is due to the fact that this laser inputs more power in the coherent receiver and has a narrower linewidth than the generated laser. Although, when the generated laser is used the system can also work even after 40km of SSMF with the need for more power at the input of the receptor and constrains on the threshold levels.

A comparison of different transceivers available in the market was also performed within this work. It was possible to conclude that most of the available transceivers are for the already deployed networks, which do not take maximum utility of the fibre's capacity. Only one model from Finisar and one model from Fujitsu support advanced modulation formats and coherent reception. This can be explained by the lack of applications that actually are on the market, the complexity and the high cost that such a transceiver comprises. Finisar's model is for 40Gb/s DWDM applications and is on a 300-PIN package. The one from Fujitsu is for 100Gb/s applications and is on a 168 pin package. Both of them are tunable over the C-band with a channel spacing of 50GHz. The transceiver that was designed within this work also supports QPSK modulation format however is solely tunable over 4 channels separated by 100GHz and can only support 20Gb/s due to physical limitations. With the development of technology and with the need by the applications, the performance of the architecture can be improved and more variety from the vendors will appear.

As future work, sample tests of the chip should be produced in order to be tested and studied. The electronic drivers and controllers for the IQ modulator and SOA switches should be designed and implemented as well as the packaging of the chip. A study could be carried out in order to frame it on a standard packaging among the ones presented on Chapter 2.

Optical communications and PIC are fields of science that are under constant fast development. New standards are created every year and the PIC technologies are still in maturation. In order to follow the trends, the presented product should be actualized with new technologies and architectures as they appear thus, when the time to market occurs, it will be ready to be deployed. This is the only way to guarantee growing and novelty in the fast changing world of innovation.

APPENDIX A

This appendix presents the chosen full set of parameters for the VPIphotonics® embedded block for the case that the current density is 7 kA/cm^2.

Category	Parameter	Value	Unit
Device structure	Active Region Type	MQW	n.a.
	Device Section Length	1200e-6	m
	Active Region Width	2.5e-6	m
	Active Region Thickness MQW	84e-9	m
	Active Region Thickness Separate Confinement Heterostructure (SCH)	208e-9	m
	CurrentInjectionEfficiency	1	n.a
Optical parameters	Nominal Frequency	194.2e12	Hz
	Effective Index	0	n.aa
	Group Index	3.7	n.a
	Polarization Model	Isotropic	n.a.
	Internal Loss	3000	1/m
	Internal Loss Carrier Dependence	0	m^2
	Confinement Factor MQW	0.054	n.a.
	Confinement Factor SCH	0.56	n.a.
	Optical Coupling Efficiency	0.9772	n.a.
	Interface Reflection Coefficient	1e-4	n.a.
	Interface Reflection Phase Left	90	deg
	Interface Transmission Phase	0	deg
	Device Section Phase Shift	0	deg
Nonlinear Parameters	Nonlinear Index	0	m^2/W
	Two Photo Absorption	0	m/W
	Effective Mode Area	1e-12	m^2
	Confinement Factor Nonlinear	1	n.a.
Carrier Dynamics	Linear Recombination	600e-12	1/s
	Biomolecular Recombination	2.62e-16	m^3/s
	Auger Recombination	5.27e-41	m^6/s
	Carrier Capture Time constant	70e-12	s
	Carrier Escape Time constant	140e-12	s
	Initial Carrier Density	5e24	1/m^3
Gain Parameters	Gain Model	Linear	n.a.
	Gain Coefficient Linear	3.5e-20	m^2
	Carrier Density Transparency	0.4e24	1/m^3
	Gain Shape Model	Parabolic	n.a.
	Gain Peak Frequency	194.2e12	Hz
	Gain Bandwidth	23.152e12	Hz
	Carrier Density Reference Gain Shape	6e24	1/m^3
	Nonlinear Gain Coefficient	5.5e-23	m^3

	Nonlinear Gain Time constant	500e-15	s
	Chirp Model	Linewidth Factor	n.a.
	Linewidth Facto MQW	3	n.a.
	Differential Index SCH	-1.5e-26	m^3
	Carrier Density Reference Index	1e24	1/m^3
Spontaneous Emission	Noise Model	Population inversion	n.a.
	Noise Center Frequency	0	Hz
	Noise Frequency Carrier Dependence	0	Hz m^3
	Noise Bandwidth	10e12	Hz
	Noise Bandwidth Carrier Dependence	0	Hz m^3

REFERENCES

[1] IEEE Communications Society, [Online]. Available: http://www.comsoc.org/blog/ieee-comsoc-infographic-internet-growth-vs-population-penetration-geographical-region [Accessed 9 June 2014].

[2] P. J. Winzer e R. Essiambre, "Advanced Optical Modulation Formats," *Proceeding of the IEEE,* vol. 94, pp. 952-985, 2006.

[3] PT Inovação e Sistemas, "Evolution of FTTH Networks for NG-PON2," *White Paper,* 2013.

[4] E. Wong, "Next-Generation Broadband Access Networks and Technologies," *Journal of Lightwave Technology,* vol. 30, n.º 4, pp. 597-608, 2012.

[5] J. Zhao, D. Lentra, R. Santos, M. J. Wale, M. K. Smit e X. J. M. Leijtens, "Feedback Phase Influence on an Integrated Filtered-Feedback Laser," *IEEE Photonics Technology Letters,* vol. 24, n.º 23, pp. 2195-2197, 2012.

[6] M. Smit, X. Leijtens, E. Bente, J. V. d. Tol, H. Ambrosius, D. Robbins, M. Wale, N. Grote e M. Schell, "Generic foundry model fo InP-based photonics," *IET Optoelectronics,* 2011.

[7] Finisar Corporation, "FCLF-8520/8521-3 1000BASE-T Product Specification," 2005.

[8] J. P. C. C. John Anderson, "CFP MSA CFP2 Hardware Specification," 2013.

[9] Finisar Corporation, "FTLF1319F1xTL 2x5 Pin SFF Product Specification," 2011.

[10] Finisar Corporation, "FTL410QD2C Product Specification," 2013.

[11] Finisar Corporation, "FTLD10CE1C Product Specification," 2011.

[12] Finisar Corporation, "FTLX1412D3BCL Datacom XFP Product Specification," 2007.

[13] Finisar Corporation, "FTLX1341E2 Product Specification," 2008.

[14] Finisar Corporation, "FTLX1462E2 Product Specifaction," 2010.

[15] Finisar Corporation, "40 Gb/s optical transponder," 2011.

[16] Y. Luo, X. Zhou e F. E. e. a. all, "Time- and Wavelength-Division Multiplexed Passive OPtical Network (TWDM-PON) for Next-Generation PON stage 2 (NG-PON2)," *Journal of lightwave technology,* vol. 31, n.º 4, pp. 587-593, 2013.

[17] K. A. G. H. a. P. S. C. Arkady Kaplan, “LiNbO3 Integrated Optical QPSK Modulator and Coherent Receiver”.

[18] M. P. G. Y. B. P. M. Boudreau, “An Integrated InP Coheren Receiver for 40 and 100 Gb/sec telecommunication systems”.

[19] M. J. Connelly, Semiconductor Optical Amplifiers, Dordrecht: Kluwer Academic Publishers, 2002.

[20] N. K. Dutta e Q. Wang, Semiconductor Optical Amplifiers, Singapore: World Scientific Publishing Co. Pte, Ltd, 2006.

[21] M. J. Connelly, “Wideband Semiconductor Optical Amplifier Steady-State Numerical Model,” *IEEE Journal of quantum electronics,* vol. 37, pp. 439-447, 2001.

[22] Eindhoven University of Technology, Phoenix Software, COBRA, “JePPIX Course 2013 Training on Photonic Integration Technology,” 2013.

[23] Eindhoven University of Technology, COBRA, “Jeppix - Cobra Photonic IC design manual,” 2013.

[24] K. S. Meint e v. D. Cor, “PHASAR-Based WDM-Devices: Principles,Design and Applications,” *IEEE Journal of selected topics in quantum electronics,* vol. 2, pp. 236-250, 1996.

[25] R. D. Cristopher e O. Kastsunari, “Advances in Silica Planar Lightwave Circuits,” *Journal of lightwave technology,* vol. 24, pp. 4763-4789, 2006.

[26] K. Thyagarajan e Ajoy Ghatak, Fiber optic essentials, John Wiley &Sons,Inc, 2007.

[27] Research Centre for Microtechnology,FHV Research, “Arrayed Waveguide Gratings,” 2010.

[28] VPIphotonics, “Module Reference,” 2014.

[29] M. Seimetz, High-Order Modulaion for Optical Fiber Transmission, Springer, 2009.

[30] Y. Jian, “High Speed Electronic Signal Processing for Pre-Compensation in Optical Communications, PhD thesis,” Queen's Univeristy, Canada, 2011.

[31] A. P. Lopes, “Advanced Modulation Formats for Optical Access Networks,” Universidade de Aveiro, 2013.

[32] W. L. Cahill e T. T. Le, “MMI Devices for Photonic Signal Processing,” *Proc. ICTON 2007,* 2007.

[33] L. Cahill, "The modeling of MMI devices," *Proc. ICTON 2006,* vol. 2, 2006.

[34] C. M. P. Lucas B. Soldano, "Optical Multi-Mode Interference Devices Based on Self-Imaging: Principles and Applications," *Journal of Lightwave Technology,* vol. 13, n.º 4, pp. 615-627, 1995.

[35] R. Ulrich, "Ligth-propagation and imagin in planar optical waveguides," *Nouv. Rv. Optique,* vol. 27, n.º 6, pp. 337-339, 1975.

[36] Y. Ishizaka e Y. Kawaguchi, "Design of all-optical XOR and AND logic gates based on multi-mode interference devices," *International Conference on Laser & FIber-Optical Networks Modeling,* 2010.

[37] Z. Li, Z. Chen e B. Li, "Optical pulse controlled all-optical logic gates in SiGe/Si multimode interference," *Optics express,* vol. 13, n.º 3, pp. 1033-1038, 2005.

[38] S. Varghese, "Fabrication and Characterization of All-Fiber Components for Optical Access Networks, PhD thesis," International School of Photonics Cochin University of Science and Technology, 2008.

[39] M. K. Chin e S.-T. Ho, "Nanophotonic directional coupler device". United States Patente US 6,636,669 B1, 21 October 2003.

[40] R. Marz, Integrated Optics: Design and Modeling, 1994.

[41] G. P. Agrawal, Lightwave technology: Components and Devices, Hoboken, New Jersey: John Wiley & Sonc Inc., 2004.

[42] P. T. A. T. Giorgia Parca, "3D interferometric integrated structure for all-optical wavelet transform," *Electrónica e Telecomunicações,* vol. 5, n.º 4, pp. 450-452, 2012.

[43] G. P. Agrawal, Fiber-Optic Communication Systems, Wiley Interscience, 2002.

[44] VPIPhotonics, "Introduction to Optical Receivers Rx1 - Lecture Series," Univeristy Program Photonics Curriculum Version 8.0.

[45] E. Sackinger, Broadband Circtuis for Optical Fiber Communications, Holmdel: Agere Systems, 2002.

[46] L. Pancheri, "Electronics for optical communication," Lecture of Electronics for Telecommunications, Trento, 2013.

[47] Kamelian, “Semiconductor Optical Amplifiers (SOAs) as Pre-Amplifiers,” Application Note No. 0002.

[48] M. Seimetz e C.-M. Weinert, “Options, Feasibility, and Availability of 2x40 90º Hybrids for Coheren Optical Systems,” *Journal of Lightwave Technology,* vol. 24, n.º 3, pp. 1317-1322, 2006.

[49] M. Boudreau, M. Poirier, G. Yoffe e B. Pezeshki, “An Integrated InP Coheren Receiver for and Gb/Sec Telecommunications Systems,” *Optical Society of America,* 2008.

[50] R. A. Shafik, M. S. Rahman e A. R. Islam, “On the Extended Relationships Among EVM,BER and SER as Performance Metrics,” *4th International Conference on Electrical and Computer Engineering,* 2006.

[51] J. G. C. X. e. a. Ning Cheng, “World's First Demonstration of Pluggable Optical Transceiver Modules for Flexible TWDM PONs,” 2013.